Investigations of Acoustically-coupled Shear Layers Using Particle Image Velocimetry

by

Ting Yan
B.E., Southwest University of Science and Technology, 2002

A Thesis Submitted in Partial Fulfillment of the
Requirements for the Degree of

MASTER OF APPLIED SCIENCE

in the Department of Mechanical Engineering

Investigations of Acoustically-coupled Shear Layers Using Particle Image Velocimetry

by

Ting Yan
B.E., Southwest University of Science and Technology, 2002

Supervisory Committee

Dr. P. Oshkai, (Department of Mechanical Engineering)

Supervisor

Dr. N. Djilali, (Department of Mechanical Engineering)

Departmental Member

Dr. D. Sinton, (Department of Mechanical Engineering)

Departmental Member

Dr. M. Hodgson, (Department of Mechanical Engineering)

Outside Member

Supervisory Committee

Supervisor

Departmental Member

Departmental Member

Outside Member

ABSTRACT

Digital particle image velocimetry is employed to investigate acoustically-coupled flow past a coaxial deep cavity (side branch) resonator mounted in a duct. The emphasis is on the effect of the separation between the coaxial side branches on the interaction between separated shear layers that form across the side branch openings. Various resonator geometries are characterized in terms of patterns of instantaneous and time-averaged flow velocity, vorticity, and streamline topology at several phases of the acoustic cycle. In addition, phase-averaged images of the flow in conjunction with unsteady pressure measurements are evaluated in order to provide insight into the mechanisms of acoustic power generation. Generally, the acoustic source undergoes a significant transformation as the distance between the coaxial side branches changes. When the side branches are located relatively far away from each other, each of them forms an independent acoustic source. As the distance between the side branches decreases, interaction between the associated oscillating shear layers results in formation of a single acoustic source of complex spatial structure.

TABLE OF CONTENTS

LIST OF TABLES

LIST OF FIGURES

ACKNOWLEDGEMENTS

I am very thankful to my supervisor Dr. Peter Oshkai for his invaluable support and guidance during my research. I also would like to thank him for spending uncountable time in preparation of this thesis.

I would like to thank my family and Xiaogang Zhang, who bring me where I am today. Without their encouragement, this work could have never been done.

I want to thank Dr. Ned Djilali of the University of Victoria for providing instrumentation for this study. I am also grateful of financial support of Natural Sciences and Engineering Research Council of Canada (NSERC) under a Discovery Grant.

CHAPTER 1

INTRODUCTION

1.1 Motivation

Over the years, flow-induced acoustic resonance has been a focus of considerable attention of the research community. This phenomenon occurs in many engineering applications, including fluid flow in pipelines, turbomachines, heat exchangers, as well as in flows past cavities in fast moving vehicles. Flow-acoustic resonance is characterized by coupling between a resonant acoustic mode that exists in the flow system and an instability of the separated shear layer. When resonance occurs, high-amplitude acoustic pressure pulsations can cause severe noise and vibrations to occur. These vibrations can compromise the operation and the structural integrity of the system. Therefore, the phenomenon of flow-induced vibration must be characterized in order to optimize design for noise control.

1.2 Cavity Flow

1.2.1 Classifications of cavity flow

Flow-excited oscillations in cavities have been the subject of extensive research. There are two basic flow regimes that a cavity can yield depending upon the length-to-depth ratio, L/W [1] (see Figure 1.1). For L/W < 10 the cavity is termed "open" that is characterized by the reattachment of separated shear layer to the trailing edge and the drag of the cavity is small. For L/W >10 the cavity is termed "closed" as the free shear layer reattaches to the lower wall resulting in significantly increased drag. Experimental results found that when the resonance occurs, either longitudinal or transverse wave can dominate

the open cavities, which depends on L/W ratio and the Mach number (M). In the short cavity, the oscillation is sustained by a transverse wave, while in the long cavity, longitudinal mechanism control the acoustic mode.

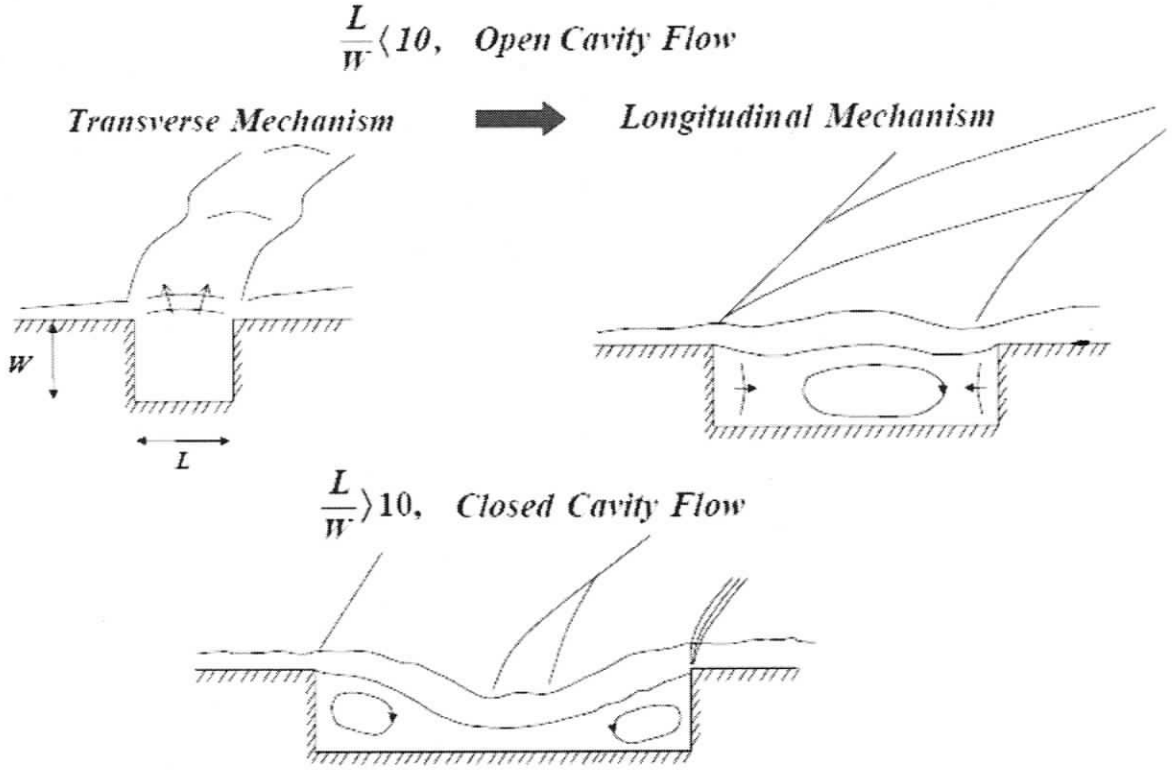

Figure 1.1: Cavity flow models for different length to depth ratios L/W [1].

1.2.2 Characteristics of non-resonant oscillations in cavity flow

Rockwell & Naudascher [2] classified the flow excitation mechanisms into the fluid-resonant and the fluid-dynamic categories. The fluid-dynamic (acoustic-free) mechanism corresponds to generation of self-sustained flow oscillations in the absence of resonance effects. In contrast, in the fluid-resonant regime, the oscillations are sustained by the coupling between the resonant sound field and the separated unstable flow. The hydrodynamic oscillations in an acoustic-free system are illustrated in Figure 1.2.

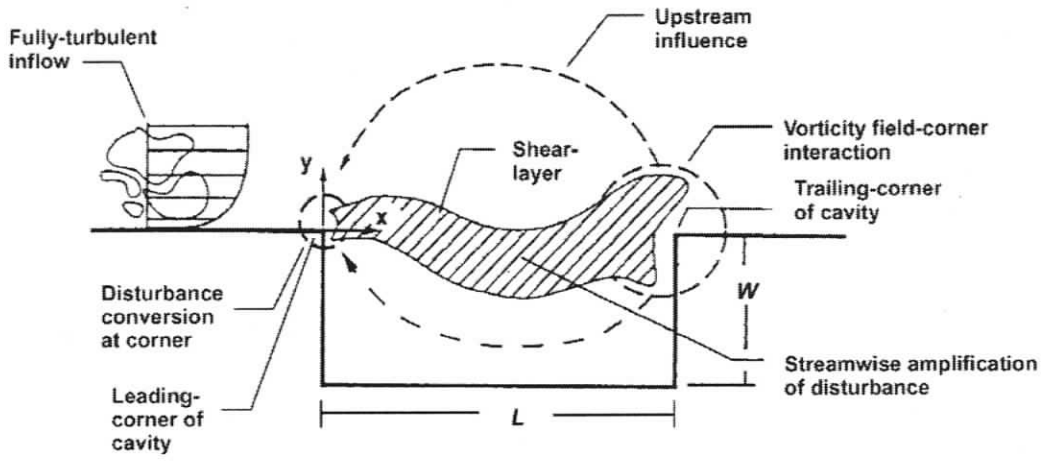

Figure 1.2: Principal elements of self-sustaining oscillation of turbulent flow past cavity associated with purely hydrodynamic effects [3].

The turbulent inflow separates at the upstream edge of the cavity and forms a shear layer over the cavity opening. The shear layer instability results in formation of large-scale vortices that are convected downstream towards the trailing edge of the cavity and impinge on the trailing corner. The impingement of the shear layer at this corner results in alternate inward and outward motions, which create alternate pressure condensations and rarefactions in the cavity. The pulsations feed back to the upstream edge and amplify the shear layer oscillation. The transverse velocity associated with the motion of the shear layer is in the approximation of linear disturbances. The wave is assumed to grow exponentially in space. The growing motion in the shear layer can be expressed as Eqn. (1) [4]

$$u(x,y,t) = |u(y)|e^{\alpha_i x}e^{i(\alpha_r x-\omega t)}, \qquad 0 \le x \le L \tag{1}$$

where $u(x,y,t)$ is fluctuating velocity, ω is the circular frequency, α_r is the real part of the complex wave number $\alpha=\alpha_r+i\alpha_i$, $\alpha_i x$ expresses the spatially growing motion along the opening. The disturbance at the downstream edge is in the form of

$$u(L,y,t) = |u(y)|e^{\alpha_i L}e^{i(\alpha_r L-\omega t)} \tag{2}$$

The most optimum coupling will happen when the maximum inflow occurs at the downstream edge. At this condition, the phase $\alpha_r L$ of *u(L)* with respect to *u(0)* should be $\pi/2$ less than complete cycle.

$$\alpha_r L = 2n_s\pi - \pi/2, \qquad n_s = 1,2,3... \tag{3}$$

Since $\alpha_r = \omega/U_c$, U_c is the wave speed, then the preferred frequencies, $f_s = \omega/2\pi$, are given by

$$f_s L/U_c = (n_s - \frac{1}{4}), \qquad n_s = 1,2,3,... \tag{4}$$

This equation provides the possible condition for the frequency of a standing wave of fluid disturbance across the opening.

1.2.3 Characteristics of resonant oscillations in cavity flow

When the frequency of the shear layer is compatible with the resonant acoustic mode of the cavity, the locked-on flow tones are generated. The frequencies of the resonant mode for an open-closed cavity (pipe) can be estimated from [5] as follows:

$$f_n = \frac{(2n-1)C}{4W}, \qquad n = 1,2,3..... \tag{5}$$

where f_n is the natural frequency, C is the speed of sound and n is the acoustic mode order. W is the depth of the cavity (pipe). According to Eqn. (4), the waves associated with the shear layer have preferential wavelengths associated with certain frequencies which can be determined by

$$f_s = 0.52n_s\left(\frac{U}{L}\right) \qquad \text{(laminar boundary layer)} \quad n_s = 1,2,3..... \tag{6}$$

$$f_s = 0.33(n_s - \frac{1}{4})\left(\frac{U}{L}\right) \qquad \text{(turbulent boundary layer)} \quad n_s = 1,2,3..... \tag{7}$$

where f_s is the vortex shedding frequency, L is the width of the cavity, U is the mean flow velocity and n_s is the vortex shedding mode order which indicates the number of vortices formed in the shear layer. For the deep cavity or pipe, transverse wave will dominate the cavity. The resonance modes consist of odd multiples of a quarter wavelengths along the cavity (pipe) [Figure 1.3]

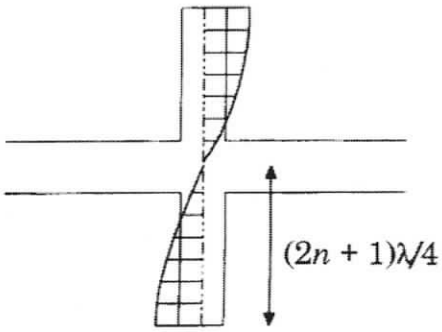

Figure 1.3: The lowest excited acoustic modes for co-axial side branch geometry [5].

The more complex flow mechanism due to the interaction between the acoustic field and the shear layer which spans the mouth of the cavity has been a subject of several investigations [3, 5-11]. At the point of separation, the incident acoustic waves force the shear layer and amplify the velocity fluctuations in the shear layer. The small scale vortices extract energy from the mean flow to form large scale vortex structures. Further downstream, the energy is transferred into the resonant acoustic field through the interaction of the formed vortices with the acoustic field and the downstream corner of the cavity. This phenomenon was described in detail by Ziada [10]. The acoustic energy is produced when the acoustic flux is directed out from the cavity. When the acoustic flux is directed into the cavity, the acoustic energy is absorbed by the vortex.

Bruggeman [10] classified the flow-excited acoustic oscillations of closed side-branches into three categories in terms of pulsation levels which is expressed by the ratio of

U_{ac}/U. U_{ac} is amplitude of acoustic velocity and U is the mean velocity in the main pipe. These are low, moderate as well as high levels of acoustic oscillations. At low amplitude acoustic pulsation ($U_{ac}/U<10^{-3}$), the growth of velocity instability was based on the linear theory. The amplitude of shear layer oscillation increases exponentially with the distance from leading edge. For moderate amplitude ($U_{ac}/U<10^{-1}$), the development of vortices is nonlinear. The vorticity concentrated in the line vorticies. The strength and the path of vortices are independent of the amplitude of the acoustic field. In the case of large amplitude, the formation and propagation of vortices become strongly dependent on the acoustic amplitude. The shear layer developed into discrete vortices.

Jungowski *et al.* [12] reported that the ratio between the cavity width and the main pipe width has a pronounced effect on the acoustic pressure amplitude. When the ratio is increased, the pulsation amplitude decreases. Ziada *et al.* [5] studied the effect of Reynolds number on the acoustic resonance amplitude and the range of frequency lock-on occurrence. The authors found that higher order shear layer modes are consecutively excited as the Reynolds number is increased. When the minimum Reynolds number which is required to excite the resonance is exceeded, the resonance amplitude at the higher modes decreases as the mode order is increased. The higher order acoustic modes are susceptible to lock-on over a wider range of Reynolds numbers.

Several experimental investigations focused on the development of the separated shear layers during a typical acoustic cycle. Experiments of Ziada [10] provide detailed smoke visualizations of formation and propagation of vorticies during a single period of acoustic oscillation. Kriesels *et al.* [6] employed laser-Doppler velocimetry to obtain measurements of flow in cross junction of co-axial side branch system. Oshkai *et al* [7]

studied the development of separated shear layers over shallow cavities using digital particle image velocimetry (DPIV).

1.3 Objectives

Based on the review of the previous studies presented in the previous section, the following unresolved issues were identified:

a) Global, quantitative visualization of acoustically-coupled flow over the mouths of co-axial side branches using particle image velocimetry has not been pursued.

b) The instantaneous and averaged flow patterns for flow past co-axial side branches during the acoustic resonance have not been examined. Patterns of vortical structures generated during the acoustic cycle and their contribution to the acoustic power generation need to be investigated.

c) As the main duct width is varied, the amplitude of acoustic pressure and structure of acoustic source are expected to change. This effect has not been adequately addressed.

The objective of the work presented in this thesis is to address these issues. The focus is on the effect of the ratio between the side branch width and the main duct width on various characteristics of the coaxial side branch resonator system, including the resonant pressure amplitude, the shear layer oscillation mode, and the spatial structure of acoustic noise source. Flow visualization in the side branch junction region is performed using a technique of digital particle image velocimetry (DPIV.) Imaging of the flow structure in conjunction with unsteady pressure measurements leads to patterns of velocity, vorticity, and streamline topology at various phases of the acoustic cycle. Howe's theory of

aerodynamic sound [13] is used to calculate the acoustic energy generated or absorbed by vortices during various phases of the acoustic cycle.

CHAPTER 2

EXPERIMENTAL SYSTEM AND TECHNIQUES

2.1 Experimental Apparatus

2.1.1 Coaxial side branch resonator system

The objective of this experimental apparatus is to investigate phenomenon of flow-induced resonance in a co-axial side branch system and the influence of the width of the main duct. A schematic view of the coaxial side branch resonator system is shown in Figure 2.1. The flow facility, which consists of an inlet plenum chamber, a main duct, and a coaxial side branch arrangement, allows variations of the channel geometry, optical access to the separated flow area(s), as well as ability to perform acoustic pressure measurements. The whole system with the exception of the side branches was constructed from Plexiglas especially in separated flow region to allow optical access. The dimensions of the components are given in Table 2.1. The velocity of air supplied by a compressor is controlled through a system of pressure regulators.

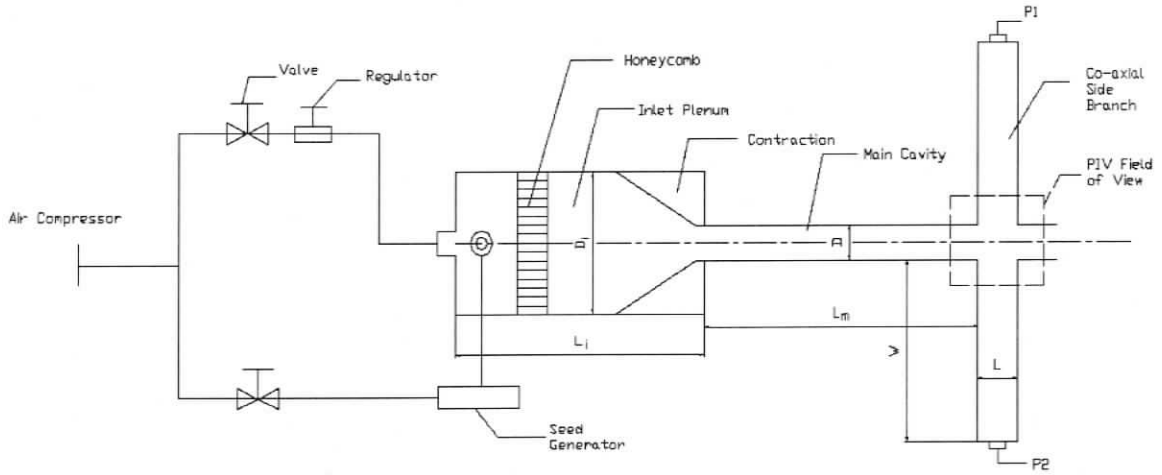

Figure 2.1: Schematic of experiment system.

	Width(D_i, mm)	Height(H_i, mm)	Length(L_i, mm)
Inlet Plenum	128	27	304.8

	Width(D, mm)	Height(H, mm)	Length(L_m, mm)
Narrow Main Duct	6.35	25.4	492.1
Wide Main Duct	12.7	25.4	492.1

	Width(L, mm)	Height(H_s, mm)	Length(W, mm)
Side Branch	25.4	25.4	482.6

Table 2.1: Experiment system dimensions

2.1.1.1 Inlet plenum chamber

The inlet plenum chamber was designed to serve as a flow conditioner. The plastic honeycomb was installed inside the plenum to reduce the level of turbulence and straighten the air flow. A seed generator was connected upstream of the honeycomb to enable introduction of particles into the airstream for flow visualization purposes. In the downstream section of the plenum, a 2:1 contraction connects the plenum to the main duct. The flow is accelerated by the contraction to improve the flow uniformity and reduce the turbulence level. This contraction is modular in order to allow alternation of main duct size.

2.1.1.2 Main cavity

The goal of this experiment is to examine the influence of the width of the main duct on the separated flow structure and generated acoustic power. Therefore, the main duct was designed to allow variation of its width. The entire system was designed as an assembly of modular components. The widths of the main duct selected for the experiments were 6.35 and 12.7mm. In both cases, the main duct was 492.1mm long.

2.1.1.3 Co-axial side branches

In order to enhance resonance, the co-axial side branches were constructed from 1.25 x 1.25 in box aluminum. They were located 454 mm downstream of the inlet plenum,

on opposite sides of the main duct and inline with each other. In the case of an open-closed pipe, if it is to resonate with an external sound source, the fixed length W of the pipe must be equal to an odd number ($2n$-1) of quarter wavelengths of the incoming sound wave.

$$W = (2n-1)\lambda_n / 4 \qquad n = 1,2,3,..... \tag{8}$$

where λ_n is the wavelength. Since $\lambda_n = C/f_n$, where C is speed of sound, Eqn. (8) yields

$$W = (2n-1)C / 4f_n \qquad n = 1,2,3,..... \tag{9}$$

Therefore, the resonant frequencies are described by the following expression:

$$f_n = \frac{(2n-1)C}{4W}, \qquad n = 1,2,3..... \tag{5}$$

The pipe length was selected based on the criteria provided by Ziada [3]. Eqn. (5) was used to calculate the resonant frequencies of the side branch. The results are shown in Table 2.2.

mode	Natural frequency (Hz)
1	177.9
2	533.7
3	889.6
4	1245.4
5	1601.2
6	1957.1

Table 2.2: First six resonant frequencies of side branch

A flow across the mouth of the open-closed pipe is turbulent in the present study. Vorticies are shed from the upstream corner of the cavity at the Strouhal frequency as described in Eqn. (7). Figure 2.2 shows the first seven Strouhal modes (c_1-c_7) as functions of inflow velocity. The first six acoustic modes of the side branch are also shown in this

figure. The resonant sites correspond to the intersections of the Strouhal (hydrodynamic) and the side branch (acoustic) modes.

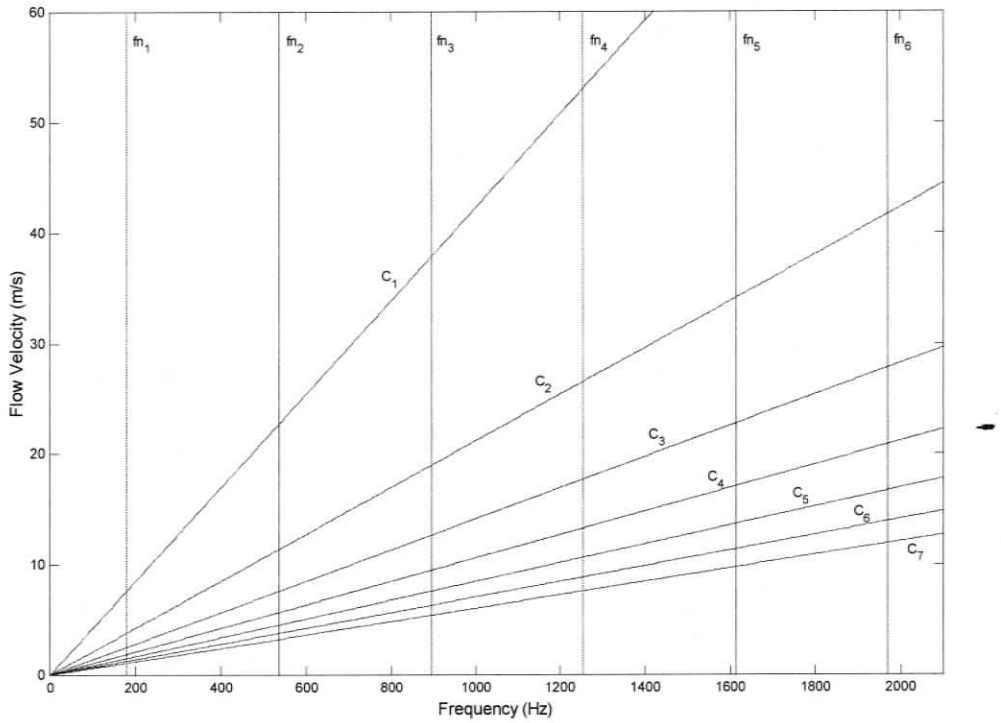

Figure 2.2: Resonant frequencies and Strouhal frequencies for side branch used in the present experiment [14].

The resonant flow velocity at the intersections can be calculated by combining Eqn. (5) and (7)

$$U = \left(\frac{d}{0.33(n_s - \frac{1}{4})} \right) \left(\frac{n_n C}{4L} \right) \qquad n_s = 1,2,3....,n_n = 1,2,3.... \tag{10}$$

The calculated resonant velocity values (m/s) are shown in Table 2.3.

		Natural Frequency Mode					
	n_s \ n_s	**1**	**2**	**3**	**4**	**5**	**6**
Strouhal Mode	**1**	7.53	22.60	37.66	52.72	67.79	82.85
	2	3.77	11.30	18.83	26.36	33.89	41.42
	3	2.51	7.53	12.55	17.57	22.60	27.62
	4	1.88	5.65	9.41	13.18	16.95	20.71
	5	1.51	4.52	7.53	10.54	13.56	16.57
	6	1.26	3.77	6.28	8.79	11.30	13.81
	7	1.08	3.23	5.38	7.53	9.68	11.84

Table 2.3: Calculated resonant flow velocities

2.1.2 Acoustic pressure measurements

PCB piezotronics model 103A02 transducers were employed for pressure measurement. These transducers were mounted at the dead ends of the side branch resonator and have a nominal sensitivity of 1500 mv/psi. The outputs from the transducer were connected to a National Instruments PXI-4472 board. This board has eight analog input channels, which are simultaneously sampled at a maximum rate of 102.4 kHz with 24-bit resolution. During the present experiments, the analog pressure signals were converted to digital form at the time of acquisition using a sampling rate of 8192 Hz. The selection of sampling rate was based on two considerations. For interpretation of the pressure signal in the frequency domain, the sampling rate must be twice as high as the maximum frequency of interest (Nyquist criterion). For representation in the time domain, a minimum of ten samples per cycle is desirable. This leads to the sampling rate should be at least ten times higher than the maximum frequency of interest. The maximum frequency of interest in the present investigation is approximately 840 Hz which corresponds to approximately 10 samples per cycle using the sampling rate of 8192 Hz.

Custom Labview and Matlab routines were used to process the data from pressure transducers and to characterize the acoustic pressure in time and frequency domain (See Appendices E and F for details.) Spectral analysis of the pressure signals was accomplished using Fast Fourier Transform (FFT). In addition, the time trace of the pressure signal was employed as a phase reference for the image acquisition. The acoustic pressure signal was not filtered for the selection of fundamental frequency since the NI 4472 board contains a built-in two-pole anti-alias lowpass filter for each channel that can remove mostly noise from signals [15]. Moreover, due to the low damping of the coaxial side branch resonator, resonant frequency components of the signal exhibited high amplitudes compared to non-resonant frequencies. In addition, dimensions of the experimental apparatus were strategically chosen to separate the resonant acoustic modes from higher-order harmonics in the frequency domain. Figure 2.3 shows a flow chart of the data acquisition system.

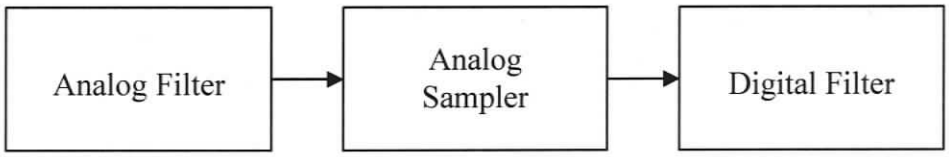

Figure 2.3: Flow chart of the data acquisition system.

The analog filter with a cutoff frequency of 400 kHz was deployed ahead of the analog sampler. The analog sampler operates at 64 times the selected sample rate for rates above 51.2 kHz and at 128 times the selected samples rate for rates below 51.2 kHz, which can sample the high frequency noise component accurately and avoid error. The sampled data produced by the analog sampler is passed on to a digital anti-alias filter. This digital filter passes only those signal components with frequencies below the Nyquist frequency (half of the sampling rate). In the present set of experiments, the ambiguity of sinusoidal

pressure signal was minimal and the dominant frequency was well-isolated from other frequencies (see Figure 2.4).

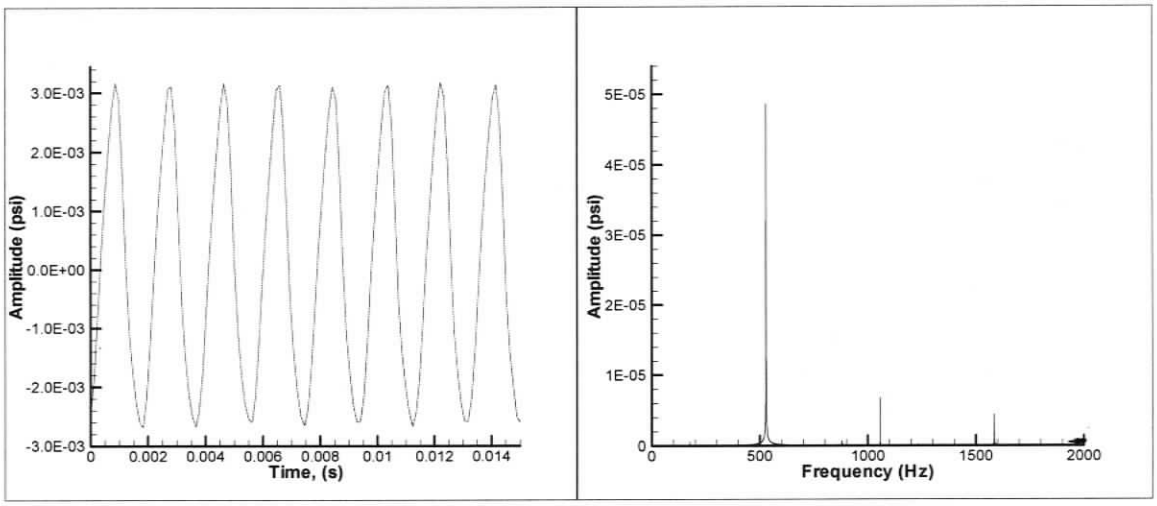

Figure 2.4: Acoustic pressure signals in time domain (left) and frequency domain (right).

2.2 Technique of Particle Image Velocimetry

Particle Image Velocimetry (PIV) is a flow visualization technique that can provide an accurate quantitative measurement of the instantaneous flow velocity over a region illuminated by a two-dimensional sheet of light. In PIV, the fluid flow is seeded with small particles and illuminated by a thin sheet of laser light. The images of the illuminated particles are captured using a digital camera. The images are processed on a computer to calculate the velocity field of the flow. Adrian [16] provided a comprehensive review of the PIV techniques. Figure 2.5 shows the basic equipment for PIV experiments.

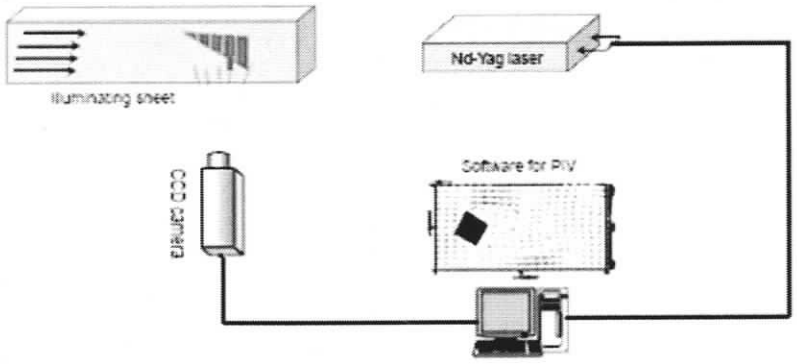

Figure 2.5: Experimental equipment for PIV [17].

The PIV technique has several advantages over other flow measurement methods including the following:

1. Properly-implemented PIV is essentially non-intrusive. Careful selection of particle sizes and seeding density ensures negligible interference with the fluid flow;

2. PIV provides flow velocity information at many points in the flow field simultaneously;

3. PIV can produce real-time velocity maps through use of state-of-the-art digital cameras and dedicated computer hardware;

4. Resulting global quantitative images have relatively high spatial resolution.

The PIV techniques have several limitations. First, PIV techniques are limited by minimum achievable time between image pairs, which results in the limitation on the maximum resolvable flow velocity. In addition, temporal resolution of a PIV image sequence is limited by the laser repetition rate and the acquisition rate of the camera.

Two major error types associated with PIV are mean bias and root-mean-square (RMS) errors. The fundamental source of these errors arises from the implementation of cross correlation algorithm. The errors arise from the peak-finding scheme, which locates the correlation peak with sub-pixel accuracy, and from noise in the correlation domain [18].

2.2.1 Image acquisition

Quantitative visualization of acoustically coupled flow was accomplished by a digital version of the particle image velocimetry (DPIV). The air flow was seeded with olive oil droplets with a typical diameter of approximately 1 μm, which served as tracer particles. Images of the particles, which were illuminated by a dual-head Nd: YAG laser, were captured by a high-resolution digital camera. The charge-coupled device (CCD) camera was positioned perpendicular to the plane of the light as shown in Figure 2.6.

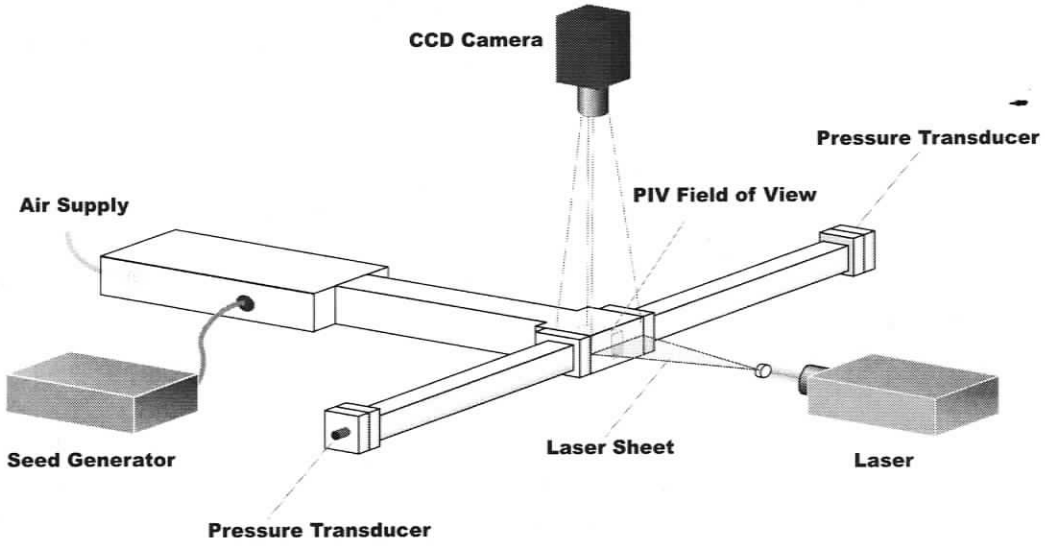

Figure 2.6: Schematic of the PIV setup.

The CCD camera has a total of 1376 (horizontal) × 1040(vertical) pixels, which correspond to physical dimensions of CCD of 38.3 (horizontal) × 28.8 (vertical) mm. The maximum framing rate of the camera is 15 frames/s, which provides 7.5 cross-correlated images per second. The rate of velocity vector acquisition was further reduced to 4.9 Hz due to data transfer rate limitations when capturing directly to computer's random access memory (RAM.) A lens with a focal length of 60 mm and a 532 nm wavelength filter with a bandwidth of 10 nm were used for image acquisition. The magnification of the camera is 1:2.8. The displacement of the particles was recorded as a pair of single-exposed images.

Depending on the flow velocity and the magnification factor of the camera lens, an appropriate time delay between the two pulses was chosen such that adequate displacements of the particle images on the CCD are obtained. The recorded local particle displacements were measured across the entire area of interest, scaled by the image magnification, and then divided by the known laser pulse separation time to obtain flow velocity vectors at each location. The Figure 2.7 shows a raw image used for calculation of the vector field.

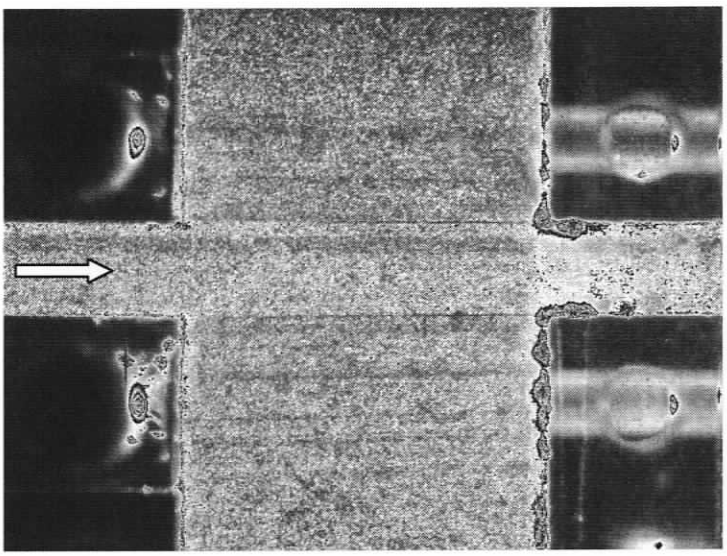

Figure 2.7: Raw image used for calculation of vector field.

2.2.2 Image processing

2.2.2.1 Correlation algorithm for velocity calculation

For the present study, two frame cross-correlation version of DPIV was used to obtain velocity measurements. Two sequential images were divided into small interrogation windows. Using statistical cross-correlation technique, one local displacement vector was determined for each interrogation window. The discrete cross-correlation function $\phi_{fg}(m,n)$ for two sample regions $f(k,l)$ and $g(k,l)$ is given in Eqn. (11) [19]

$$\phi_{fg}(m,n) = \frac{\sum_{k=-\infty}^{\infty}\sum_{l=-\infty}^{\infty} f(k,l)g(k+m,l+n)}{\sum_{k=-\infty}^{\infty}\sum_{l=-\infty}^{\infty} f(k,l)\sum_{k=-\infty}^{\infty}\sum_{l=-\infty}^{\infty} g(k,l)}, \tag{11}$$

where $f(k,l)$ and $g(k,l)$ denote image intensity distribution of the first and second image in the pair, k and l are coordinates of the interrogation window, m and n are pixel offsets between the two images. A high cross-correlation value (close to unity) corresponds to a case where many particle images match up with their corresponding shifted partners. The highest peak in the cross-correlation image represents the most probable displacement for the particles within the interrogation window. Fast Fourier transforms (FFT) was employed in order to speed up the calculation of the cross-correlation function. Rather than performing a summation over all the elements of the sampled region as in Eqn. (11), the operation is changed to a complex conjugate multiplication of each corresponding pair of Fourier coefficients. According to the Nyquist criterion associated with the Fourier transform, the maximum displacement that can be computed accurately is one half of the interrogation window size. Multi-pass processing with incremental decrease of the interrogation window size from 128 × 128 pixels to 32 × 32 pixels with 50% overlap was used to improve spatial resolution of the resulting vector field. This process resulted in the final spatial resolution of 0.45 x 0.45 mm. When a local particle displacement vector is found, the local velocity vector can be calculated as the ratio of the displacement vector to the time interval between the two exposures (ds/dt). Due to light reflections near the edges of the cavity, velocity vectors could not be calculated in these regions.

2.2.2.2 Post processing

Once a vector field was calculated, post-processing of the raw velocity field was undertaken to eliminate spurious vectors. False vectors were automatically removed from the entire sequence of velocity fields by applying a median filter. Regions where spurious vectors were removed were subsequently filled using bilinear interpolation. In addition, the images were smoothed using a Gaussian filter with a standard deviation of kernel of 1.3. Figure 2.8 shows a post-processed velocity vector field.

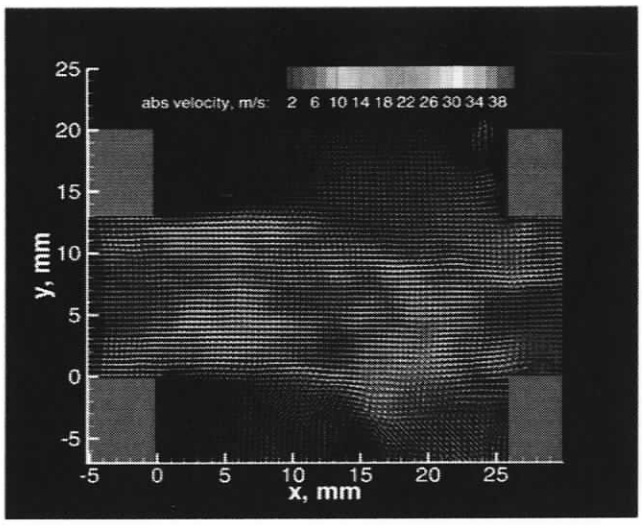

Figure 2.8: Post-processed velocity vector field.

2.2.2.3 Vorticity calculation

Vorticity is an important parameter that is used to illustrate the nature of the instability within the flow. The values of out-of-plane vorticity ω_z were calculated based on the PIV velocity vector fields using Eqn. (12).

$$\omega_z = \frac{\partial v}{\partial x} - \frac{\partial u}{\partial y}, \tag{12}$$

where v is the y-component of velocity, u is the x-component of velocity. Figure 2.9 shows a schematic of the numerical grid for vorticity calculation. Interrogation window

size of 32 × 32 pixels with 50% overlap that was used for velocity calculation resulted in a uniform grid with the step size $d = 16$ pixels.

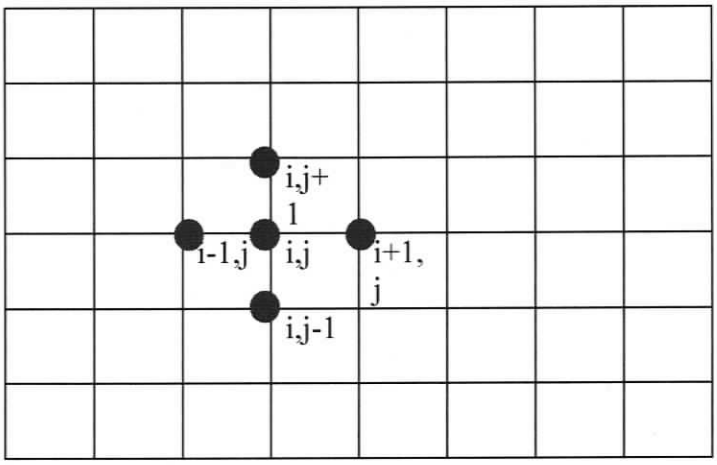

Figure 2.9: Domain for vorticity calculation.

For the interior points of the domain, the derivatives in Eqn. (12) were approximated by central differences:

$$\omega_z(i,j) = \frac{v(i+1,j) - v(i-1,j)}{2*d} - \frac{u(i,j+1) - u(i,j-1)}{2*d}. \qquad (13)$$

For the points at the boundaries, forward or backward formulae were implemented:

$$\text{Left boundary: } \omega_z(i,j) = \frac{v(i+1,j) - v(i,j)}{d} - \frac{u(i,j+1) - u(i,j-1)}{2*d}; \qquad (14)$$

$$\text{Right boundary: } \omega_z(i,j) = \frac{v(i,j) - v(i-1,j)}{d} - \frac{u(i,j+1) - u(i,j-1)}{2*d}; \qquad (15)$$

$$\text{Top boundary: } \omega_z(i,j) = \frac{v(i+1,j) - v(i-1,j)}{2*d} - \frac{u(i,j) - u(i,j-1)}{d}; \qquad (16)$$

$$\text{Bottom boundary: } \omega_z(i,j) = \frac{v(i+1,j) - v(i-1,j)}{2*d} - \frac{u(i,j+1) - u(i,j)}{d}. \qquad (17)$$

2.3 Time-averaging of PIV Images

Pairs of images that were used to yield a single velocity vector field were acquired at a time interval of 1/4.9s. Since the image acquisition frequency was significantly lower than the frequency of the acoustic resonance under investigation, the sequence of the PIV images was essentially random with respect to the oscillating acoustically-coupled flow. This feature made the PIV sequences appropriate for calculation of time-averaged turbulent statistics. In order to minimize the amount of collected data, the minimum sample size, appropriate for the calculation of time-averaged flow parameters was determined. The number of images used in a sample calculation was incrementally increased, and the results were compared for different sample sizes. For the present flow configuration and range of flow velocities, a sample size of 200 images was found to be adequate. The definition for each of the time-averaged parameters used in the present investigation is provided below (N is the total number of images).

Time-averaged horizontal component of velocity:

$$< u >= \frac{1}{N}\sum_{n=1}^{N} u_n(x,y) \tag{18}$$

Time-averaged transverse component of velocity:

$$< v >= \frac{1}{N}\sum_{n=1}^{N} v_n(x,y) \tag{19}$$

Time-averaged vorticity:

$$< \omega >= \frac{1}{N}\sum_{n=1}^{N} \omega_n(x,y) \tag{20}$$

Root-mean-square of u component fluctuation:

$$u_{rms} = \left\{ \frac{1}{N}\sum_{n=1}^{N} \left[u_n(x,y) - < u(x,y) > \right]^2 \right\}^{1/2} \tag{21}$$

Root-mean-square of v component fluctuation:

$$v_{rms} = \left\{ \frac{1}{N}\sum_{n=1}^{N} \left[v_n(x,y) - < v(x,y) > \right]^2 \right\}^{1/2} \tag{22}$$

Averaged value of Reynolds stress correlation:

$$< u'v' >= \frac{1}{N}\sum_{n=1}^{N} \left[u_n(x,y) - < u(x,y) > \right]\left[v_n(x,y) - < v(x,y) > \right] \tag{23}$$

2.4 Phase-averaging of PIV Images

The trigger signal to the camera and the laser was provided by a synchronizer unit (LaVision Inc.) The trigger signal to the laser was recorded together with the acoustic pressure signal to provide a reference to the time instant, at which PIV images were acquired. Using this information, it is possible to determine the phase of acquisition of each velocity field with respect to a typical acoustic cycle.

M. Geveci [8] outlined an approach for obtaining the phase-averaged PIV images. The time trace of the pressure signal is used as a phase reference of image acquisition. Phase ϕ is defined as the phase difference between the occurrence of zero crossing of pressure signal from negative to positive and acquisition of the pair of images. A typical acoustic cycle is divided into a specified number of phase intervals. The images that correspond to the same phase interval are classified as having the same phase. The position of large-scale vortical structures along the cavity opening (obtained from PIV images) is used to improve the accuracy of phase determination. In contrast to this approach, the phase-locking technique that was employed in the present study enabled acquisition of 100 cross-correlated pairs of images at each pre-determined phase of the acoustic oscillation cycle using the real-time acoustic pressure signal as a reference. The acoustic pressure signal was acquired using a National Instruments board (PXI-4472). Custom Labview code was developed to control the PXI-4472 board to sample the real-time pressure signal and to determine the point of the occurrence of zero amplitude with a rising edge in the signal. At this instant, a single pulse TTL signal is sent from output board (NI PXI-6221) to trigger the camera for image capture. Since the maximum framing rate of the camera is 4.9 Hz (in terms of cross-correlated image pairs), and the interested frequencies of the pressure are

545 and 840 Hz, the TTL pulse should only be sent once in approximately 10 and 16 acoustic cycles respectively. Figure 2.10 shows the recorded acoustic signal (red line) and the laser trigger signal (green line). This method resulted in the error of the phase calculation of ±4°.

The time delay between receiving the trigger and firing the laser can be set arbitrarily by the Davis software (LaVision Inc.), which is used to operate the DPIV system. The minimum delay is 0.4ms. One hundred pairs of images at each pre-determined phase of the acoustic oscillation cycle were acquired. Ensemble-averaging of the PIV images corresponding to the same phase was performed to produce a single global quantitative representation of the flow at that phase. Flow features at ten phases of the acoustic cycle were investigated in the present study. It is apparent that the two consequential laser trigger signals occurred at the same phase of acoustic cycle. The accuracy of the phase is within ±4°.

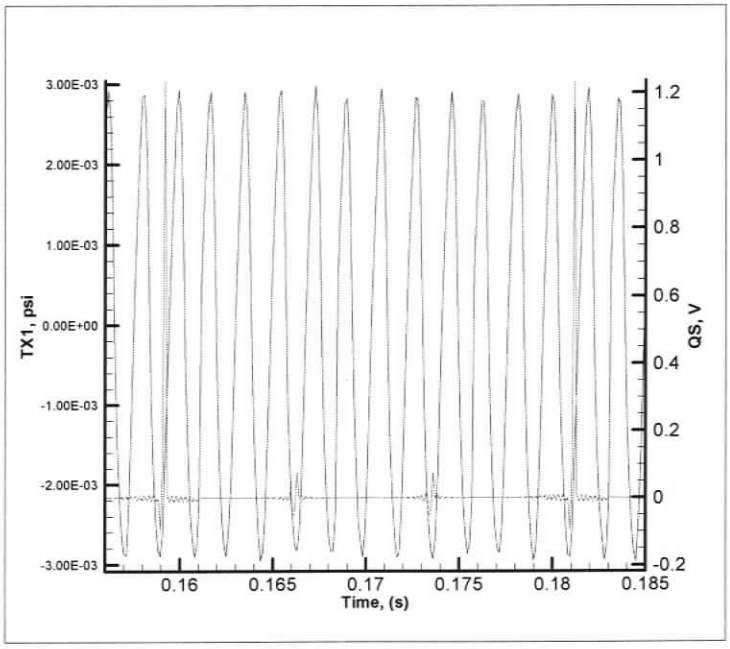

Figure 2.10: Phase information provided by reference acoustic pressure signal (red) and laser trigger signal (green) that corresponds to the time instant of image acquisition.

2.5 Data Collection

Ziada[20] studied the non-resonant and resonant oscillations in a jet-slot oscillator with deep cavity resonator. It was observed that the shear layer oscillation was symmetrical when the resonance was not established. Within the resonance range, a given acoustic mode can be excited over a range of Strouhal numbers (Ziada [21]). Resonance that occurred at the lowest value of Strouhal number was found to be excited by the first mode of shear layer oscillations. Higher modes of shear layer oscillation excite the resonance at the higher values of the Strouhal number. In the present study, the experiments were performed to characterize the following regimes of the acoustically-coupled flow: 1) shear layer oscillation without acoustic resonance effects, which is referred as non-resonant flow oscillation; 2) flow-induced acoustic resonance excited by the first hydrodynamic oscillation mode at low Strouhal number; 3) flow-induced acoustic resonance excited by the second hydrodynamic oscillation mode at a relatively high Strouhal number. Figure 2.11 shows the oscillation patterns of these three cases. At each case, the data were collected for both narrow (D = 6.35mm) and wide main duct (D = 12.7mm). Case 2 corresponds to the dominant acoustic frequency f = 545 Hz, Case 3 corresponds to the acoustic frequency f = 840 Hz.

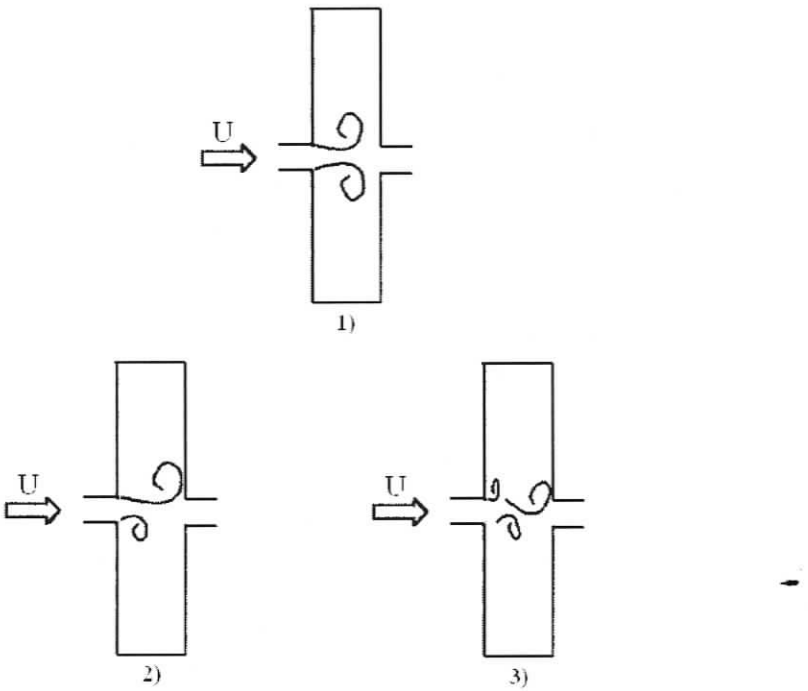

Figure 2.11: Schematic presentation of the shear layer oscillation patterns of the three investigated cases [20].

For each data set, global instantaneous images, time-averaged images, as well as phase-averaged images were evaluated to provide insight into the flow physics during tone generation.

CHAPTER 3

EFFECT OF THE MAIN DUCT WIDTH

3.1 Acoustic Response of the Resonator

In the present investigations, each branch of the coaxial side branch resonator is assumed to act as a perfect quarter wave resonator. Therefore, only acoustic waves that are odd multiples of a quarter wavelengths can be excited inside the side branches. The pressure perturbations in the co-axial side branches at several resonant acoustic modes are illustrated schematically in Figure 3.1. The frequency of an acoustic mode can be estimated according to Eqn. (5).

$$f_n = \frac{(2n-1)C}{4W}, \qquad n = 1,2,3..... , \tag{5}$$

where m = 2n-1 (n = 0, 1, 2...) indicates the mode number. Figure 3.1 shows three examples of possible resonance modes, corresponding to m = 1, 3, and 5. For m = 1, one quarter of the characteristic wavelength of the resonator spans the length of each side branch, and thus one half of a wavelength is completed across both side branches. Thus, for m = 3 and m = 5, three-quarters of one wavelength and five-quarters of one wavelength span each side branch respectively.

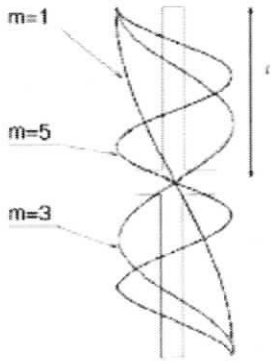

Figure 3.1: Acoustic pressure distribution at resonant acoustic modes in the co-axial branches.

Figure 3.2 shows evolution of the pressure spectra as the main flow velocity in the main duct is increased. The data correspond to the case of the wide main duct. The measurements were obtained at the end of one of the side branches. The three dominant spectral peaks correspond to the occurrence of resonances at three different acoustic modes. These acoustic oscillations are classified as locked-on flow regimes. They correspond to matching of the frequencies of hydrodynamic shear layer oscillations to the frequencies of acoustic standing waves in the side branches. The results given in the Figure 3.2 show that the first acoustic mode (f = 172 Hz) is excited first as the velocity increases. The second mode to be excited is the fifth acoustic mode (f = 840 Hz). The highest peak corresponds to the third acoustic mode (f = 545 Hz). The measured frequencies are within ±6% of the predicted resonance frequencies, which confirm that the model described by Eqn. (5) provides a good prediction of resonant acoustic modes. Figure 3.2 indicates that the amplitude of acoustic oscillation is increased as the mean flow velocity increases.

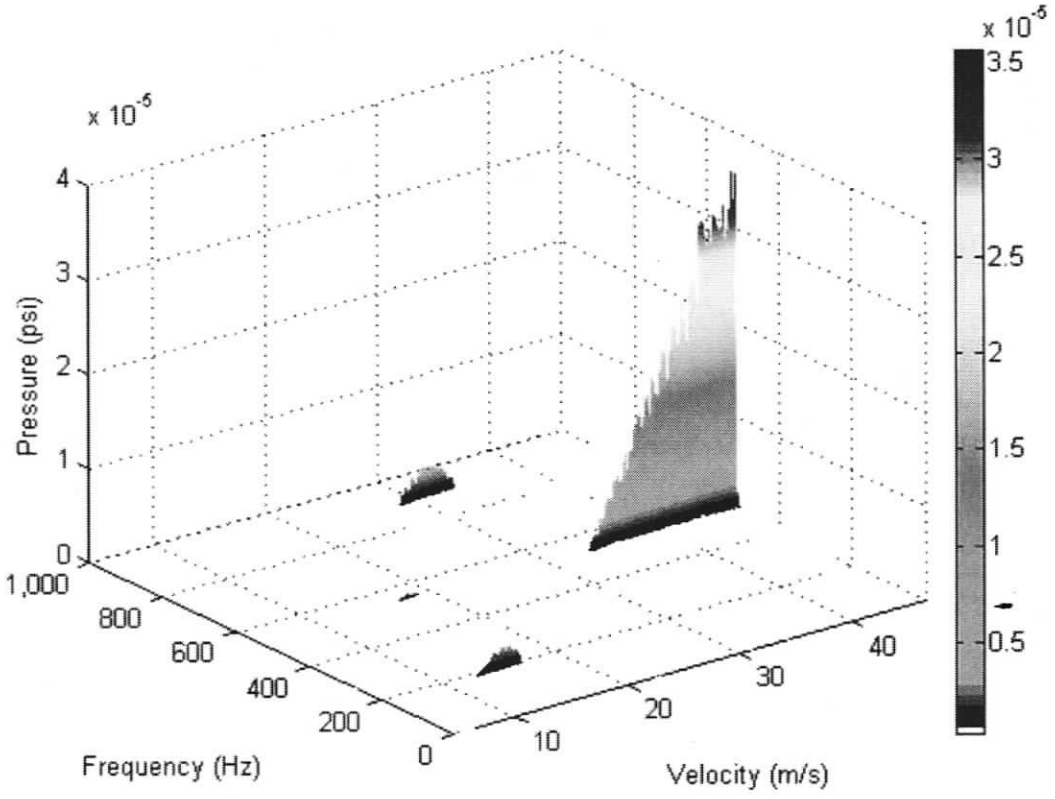

Figure 3.2: Pressure spectra measured at the closed end of the side branch as a function of the mean flow velocity for the case of the wide main duct ($D/L = 0.5$).

The same type of plot for the case of the narrow main duct is shown in Figure 3.3. Between $U = 40$ m/s and 50 m/s, strong subharmonic components are clearly observed in the pressure spectra. The acoustic oscillation within this range of flow velocities is classified as a quasi-locked-on regime [8].

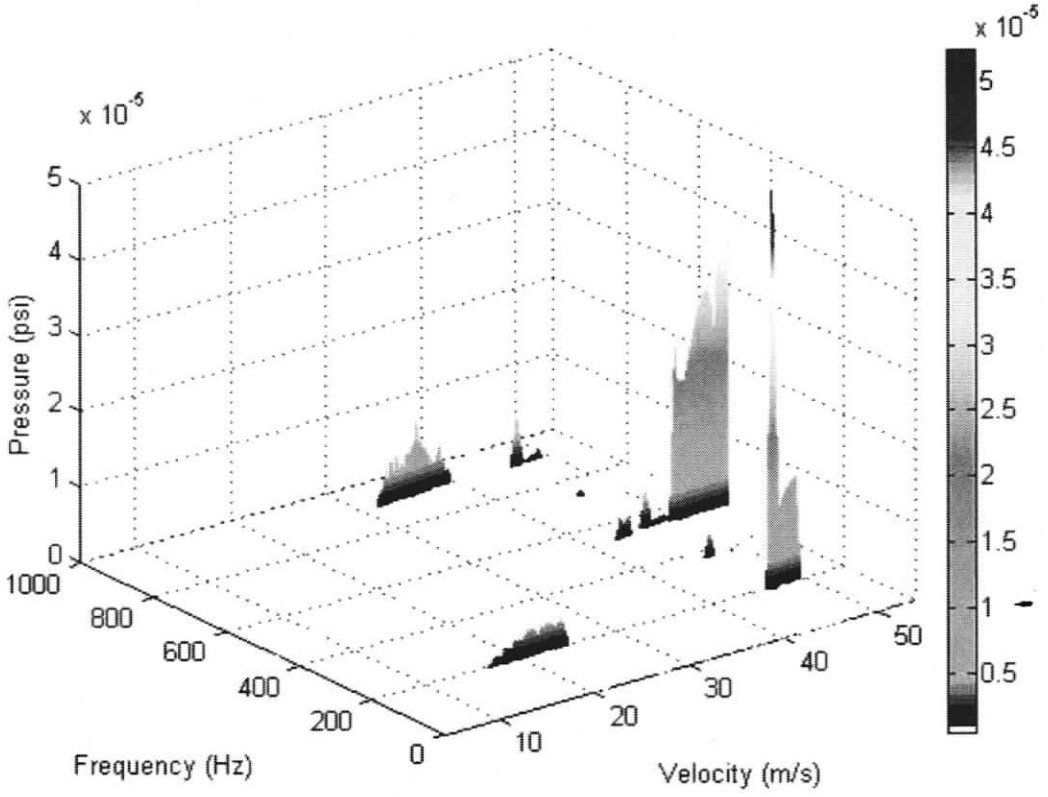

Figure 3.3: Pressure spectra measured at the closed end of the side branch as a function of the mean flow velocity for the case of the narrow main duct ($D/L = 0.25$).

The frequency and the pressure amplitude for the case of the wide main duct are plotted in Figure 3.4 as functions of the main flow velocity. The data points shown in the plot correspond to the points of maximum pressure amplitude at each velocity value. It is observed that when the resonance occurs, it is not associated with a single value of velocity, but rather with a range of velocities. There exists a minimum threshold velocity, which is required to excite the resonance. The resonance is observed to occur over three ranges of flow velocity. The range of resonance becomes wider as the velocity is increased. The weak resonance of the first acoustic mode dominate the acoustic field between $U = 10$ m/s and 17 m/s. Within this range, the pressure amplitude increases gradually with the flow velocity until it reaches the highest value of 3.5E-06 psi. After velocity reaches 14m/s, the oscillation amplitude decreases to approximately 0 psi. The fifth acoustic mode covers the

range of velocity between 28 m/s and 32 m/s. The oscillation amplitude of the fifth acoustic mode is slightly higher that of the first mode. At a point of U = 32 m/s, the resonant frequency suddenly jumps from f = 840 Hz to f = 545 Hz, which corresponds to the third acoustic mode. The pressure amplitude is significantly increased (by an order of magnitude) compared to the first and the fifth modes. The broken lines in the bottom plot correspond to the first two hydrodynamic oscillation modes (h =1 and 2 respectively) of the separated shear layers that exist across the mouths of the side branches. In the case of the first hydrodynamic oscillation mode, only one large-scale vortex forms in the shear layer during a typical oscillation cycle. The main resonance is excited by the first mode of shear layer instability. In the case of the second hydrodynamic mode (h = 2), the time required for each vortex to traverse the opening of the side branch corresponds to two typical oscillation periods. In other words, two large-scale vortices form in the opening of the side branch during a typical cycle of acoustic oscillations.

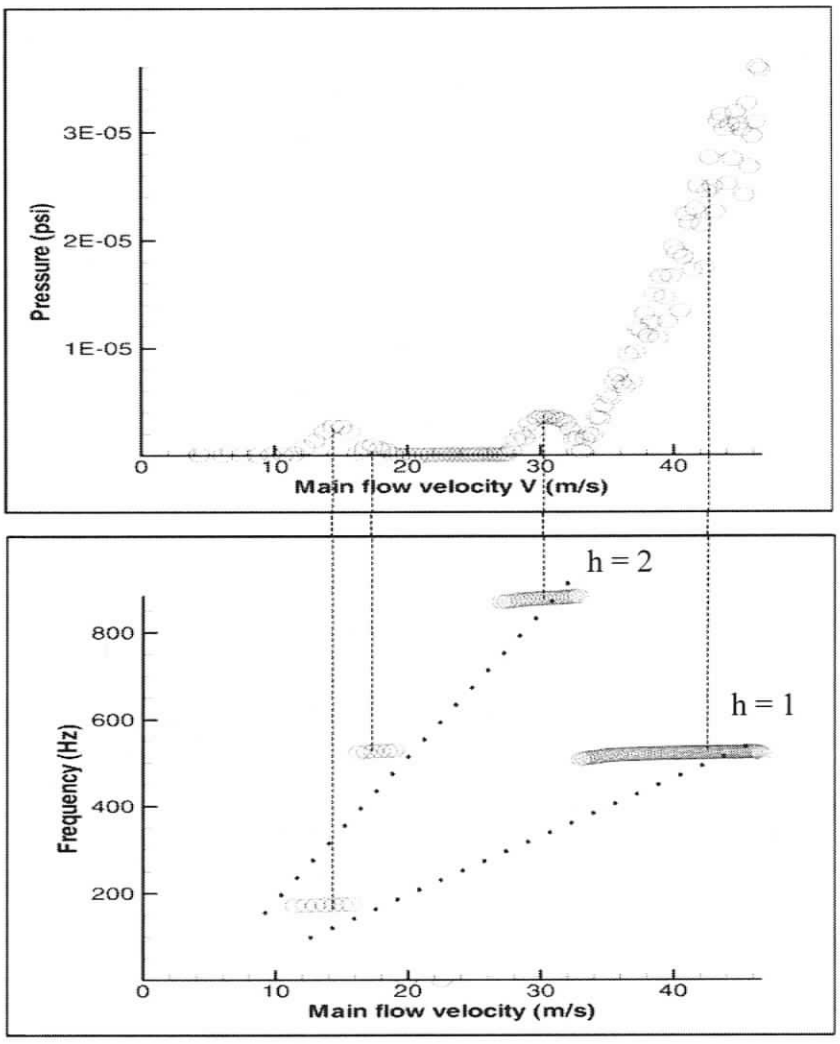

Figure 3.4: Amplitude of the pressure pulsations and frequency as functions of the mean flow velocity in the case of the wide main duct (D/L =0.5).

The acoustic response of the co-axial side branch resonator in the case of the narrow main duct (D/L = 0.25) is shown in Figure 3.5. It is noteworthy that the resonance amplitude increased as the ratio D/L decreased. The locked-on range is wider in comparison to that of the wide main duct. At each acoustic resonance mode, the onset of the resonances is delayed comparing with the wide main duct. The frequency jump that is observed in the bottom plot of Figure 3.5 between U = 43 m/s and 49 m/s, is a feature associated with a quasi-locked-on flow regime.

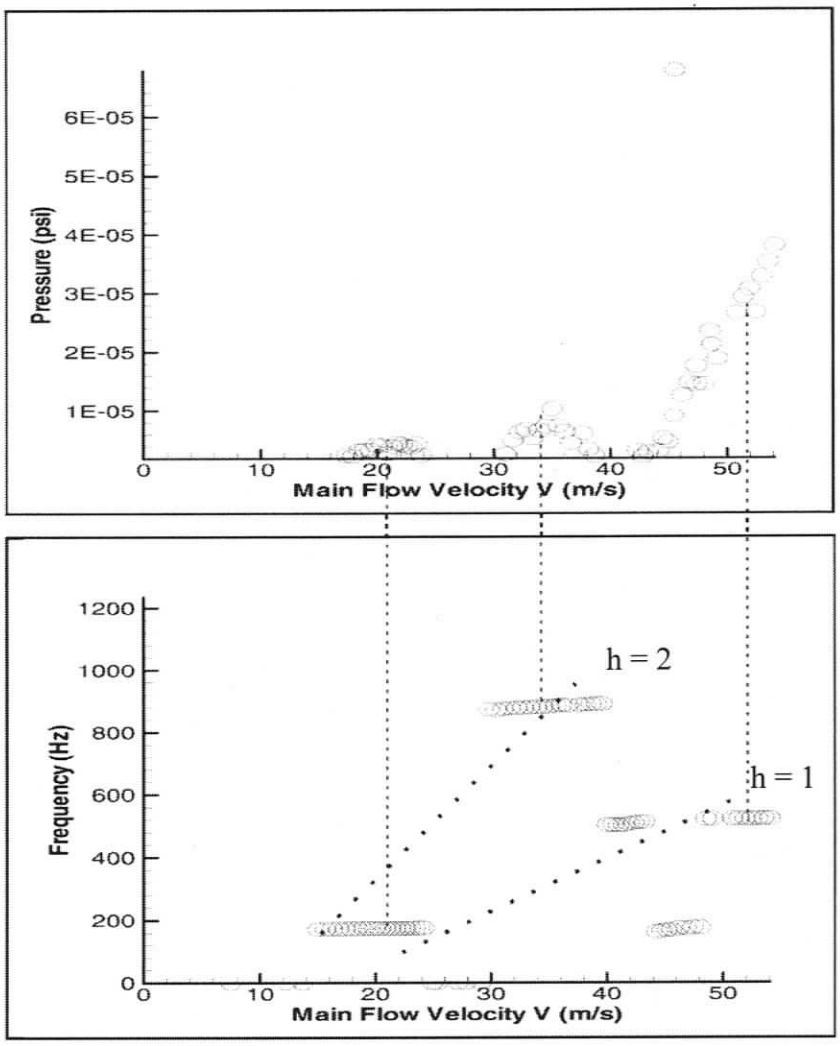

Figure 3.5: Amplitude of the pressure pulsations and frequency as functions of the mean flow velocity in the case of the narrow main duct (D/L =0.25).

Quantitative flow visualization experiments were conducted to investigate three distinct flow regimes for both the wide and the narrow main ducts, as described as following:

Case 1: Flow visualization of shear layer oscillations at the non-resonant case.

Case 2: Flow visualization of shear layer oscillations at the first hydrodynamic oscillation mode. Third resonant acoustic mode was exited during this regime.

Case 3: Flow visualization of shear layer oscillations at the second hydrodynamic oscillation mode. Fifth resonant acoustic mode was exited during this regime.

Figures 3.6 and 3.7 show the plots of acoustic pressure waveforms and their spectra for the case of the wide and the narrow main duct respectively in the non-resonant flow regime (Case 1). The data shown herein were acquired at the end of one of the side branches. Non-periodic signals of pressure fluctuations are observed in the wave plots. The spectra plots show the presence of harmonic components at several frequencies. There is no isolated dominant peak evident in the spectra plots.

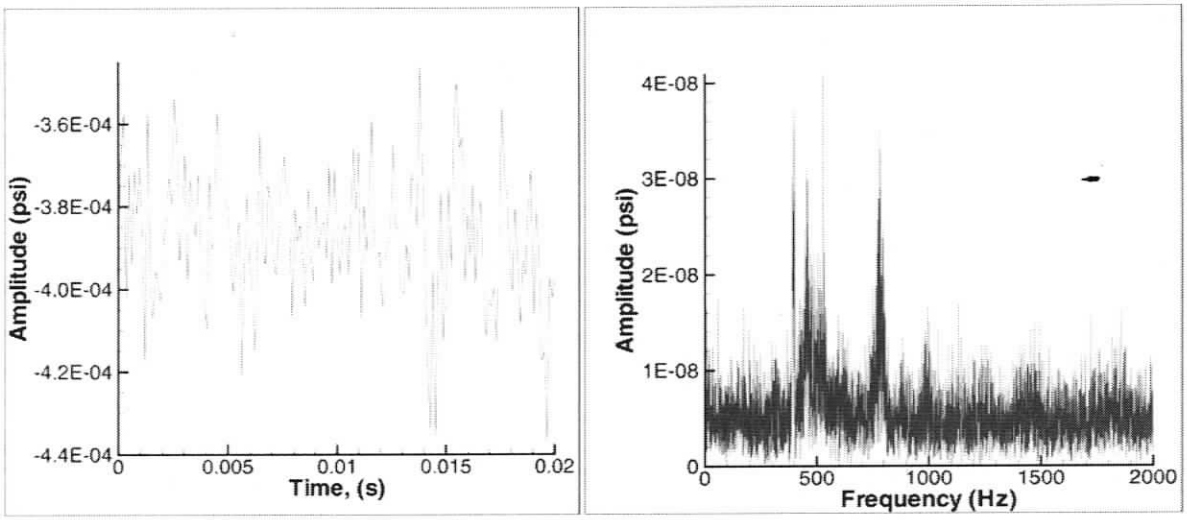

Figure 3.6: Pressure waveforms and spectra during non-resonant flow regime in the case of the wide main duct ($D/L = 0.5$).

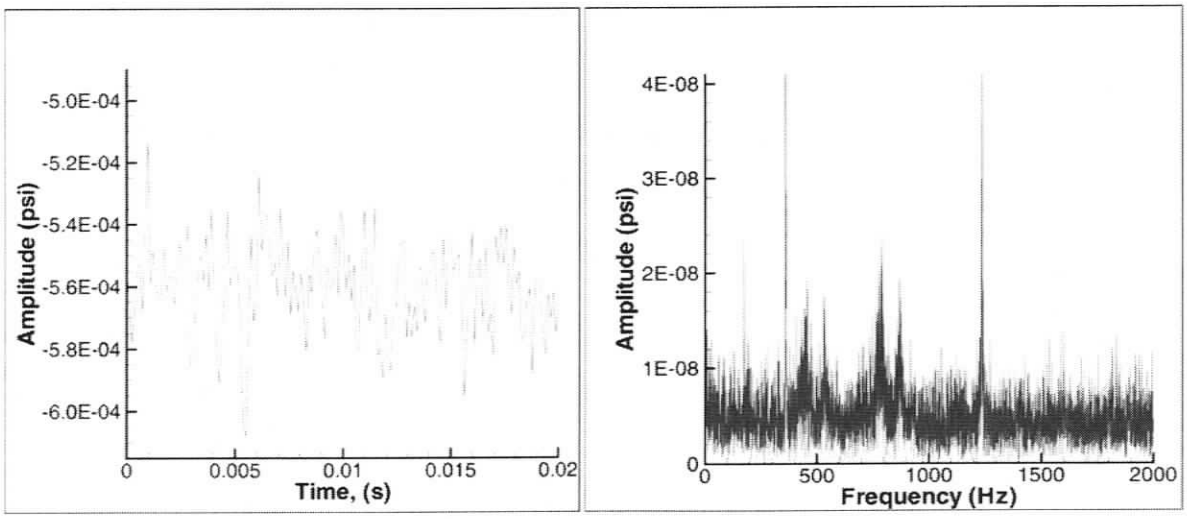

Figure 3.7: Pressure waveforms and spectra during non-resonant flow regime in the case of the narrow main duct ($D/L = 0.25$).

The plots of acoustic pressure waveform and its spectrum for the wide main duct at the first hydrodynamic oscillation mode (Case 2) are given in Figure 3.8. This flow regime corresponds to a strong resonance case. The dominant pressure peak is observed at a frequency of 545 Hz. It corresponds to a sinusoidal acoustic pressure waveform. The pressure amplitude is 1.2E-03 psi. Two higher-order harmonic components are observed in the spectrum plot.

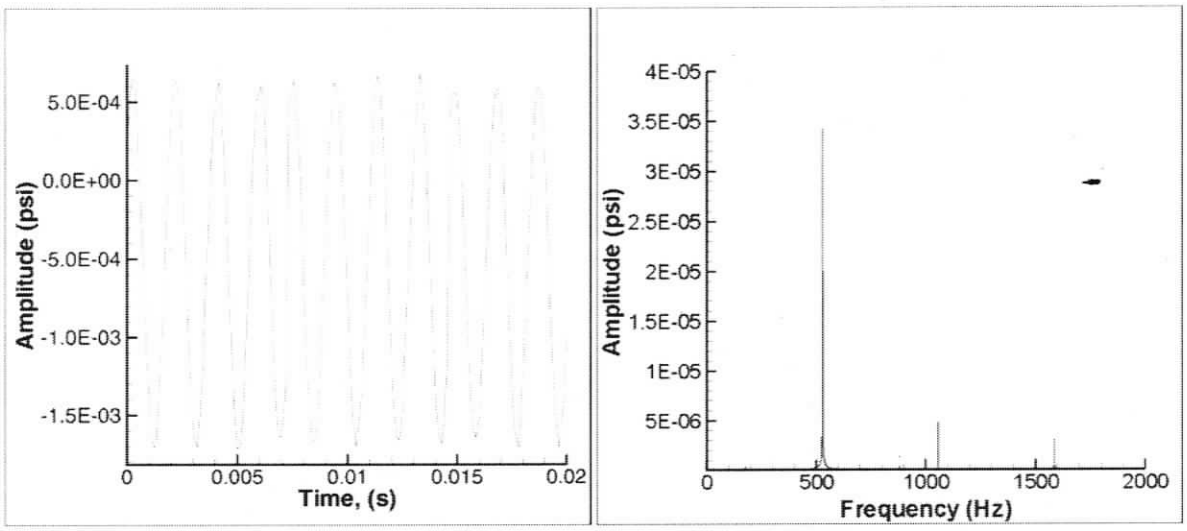

Figure 3.8: Pressure waveforms and spectra during the first hydrodynamic oscillation mode in the case of the wide main duct ($D/L = 0.5$).

Figure 3.9 shows the acoustic response of the narrow channel at the first hydrodynamic oscillation mode (Case 2). The peak acoustic pressure amplitude of 2.7E-03 psi is higher than that of the wide channel case. This suggests that the width of the main duct has a significant effect on the generation of acoustic noise. When the ratio between the main duct width and the side branch width is decreased, the pulsation amplitude increases. This observation is in agreement with the results reported by Jungowski *et al.* [12]. The peak in the spectrum plot clearly indicates the excitation of the third acoustic mode at $f =$ 545 Hz. Harmonics of this peak are either very small or indistinguishable.

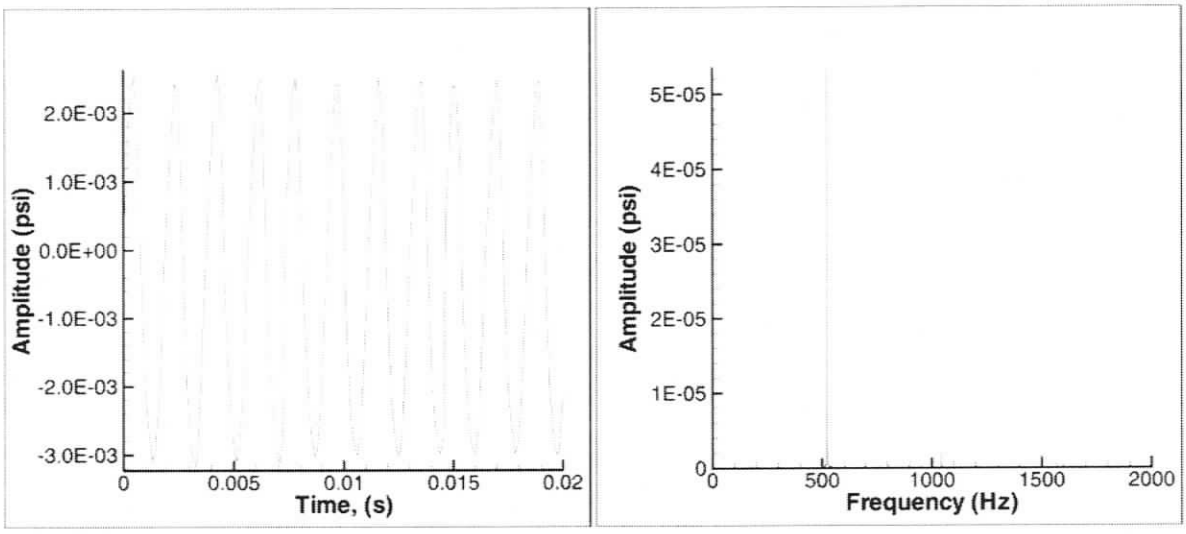

Figure 3.9: Pressure waveforms and spectra during the first hydrodynamic oscillation mode in the case of the narrow main duct (D/L = 0.25).

At the second hydrodynamic oscillation mode (Case 3) for the case of the wide main duct, plots of Figure 3.10 show that the pressure wave signal is not perfectly sinusoidal. The pressure amplitude is approximately 3.0E-04 psi, which is lower in comparison to that of Case 2. The spectral peak corresponds to the resonant frequency of the fifth acoustic mode (f = 840 Hz.) Strong resonance at f = 840 Hz is observed in the plots of Figure 3.11, which correspond to acoustic response of the narrow main duct at the second hydrodynamic oscillation mode (Case 3). It is evident that the acoustic pressure signal is more periodic and has higher oscillation amplitude compared to the case of the wide main duct.

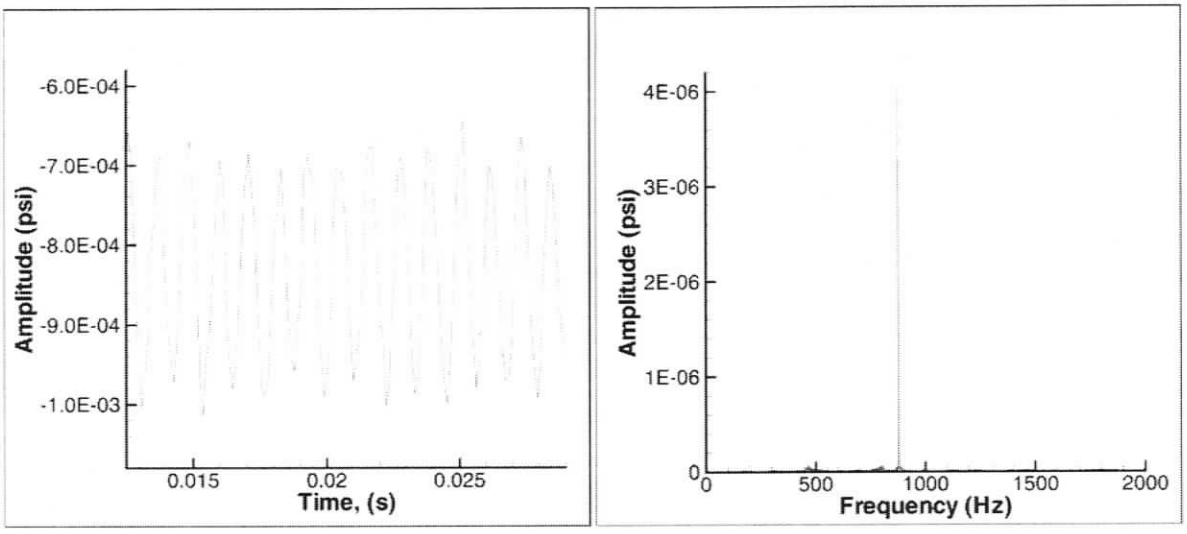

Figure 3.10: Pressure waveforms and spectra during the second hydrodynamic oscillation mode in the case of the wide main duct ($D/L = 0.5$).

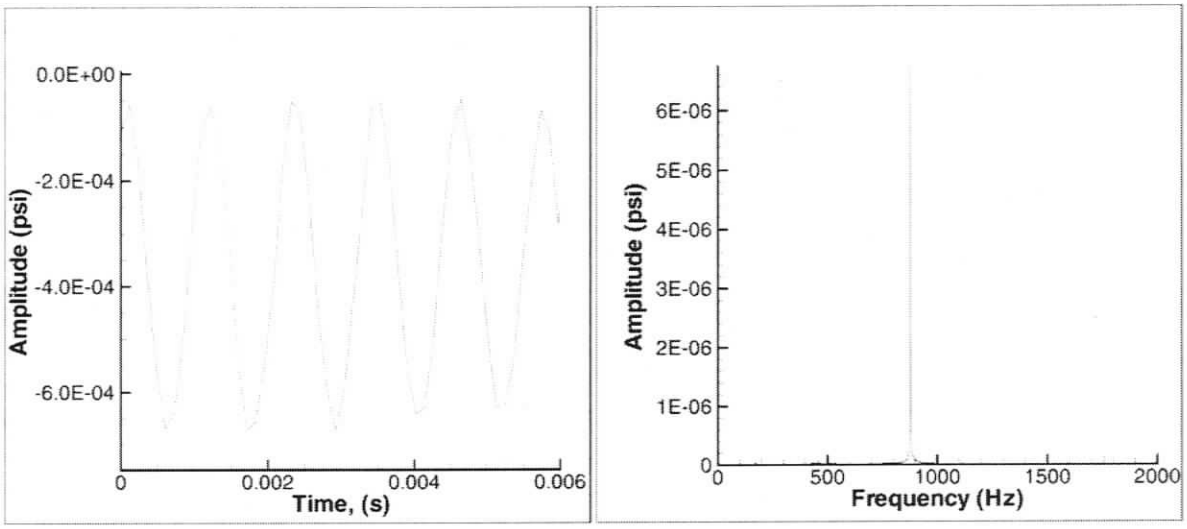

Figure 3.11: Pressure waveforms and spectra during the second hydrodynamic oscillation mode in the case of the narrow main duct ($D/L = 0.25$).

3.2 Instantaneous Flow Patterns

3.2.1 Instantaneous flow patterns at the non-resonant flow regime

Figure 3.12 shows the instantaneous velocity $\underline{V}$ and vorticity ω_z for the case of the wide main duct at the main velocity U = 20 m/s (non-resonant flow regime.) In this case, there is no acoustic flux inside the side branches. The pressure pulsations at the end of side branches are out-of-phase. The shear layer exhibits purely hydrodynamic oscillations. Instantaneous patterns of velocity and vorticity show that unsteady vortical structures of multiple scales are present in the top and bottom shear layers. The small-scale Kelvin-Helmholtz vortices that initially form in the separated shear layers in the vicinity of the upstream corners of the side branch resonator eventually impinge upon the downstream corner. The vorticity plot shows that the two shear layers oscillate symmetrically. The low level of incursions of the shear layers into the side branches is observed. This is a characteristic feature of the absence of resonant interaction of hydrodynamic structures with the acoustic field.

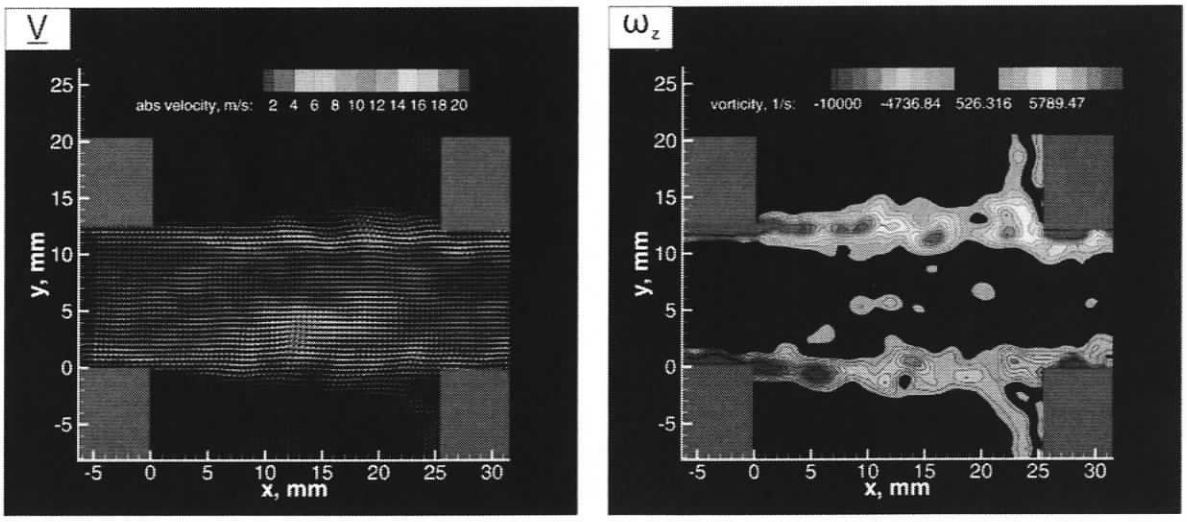

Figure 3.12: Instantaneous streamwise flow patterns corresponding to non-resonant flow regime for the case of the wide main duct (D/L = 0.5).

Figure 3.13 corresponds to the instantaneous flow patterns for the case of the narrow main duct within the non-resonant range. Symmetric flow patterns are evident in the vorticity plot. Due to the increased interaction between the two shear layers, the peak vorticity levels are higher than those in the case of the wide main duct.

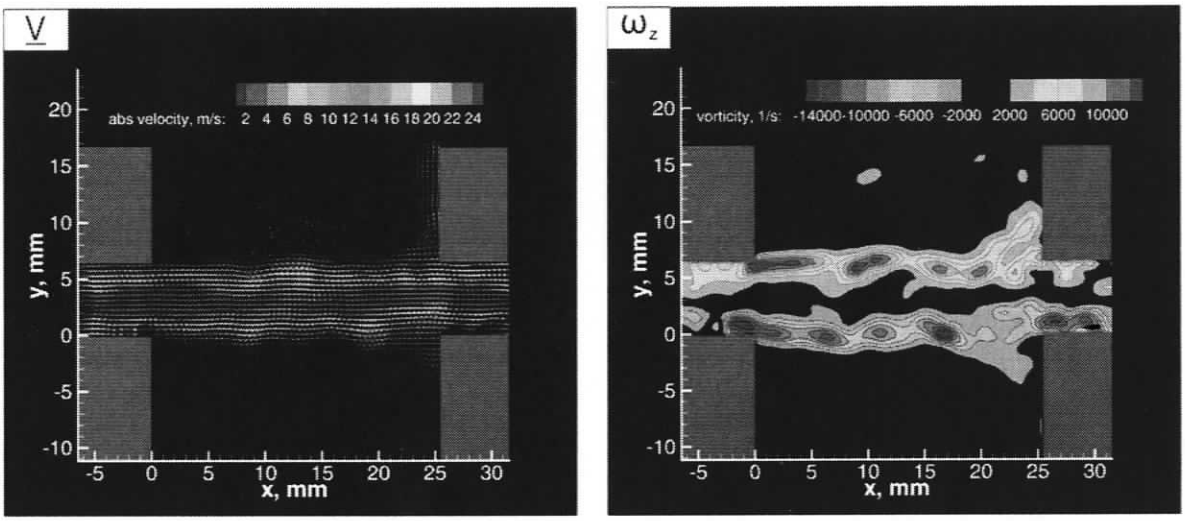

Figure 3.13: Instantaneous streamwise flow patterns corresponding to non-resonant flow regime for the case of the narrow main duct ($D/L = 0.25$).

3.2.2 Instantaneous flow patterns at the first hydrodynamic oscillation mode

When the resonance is excited, the symmetrical oscillation of the shear layer switches to antisymmetrical periodic oscillation mode. Instantaneous images of flow velocity $\underline{V}$ and out-of-plane vorticity ω_z for the case of the wide duct ($D/L = 0.5$), where the main resonance is excited, are shown in Figure 3.14. The images correspond to a phase in the acoustic oscillation cycle, which is indicated by a circle in the inset schematic. The mean flow velocity is 38m/s and the acoustic frequency $f = 545$ Hz, which yields a Strouhal number of $\mathrm{Sr} = fL/U = 0.36$. The observed value of the dimensionless acoustic velocity U_{ac}/U for this case is equal to 0.0005.

The vorticity plot shows that the shear layer oscillation coupling with an acoustic mode drastically increases the oscillation amplitude. The instability acoustic waves result

in rollup of the shear layer into larger-scale structures as they are convected downstream along the mouth of the side branch. These large-scale vortices generally have lower peak vorticity than the original Kelvin-Helmholtz vortices, but possess greater energy due to larger circulation values and increased convective speed. Images presented herein correspond to the first hydrodynamic mode of the shear layer oscillation, when one large-scale vortex forms in the shear layer during a typical oscillation cycle.

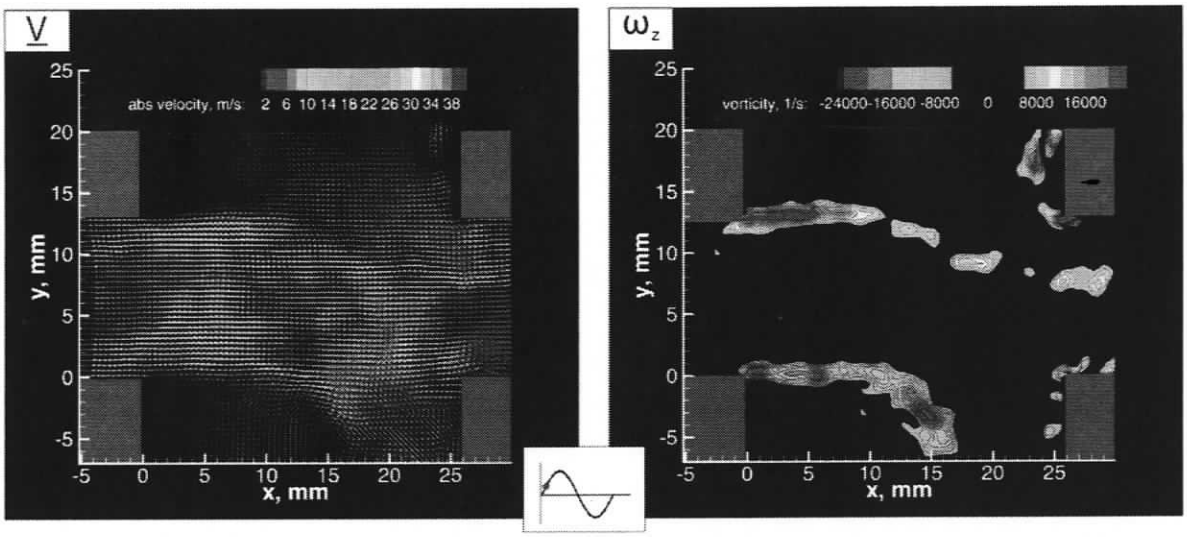

Figure 3.14: Instantaneous streamwise flow patterns corresponding to the first hydrodynamic oscillation mode for the case of the wide main duct. The corresponding phase of acoustic oscillation is indicated in the central insets. (D/L = 0.5, Sr = 0.36, U_{ac}/U = 0.0005).

When the main duct is relatively wide, as shown in Figure 3.14, the two shear layers that form across the top and bottom side branches do not interact with each other and impinge upon the downstream corners of the corresponding side branches. In this case, the coaxial side branch resonator can be represented as two independent single side branches in terms of the structure of the acoustic source.

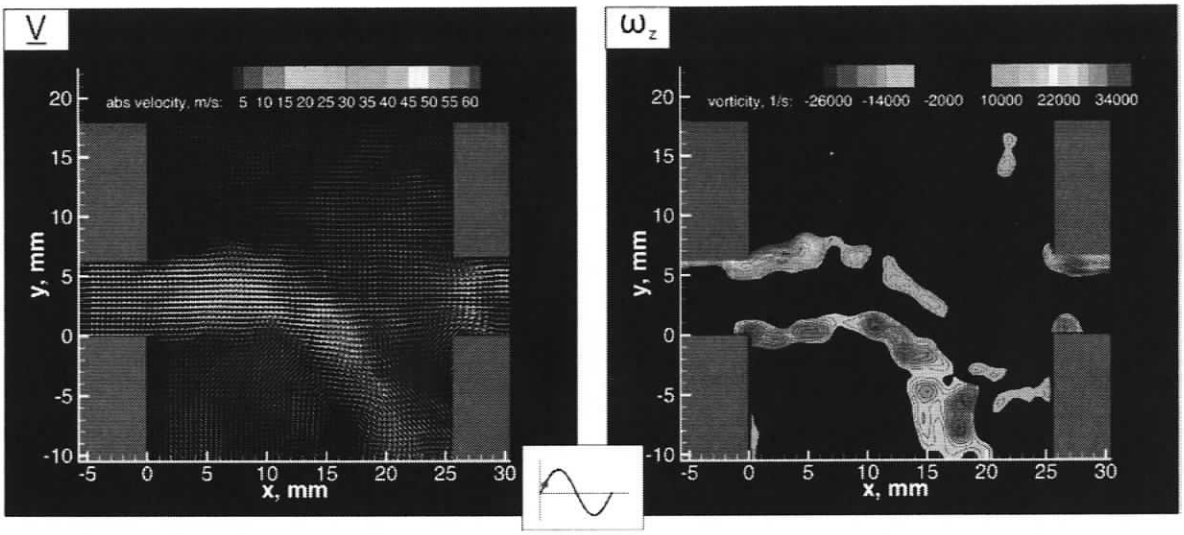

Figure 3.15: Instantaneous streamwise flow patterns corresponding to the first hydrodynamic oscillation mode for the case of the narrow main duct. The corresponding phase of acoustic oscillation is indicated in the central insets. (D/L = 0.25, Sr = 0.28, U_{ac}/U = 0.001).

This situation is in marked contrast to the shear layer interaction that occurs at the lower value of the main duct width (D/L = 0.25) shown in Figure 3.15, where the Strouhal number Sr = 0.28 and the dimensionless acoustic velocity U_{ac}/U = 0.001. When the main duct width is sufficiently low, the bottom shear layer can interact with the top shear layer. This flow behavior suggests that the structure of the acoustic power source will change significantly as the main duct width is decreased.

3.2.3 Instantaneous flow patterns at the second hydrodynamic oscillation mode

Figure 3.16 shows the instantaneous velocity field and corresponding out-of-plane vorticity for the wide main duct (D = 12.7 mm) at the second hydrodynamic oscillation mode, when the side branch resonators are excited at the fifth acoustic mode (f = 840 Hz.) The mean flow velocity is 26 m/s, which corresponds to the Strouhal number of Sr = fL/U = 0.82. The maximum dimensionless value of the one-dimensional acoustic velocity U_{ac}/U for this case is 0.00017. In contrast to the first hydrodynamic mode, where only one large-scale vortex is observed in the upper or lower shear layer, two vortices are formed in each

shear layer during a typical oscillation cycle. The vorticity plot of Figure 3.16 shows lower values of peak vorticity compared to the first hydrodynamic mode (the predominant oscillation mode) shown in Figure 3.14. In addition, the transverse undulations of the shear layers exhibit lower amplitude compared to the first hydrodynamic mode

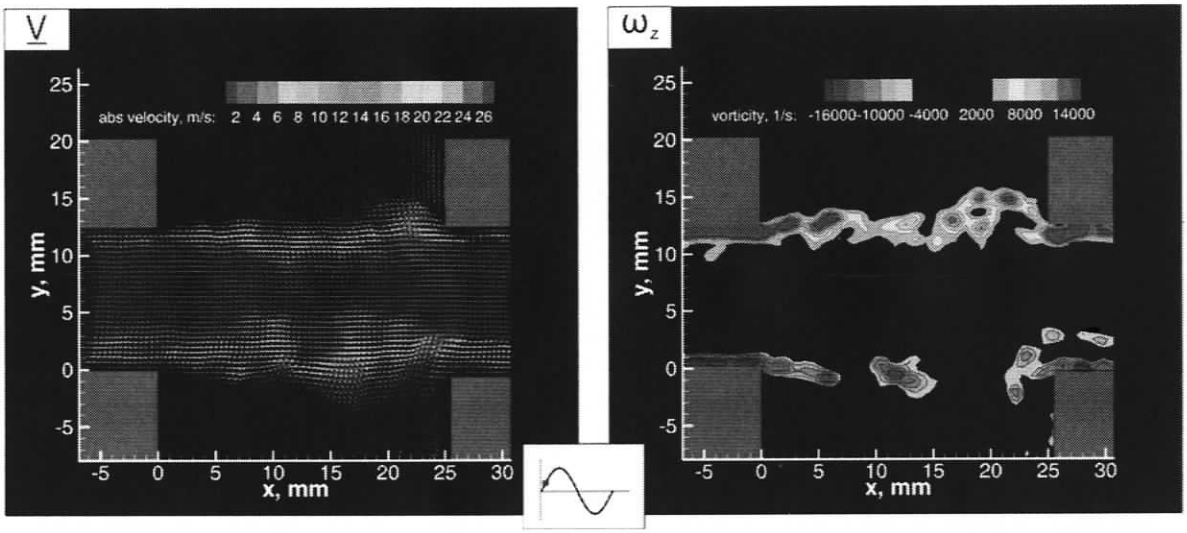

Figure 3.16: Instantaneous streamwise flow patterns corresponding to the second hydrodynamic oscillation mode for the case of the wide main duct. The corresponding phase of acoustic oscillation is indicated in the central insets. (D/L = 0.5, Sr = 0.82, U_{ac}/U = 0.00017).

In the case of the narrow main duct, Figure 3.17 shows the increased interaction between the upper and lower shear layers. Another feature of the vorticity pattern is the presence of two well-defined vortices that span the mouth of the side branch resonator. The pressure amplitude is 0.0006 psi, which corresponds to the dimensionless value of the acoustic velocity U_{ac}/U = 0.00036. In comparison with the case of the wide main duct, the acoustic pressure is significantly increased, which suggests that the interaction between the shear layers results in more energy being released by the vortical structures.

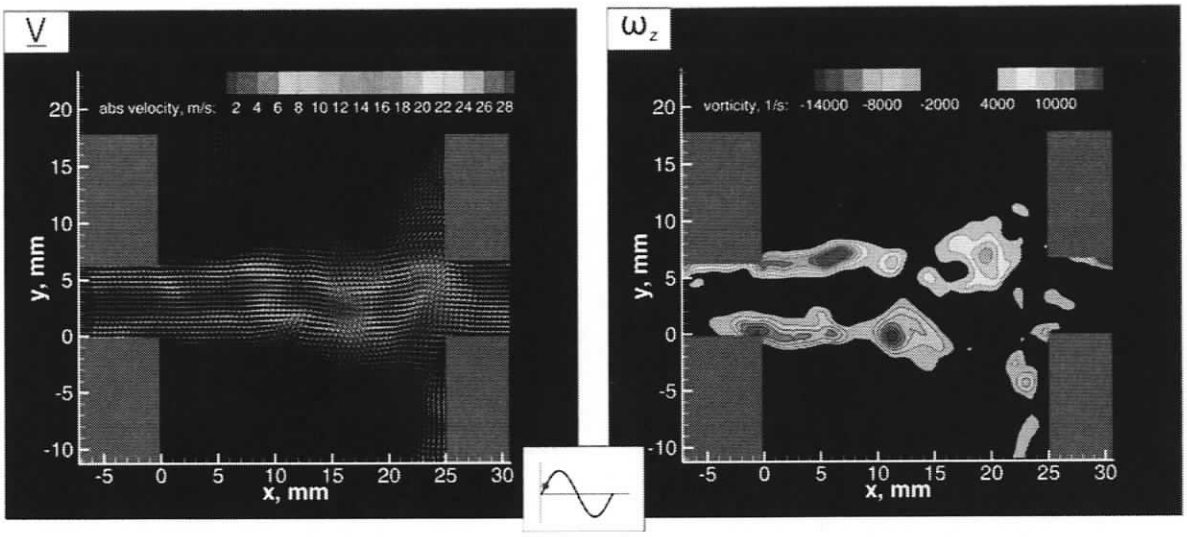

Figure 3.17: Instantaneous streamwise flow patterns corresponding to the second hydrodynamic oscillation mode for the case of the narrow main duct. The corresponding phase of acoustic oscillation is indicated in the central insets. (D/L = 0.25, Sr = 0.76, U_{ac}/U = 0.00036).

3.3 Phase-averaged Flow Patterns

3.3.1 Phase-averaged flow patterns at the first hydrodynamic oscillation mode

This experimental work employed phase-locking image acquisition techniques described in detail in Section 2. Implementation of real-time acoustic pressure analysis in conjunction with DPIV imaging resulted in a series of global quantitative images of the acoustically coupled flow that show formation and propagation of large-scale vortices during a typical acoustic cycle. Figure 3.18 shows the phase averaged flow patterns for the two values of the main duct width D at the phase of the acoustic cycle $\varphi = 10°$. The left and right columns of Figure 3.18 correspond to the values of D/L of 0.5 and 0.25 respectively. The images show plots of phase-averaged flow velocity $\langle \underline{V} \rangle_p$, vorticity $\langle \omega_z \rangle_p$, and streamline patterns (from top to bottom). At this phase, the acoustic velocity is directed into the upper side branch, and a new vortex is formed at the upstream edge of upper side branch (indicated in the vorticity plot). The vortex in the lower shear layer has been fully developed and convected downstream. The patterns of the streamline topology correspond

to the reference frame moving from left to right with the speed of $0.5U$, which approximates the average convective speed of the large-scale vortices in the shear layers. The plots show higher levels of circulation of the large-scale vortices in the case of the narrower main duct. In addition, the interaction between the vortical structures in the top and bottom shear layers is increased as the main duct becomes narrower.

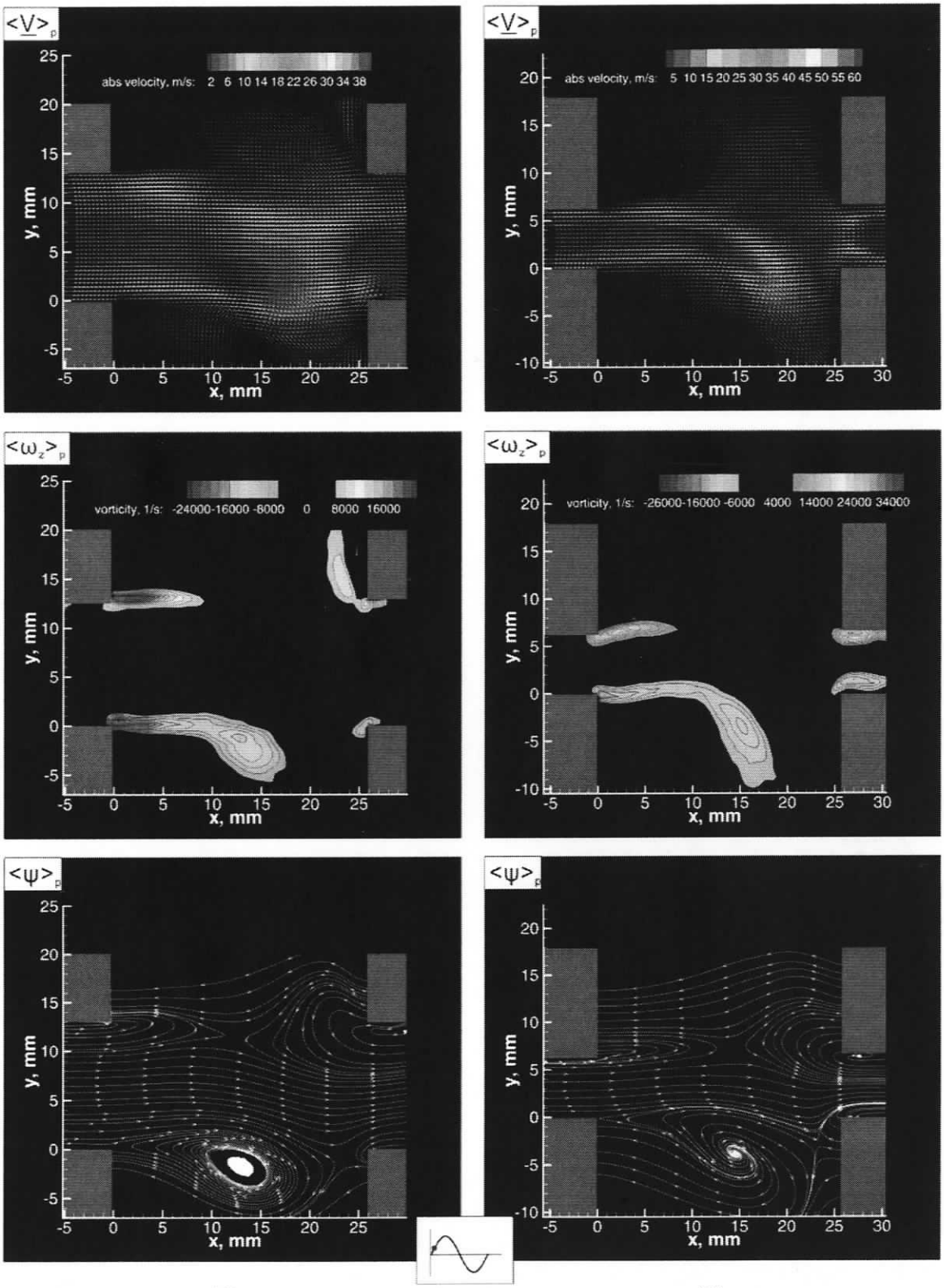

(a) **(b)**

Figure 3.18: Phase-averaged streamwise flow patterns corresponding to the first hydrodynamic oscillation mode at φ =10°. (a) Flow patterns for the case of the wide main duct (D/L = 0.5, Sr = 0.36, U_{ac}/U = 0.0005); (b) flow patterns for the case of the narrow main duct (D/L = 0.25, Sr = 0.28, U_{ac}/U = 0.001).

Figures 3.19 and 3.20 correspond to two subsequent phases of the acoustic oscillation cycle (φ=170° and φ=240° respectively). When the acoustic velocity changes sign, a new vortex starts to develop at the upstream edge of either the upper or the lower side branch. This vortex is then convected downstream, and its circulation is increased. For example, the images of Figure 3.19 illustrate the development of the vortex in the upper shear layer, which is shown in its initial stages of formation in Figure 3.18. At the later phase, shown in Figure 3.20, the positive vortex in the upper shear layer impinges on the downstream corner of the side branch. At the same time, a new negative vortex develops in the lower shear layer.

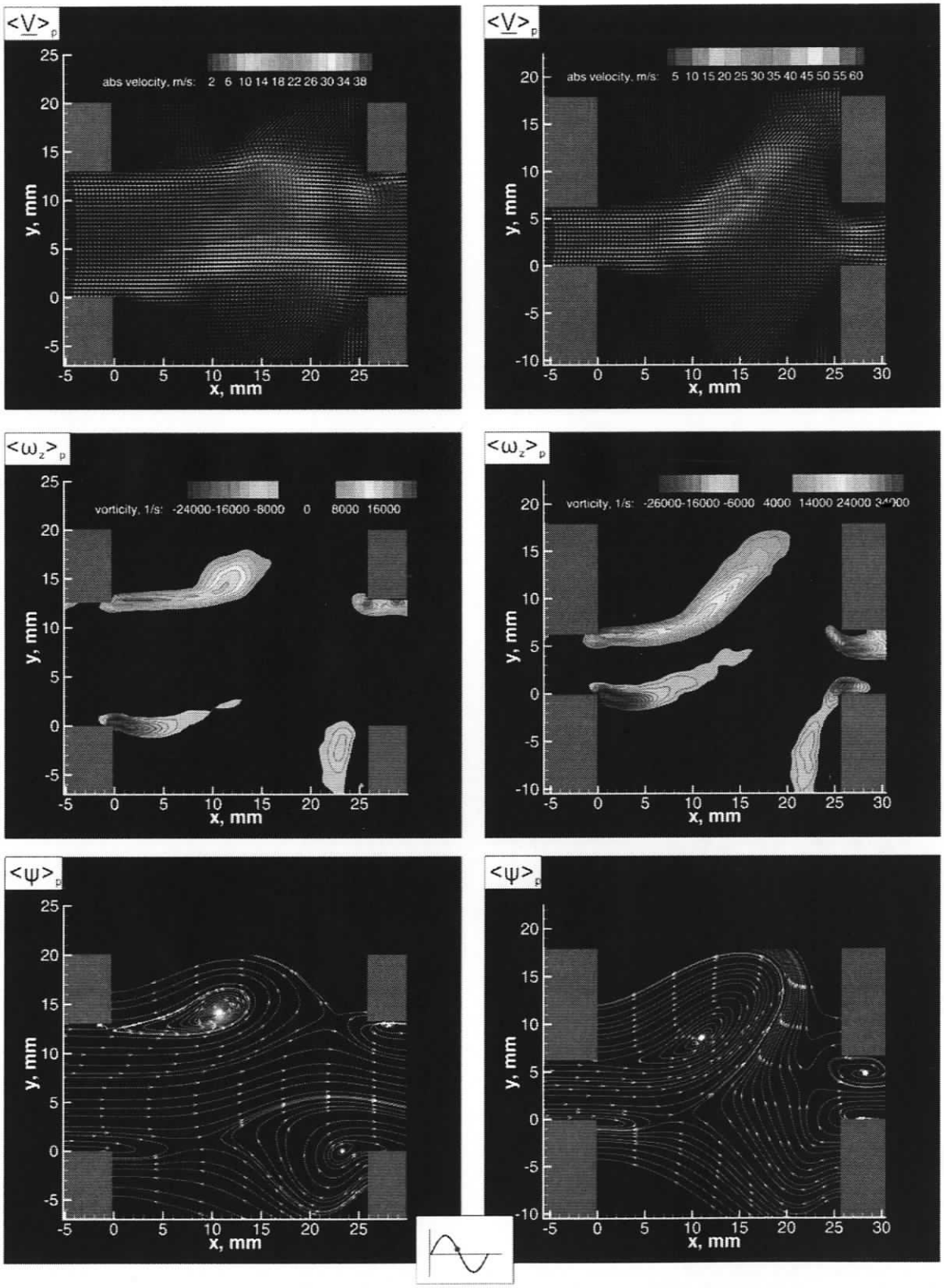

(a) **(b)**

Figure 3.19: Phase-averaged streamwise flow patterns corresponding to the first hydrodynamic oscillation mode at $\varphi = 170°$. (a) Flow patterns for the case of the wide main duct ($D/L = 0.5$, Sr = 0.36, $U_{ac}/U = 0.0005$); (b) flow patterns for the case of the narrow main duct ($D/L = 0.25$, Sr = 0.28, $U_{ac}/U = 0.001$).

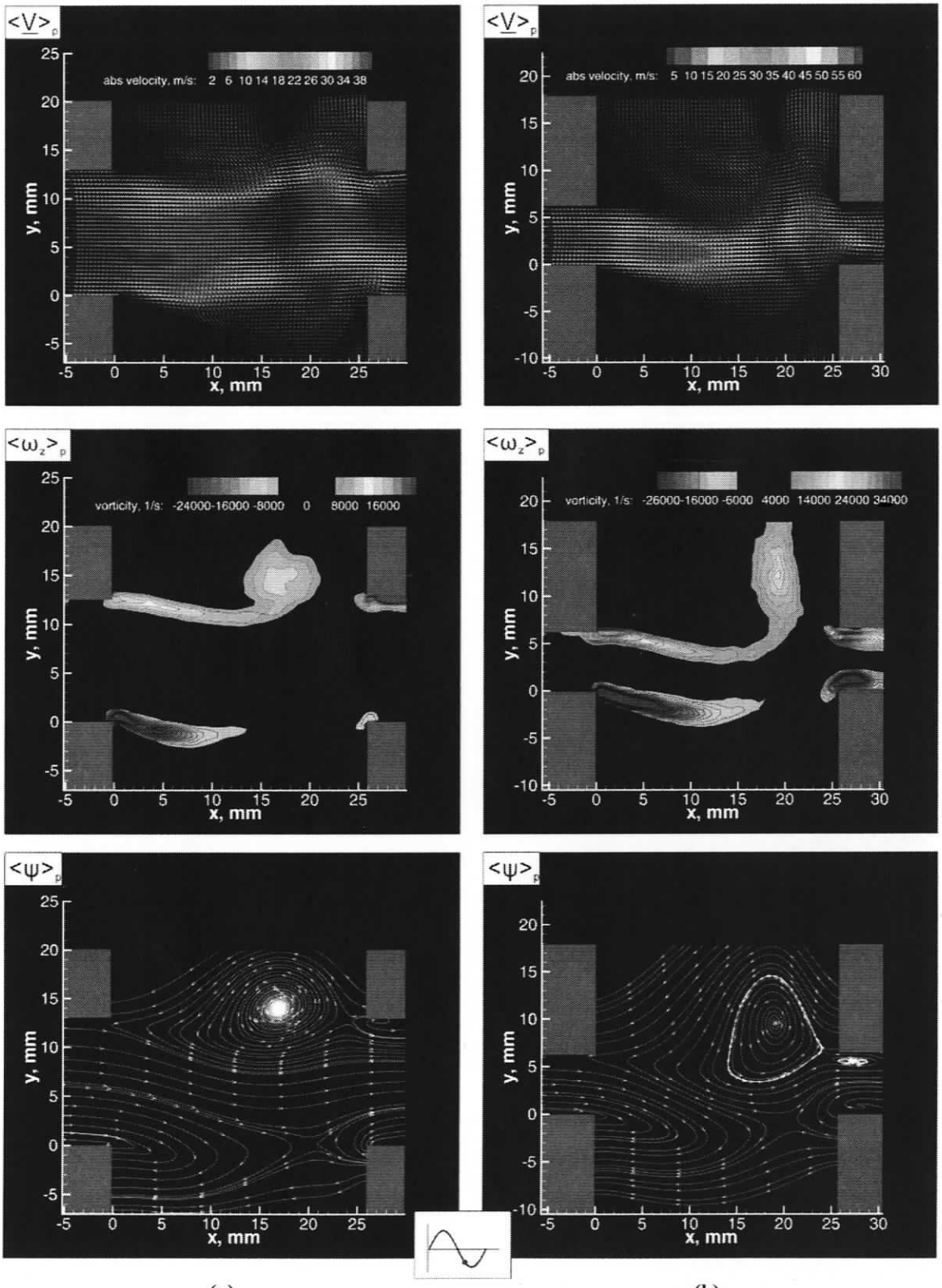

Figure 3.20: Phase-averaged streamwise flow patterns corresponding to the first hydrodynamic oscillation mode at $\varphi = 250°$. (a) Flow patterns for the case of the wide main duct ($D/L = 0.5$, Sr = 0.36, $U_{ac}/U = 0.0005$); (b) flow patterns for the case of the narrow main duct ($D/L = 0.25$, Sr = 0.28, $U_{ac}/U = 0.001$).

3.3.2 Phase-averaged flow patterns at the second hydrodynamic oscillation mode

The figures shown in this section correspond to the second hydrodynamic mode of the shear layer oscillation, when two large-scale vortices form in the shear layer. At the phase $\varphi = 10°$ (shown in Figure 3.21), the acoustic velocity is directed into the upper side branch. The vorticity plots in the second row show that the two vortices in the upper shear layer are pulled inside the branch by the acoustic flux. Meanwhile, the lower vortices are pushed out of the lower side branch. In the upper shear layer, the first vortex that is located near the upstream corner of the side branch is in the stage of development. The second vortex that has been formed completely is convecting along with the mean flow towards the trailing edge of the upper side branch. In the case of the narrow duct, the peak value of absolute vorticity is 14000/s, which is observed near the upstream edges of both side branches. The vorticity plot indicates that the circulation values are larger than those observed in the case of the wide duct. The well-defined vortices are apparently present over the cavity openings in this case. Since the acoustic pressures inside the co-axial side branches are 180° out-of-phase, the vorticies in the lower shear layer lead the vorticies in the upper shear layer in time by one half of an acoustic period. The large-scale vortex in the lower shear layer is located approximately 12 mm downstream of the leading edge. The distance between the centers of vorticies in the upper and lower shear layers is approximately 7 mm.

Figure 3.22 shows the flow features at $\varphi = 160°$. During the first half of the acoustic period, small-scale vorticity concentrations roll up into a large-scale vortex. The previously-formed large-scale vortex starts to interact with the downstream edge of the cavity. Since the total time required by a vortex to traverse the side branch opening is two

typical acoustic cycles, the convective speed of the vortices is such that the vortex traverses approximately a quarter of the side branch length during one half of the acoustic period. The convective speed of the vortices can be evaluated, for example, by considering the vorticity patterns in the upper shear layer. Dividing the distance between the estimated centers of the large-scale vortices shown in Figures 3.21 and 3.22 by the corresponding fraction of the acoustic period yields the average convection velocity of the vorticies to be approximately equal to 14 m/s. The ratio of the vortex convection velocity to the mean flow velocity is close to 0.5. Therefore, a reference frame moving with 0.5 U was used to identify the vortical structures in the streamline topology plots.

At the acoustic phase of φ = 250° (shown in Figure 3.23), the acoustic velocity reverses its direction and points out of the upper side branch. The vortices in the upper shear layer are forced downwards and a new vortex develops at the upstream edge of the lower side branch. The streamline patterns indicate that the interaction between the upper and lower shear layers in the vicinity of the separation region is less pronounced compared to the first shear layer oscillation mode.

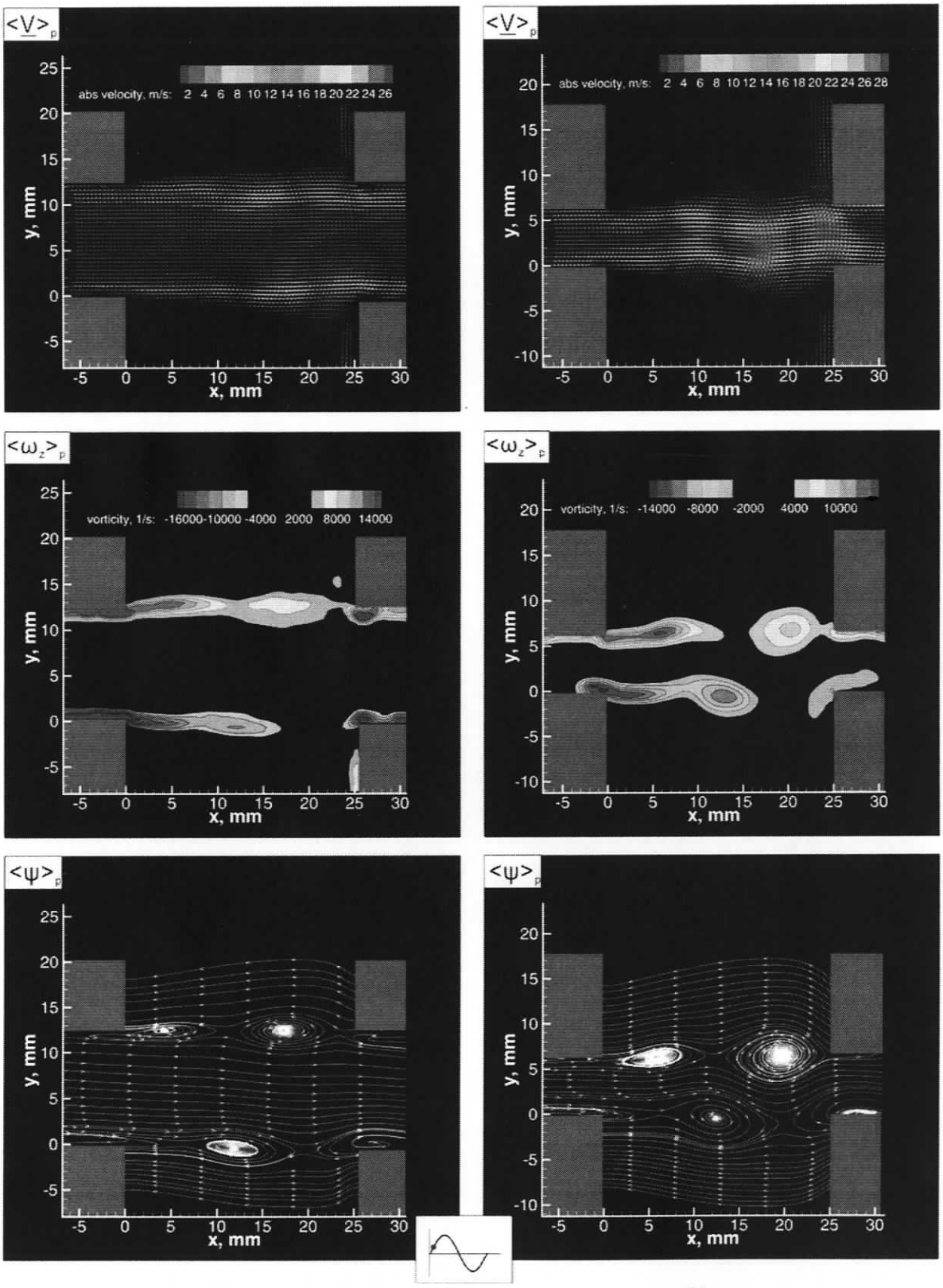

(a) **(b)**

Figure 3.21: Phase-averaged streamwise flow patterns corresponding to the second hydrodynamic oscillation mode at $\varphi = 10°$. (a) Flow patterns for the case of the wide main duct ($D/L = 0.5$, Sr = 0.82, $U_{ac}/U = 0.00017$); (b) flow patterns for the case of the narrow main duct ($D/L = 0.25$, Sr = 0.76, $U_{ac}/U = 0.00036$).

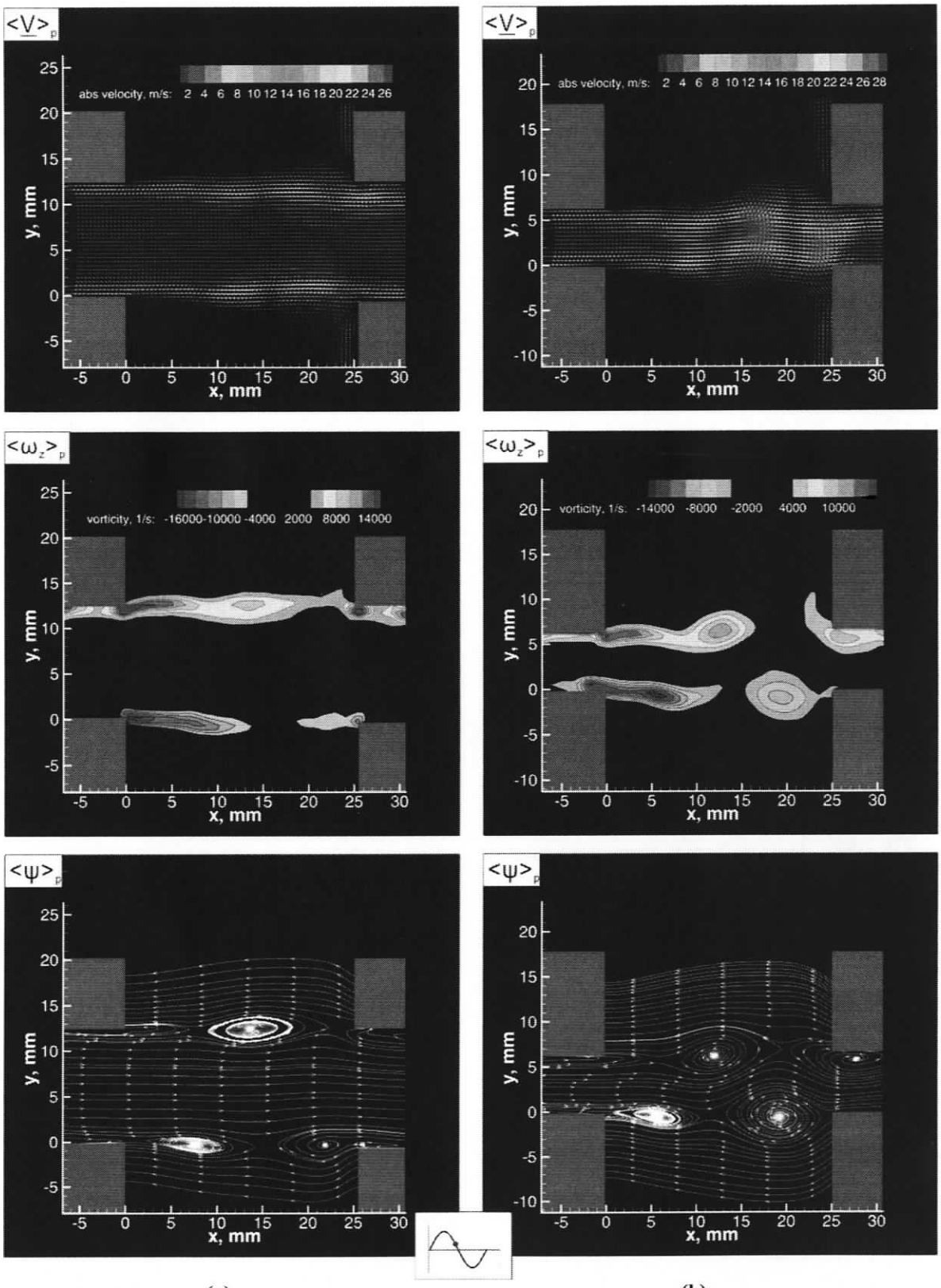

(a) **(b)**

Figure 3.22: Phase-averaged streamwise flow patterns corresponding to the second hydrodynamic oscillation mode at φ = 160°. (a) Flow patterns for the case of the wide main duct (D/L = 0.5, Sr = 0.82, U_{ac}/U = 0.00017); (b) flow patterns for the case of the narrow main duct (D/L = 0.25, Sr = 0.76, U_{ac}/U = 0.00036).

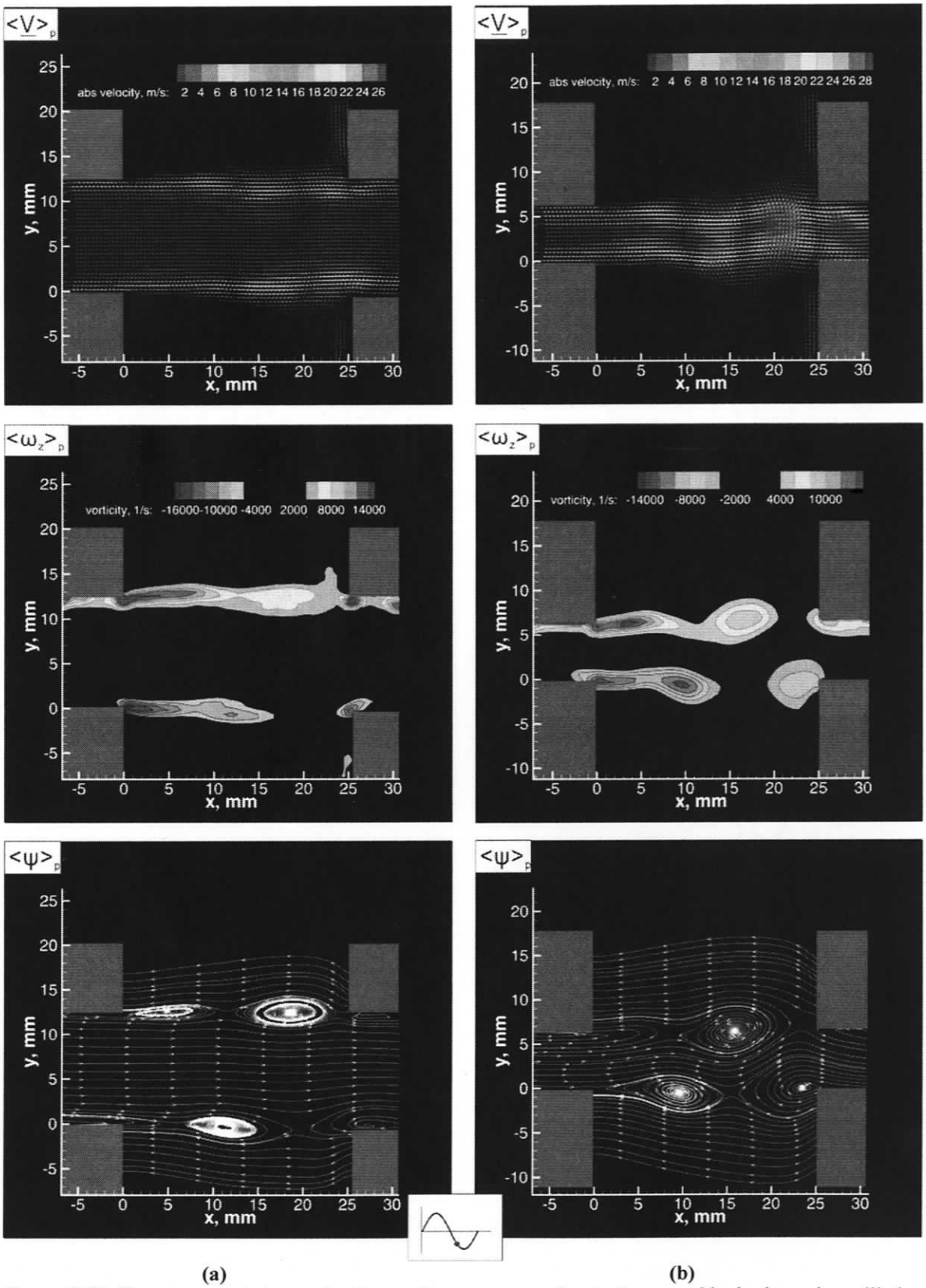

(a) **(b)**

Figure 3.23: Phase-averaged streamwise flow patterns corresponding to the second hydrodynamic oscillation mode at φ = 250°. (a) Flow patterns for the case of the wide main duct (D/L =0.5, Sr = 0.82, U_{ac}/U = 0.00017); (b) flow patterns for the case of the narrow main duct (D/L = 0.25, Sr = 0.76, U_{ac}/U = 0.00036).

3.4 Time-averaged Flow Patterns

3.4.1 Time-averaged flow patterns at the non-resonant flow regime

Time-averaged flow patterns at a non-resonant flow regime for the wide main duct are shown in Figure 3.24. Time-averaged images of streamwise velocity $\langle \underline{V} \rangle$ and out-of-plane vorticity $\langle \omega_z \rangle$ show that the shear layers are essentially horizontal. The distribution of the time-averaged turbulence statistics, such as the root-mean-square values of the velocity ($\langle u_{rms} \rangle$ and $\langle v_{rms} \rangle$) and Reynolds stress correlation ($\langle u'v' \rangle$) serves as an indicator of the region of the relative unsteadiness in the flow field. The $\langle u_{rms} \rangle$ has relatively high values along the shear layer over the mouth of the side branches, which corresponds to the pronounced turbulence region. Significant values of $\langle v_{rms} \rangle$ occur in the region near the downstream corner. This indicates the fluctuations and distortions of large-scale vorticies in this region. The peak value of $\langle v_{rms} \rangle$ is 1.7 m/s, which is relatively low and is an indication of a non-resonant flow regime. The velocity correlation $\langle u'v' \rangle$, which corresponds to the dominant Reynolds shear stress component, has positive values in the upper shear layer. The opposite-signed contour is present at the lower side. The peak values of the elevated positive and negative contours are observed close to the downstream corners of the resonator, in the flow impingement region.

In the case of the narrow main duct, the time-averaged flow patterns clearly repeat the main features of the flow in the case of the wide main duct. The plots of turbulence statistics show that the interaction level between the two shear layers is low. This is due to the low oscillation amplitude of the shear layers during the non-resonant flow regime. The distributions of turbulence statistics shown in Figure 3.25 demonstrate a higher level of flow unsteadiness compared to the case shown in Figure 3.24.

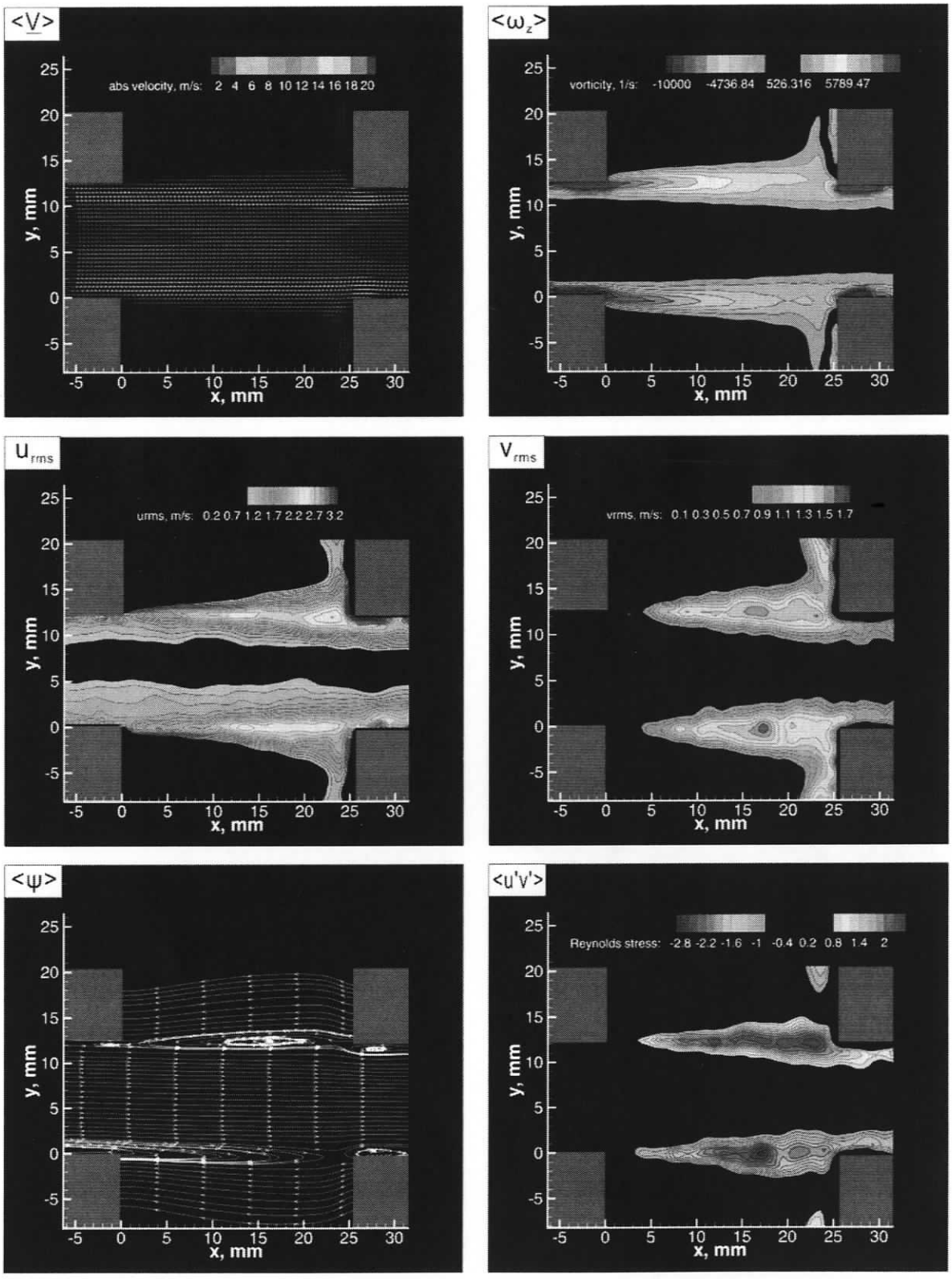

Figure 3.24: Time-averaged streamwise flow patterns corresponding to the non-resonant flow regime for the case of the wide main duct ($D/L = 0.5$).

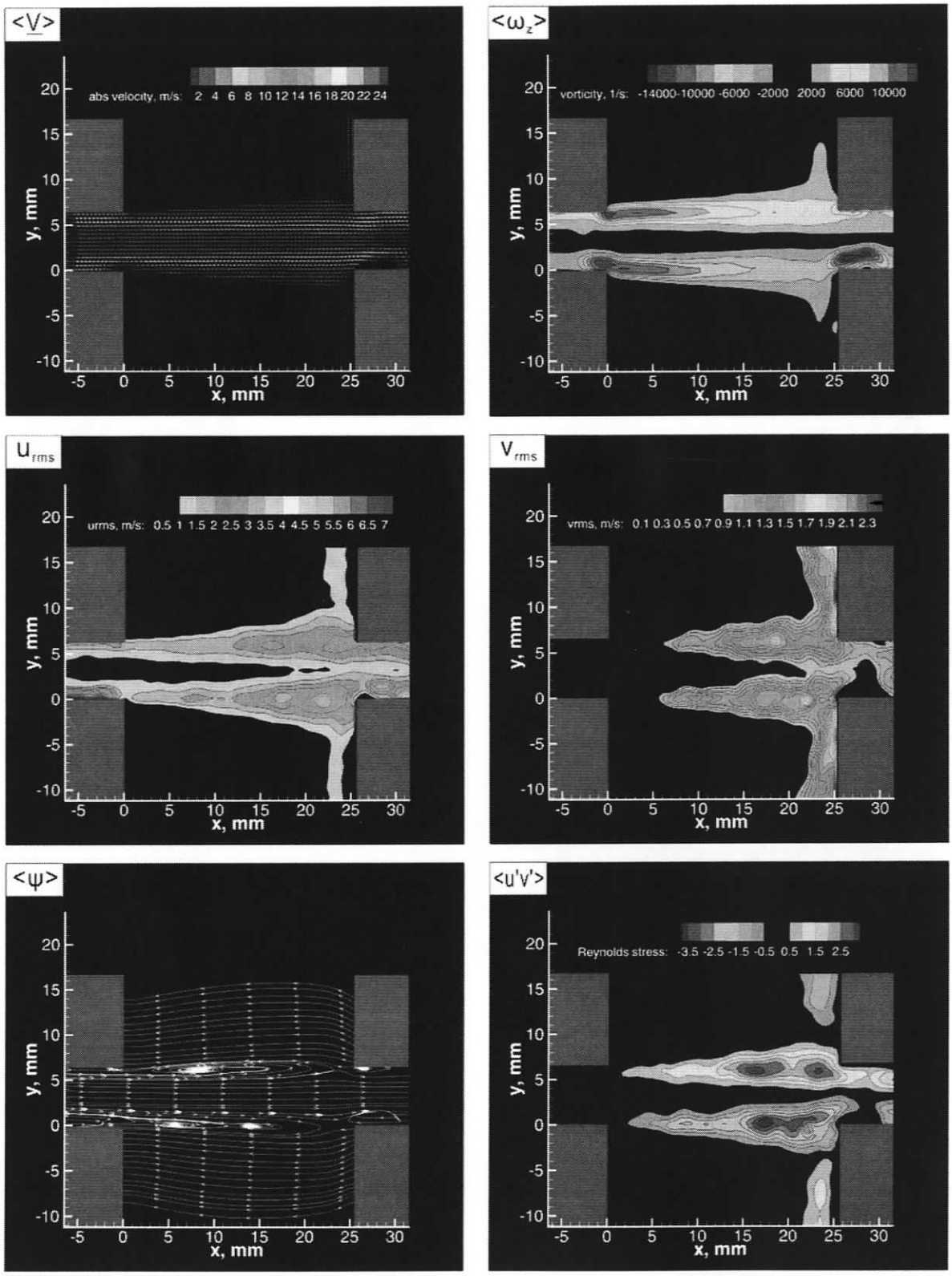

Figure 3.25: Time-averaged streamwise flow patterns corresponding to the non-resonant flow regime for the case of the narrow main duct ($D/L = 0.25$).

3.4.2 Time-averaged flow patterns at the first hydrodynamic oscillation mode

When the resonance sets in, the distributions of the time-averaged flow parameters for the two values of the main duct width illustrate the increased interaction between the top and bottom shear layers and a change in the structure of the acoustic source as the duct width decreases. For the case of the wide duct, represented in Figure 3.26, patterns of time-averaged flow velocity $<\underline{V}>$, out-of-plane vorticity $<\omega_z>$, and streamlines $<\Psi>$ indicate no interaction between the shear layers that form across the top and bottom side branches. For the case of the narrow channel, shown in Figure 3.27, these parameters indicate a more complex hydrodynamic behavior due to the relative proximity of the shear layers. Moreover, the large excursions of the shear layers into the side branches are evident in Figure 3.27. This pattern is characteristic to the first hydrodynamic mode of shear layer oscillations.

Distribution of the time-averaged turbulence statistics indicates that higher absolute values of these parameters correspond to the regions where the energy is extracted from the large-scale vortical structures and the acoustic noise is generated. Therefore, the plots of the turbulence statistics presented in Figures 3.26 and 3.27 suggest the spatial structure of the acoustic source for the two values of the main duct width.

When the main duct is sufficiently wide (Figure 3.26), the structure of the acoustic power source formed at the opening of each of the two side branches is unaffected by the presence of the other branch. Therefore, in terms of the acoustic source structure, the coaxial side branch resonator behaves as two independent side branches. However, for the case of the narrow duct (Figure 3.27), the coaxial resonator forms a single acoustic noise

source having a complex spatial structure, as indicated by the butterfly pattern in the plots of $\langle u_{rms} \rangle$, $\langle v_{rms} \rangle$, and $\langle u'v' \rangle$.

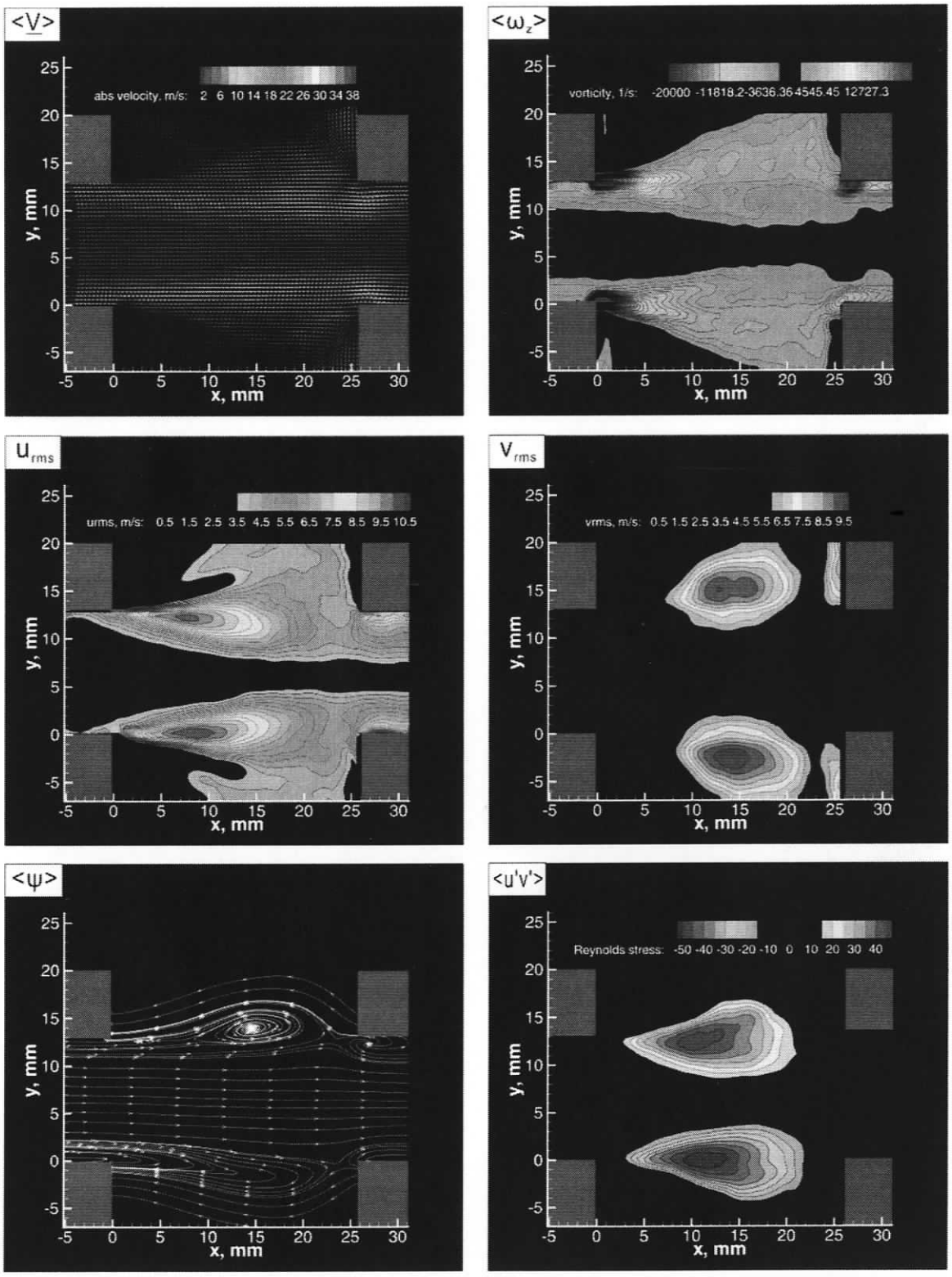

Figure 3.26: Time-averaged streamwise flow patterns corresponding to the first hydrodynamic oscillation mode for the case of the wide main duct (D/L = 0.5, Sr = 0.36, U_{ac}/U = 0.0005).

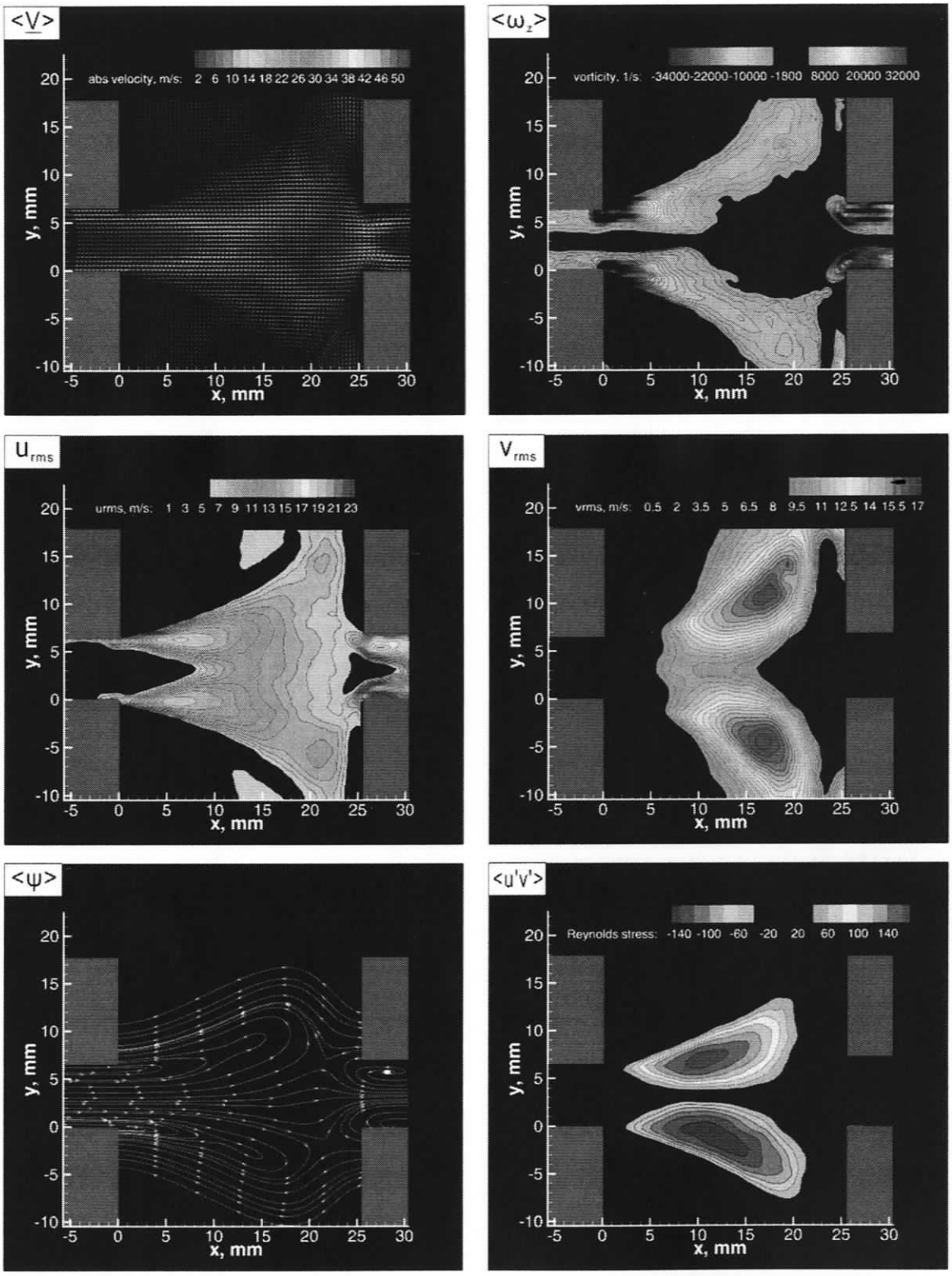

Figure 3.27: Time-averaged streamwise flow patterns corresponding to the first hydrodynamic oscillation mode for the case of the narrow main duct (D/L = 0.25, Sr = 0.28, U_{ac}/U = 0.001).

3.4.3 Time-averaged flow patterns at the second hydrodynamic oscillation mode.

Figures 3.28 and 3.29 show the time-averaged flow patterns at the second shear layer oscillation mode for the wide and narrow main ducts respectively. In Figure 3.28, time-averaged velocity $\langle \underline{V} \rangle$ and vorticity $\langle \underline{\omega} \rangle$ plots exhibit the symmetric flow patterns over the junction. The plots of turbulence statistics indicates that the values of $\langle u_{rms} \rangle$, $\langle v_{rms} \rangle$, and $\langle u'v' \rangle$ are one order of magnitude lower in comparison with the first hydrodynamic mode. The plot of $\langle u_{rms} \rangle$ shows that significant values of $\langle u_{rms} \rangle$ occur in the shear layer immediately downstream of the leading edge of the side branches. Increasingly larger region of higher level $\langle u_{rms} \rangle$ are observed further downstream. The velocity fluctuation in the vertical direction, $\langle v_{rms} \rangle$, is a parameter that serves as the indicator of the region where the interaction between the acoustic field and the unstable shear layer occurs. The significant values of $\langle v_{rms} \rangle$ occur in the downstream region of the junction, which indicates that this region of flow involve significant energy exchange between the hydrodynamic and acoustic flow components. Discrete acoustic power sources are expected, since they are related to the structure of $\langle v_{rms} \rangle$ distribution. The peak values of the velocity correlation $\langle u'v' \rangle$ occur farther downstream comparing to the first hydrodynamic mode.

In the case of the narrow main duct, the plot of $\langle v_{rms} \rangle$ shows that a single contour is accompanied by two discrete sharp edges. The single contour of the $\langle v_{rms} \rangle$ suggests the presence of single acoustic noise structure close to the downstream edge of the cavity. The peak amplitude of the $\langle v_{rms} \rangle$ is 4.6m/s. The velocity correlation $\langle u'v' \rangle$ shows the presence of contours of the opposite sign in the junction area. Two small, roughly symmetric protrusions on the contours correspond to the two discrete sharp edges in the $\langle v_{rms} \rangle$ distribution mentioned above.

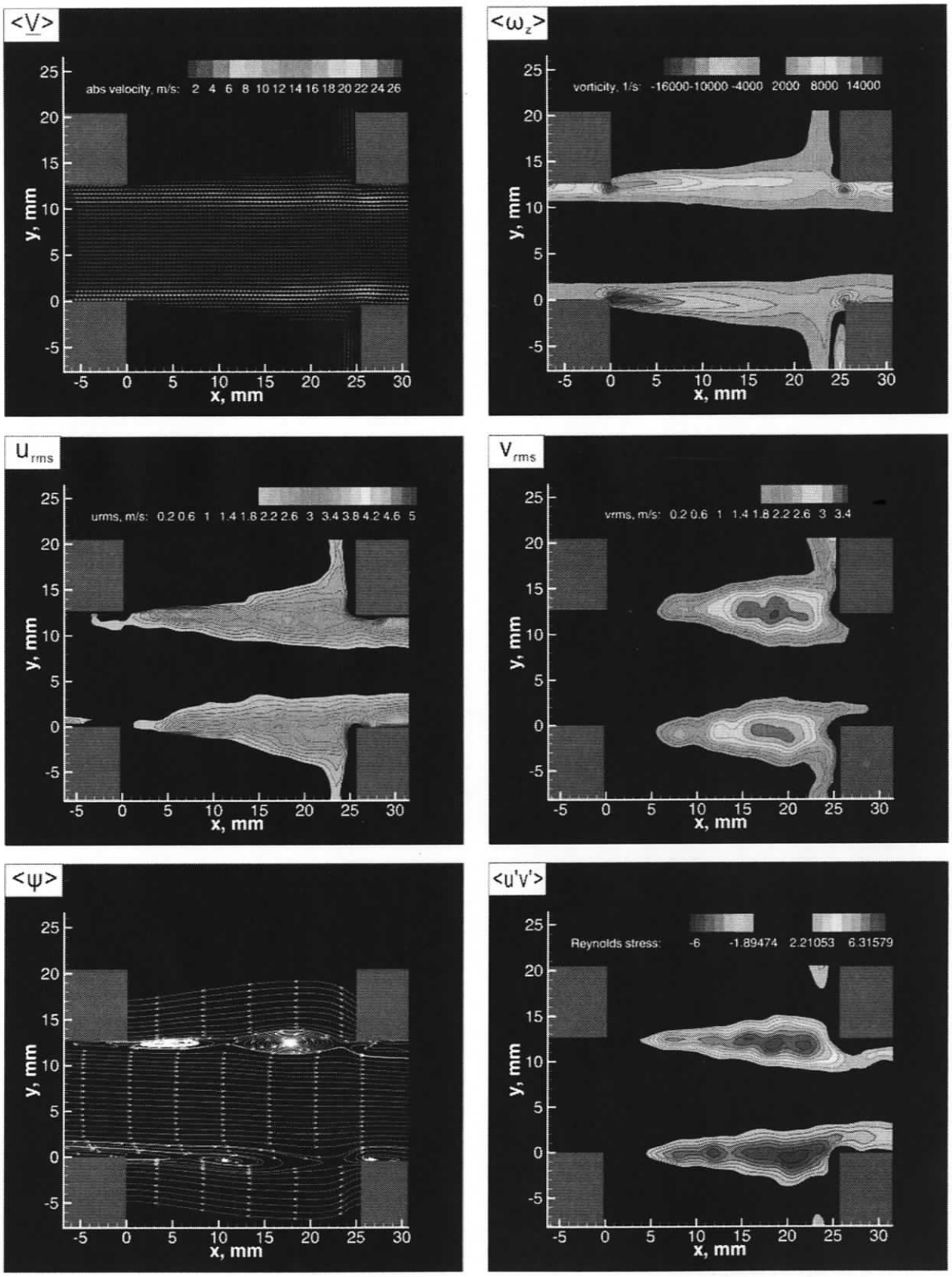

Figure 3.28: Time-averaged streamwise flow patterns corresponding to the second hydrodynamic oscillation mode for the case of the wide main duct (D/L = 0.5, Sr = 0.82, U_{ac}/U = 0.00017).

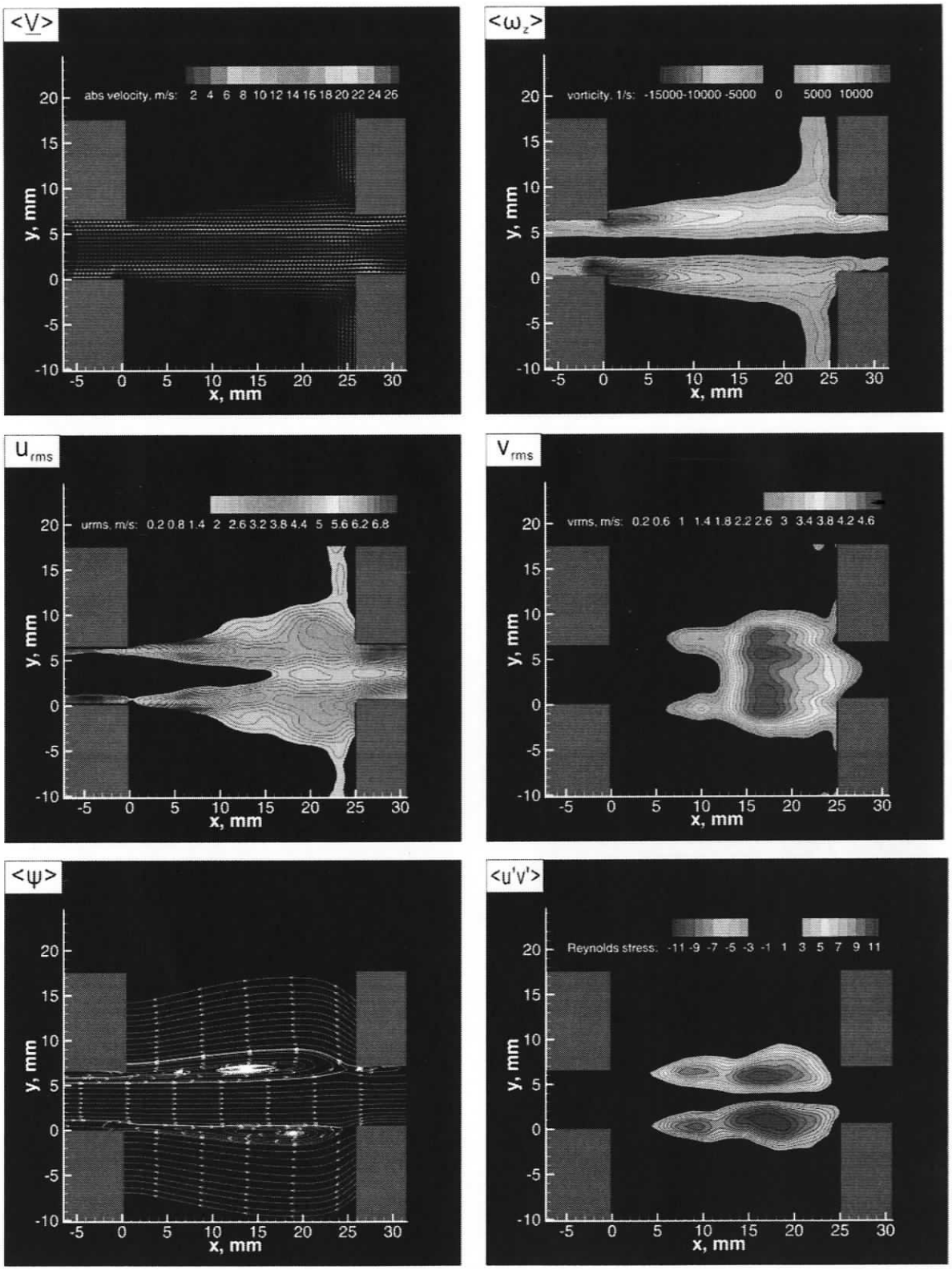

Figure 3.29: Time-averaged streamwise flow patterns corresponding to the second hydrodynamic oscillation mode for the case of the narrow main duct ($D/L = 0.25$, Sr = 0.76, $U_{ac}/U = 0.00036$).

3.5 Acoustic Power

The pressure fluctuations across the flow region which are induced by unsteady vortex shedding at the edges of the junction drive acoustic waves in pipes. This acoustic field can be described by using a one-dimensional wave approximation. The acoustic velocity u_{ac} is defined as the unsteady irrotational part of the velocity vector [5].

$$\underline{V} = \underline{\nabla}(\varphi_0 + \varphi_{ac}(t)) + \underline{\nabla} \times \underline{\psi}, \tag{24}$$

where $u_{ac} = \underline{\nabla}\varphi_{ac}(t)$ and $\underline{\nabla}\varphi_0$ is undisturbed mean flow. $\underline{\psi}$ is the vector stream function. The part $\underline{\nabla} \times \underline{\psi}$ represents the flow induced by vorticity. Howe [13] introduced Eqn. (25) to model the excitation mechanism of acoustically-coupled flow, in which vorticity is considered as a source of sound. The instantaneous acoustic power P generated by vorticity $\underline{\omega}$, within a volume V can be obtained from

$$P = \iiint_V -\rho_0 (\underline{\omega} \times \underline{V}) \cdot \underline{u_{ac}} dV, \tag{25}$$

where ρ_0 is the fluid density, $\underline{V}$ is the fluid velocity and $\underline{u_{ac}}$ is the acoustic particle velocity. The sign of the triple product $(\underline{\omega} \times \underline{V}) \cdot \underline{u_{ac}}$ determines whether vorticity acts as an acoustic source or sink. If the integral of instantaneous acoustic power over one acoustic cycle is positive, the acoustic resonance is self-sustained.

3.5.1 Acoustic power calculation

In order to simulate the one-dimensional fluctuating acoustic field in the side braches, the acoustic velocity $\underline{u_{ac}}$ is modeled numerically by a potential flow determined by the boundary conditions. A source-sink pair of variable strength m at the ends of the side branches is employed.

$$u_{ac} = m\left(\frac{1}{y-a} - \frac{1}{y+a}\right), \tag{26}$$

where a is the side branch depth measured from the centerline of the channel, as shown in Figure 3.30.

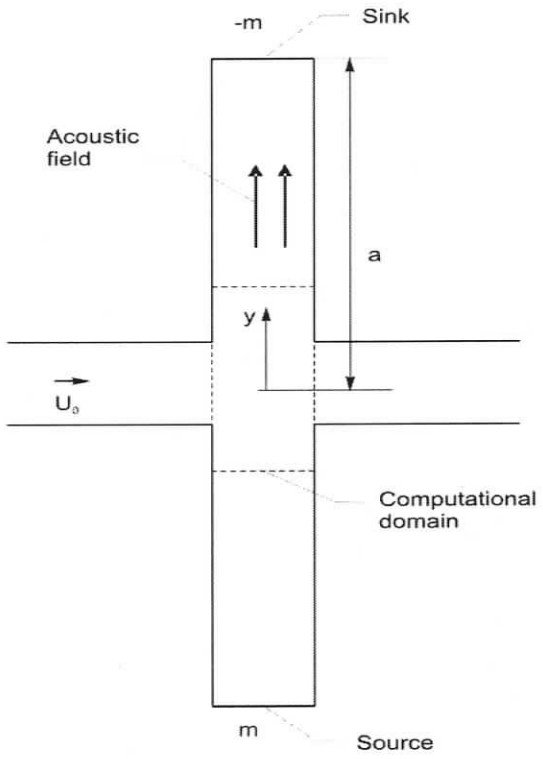

Figure 3.30: Definitions of parameters for acoustic power calculation.

The absolute value of source strength m equals to the magnitude of the acoustic velocity at the end walls that varies with time. The acoustic velocity signal at the end wall can be derived from the measured pressure signal.

$$p = P_{ac}\sin(2\pi ft), \tag{27}$$

where f is the frequency of the acoustic pressure signal measured at the end of a closed side branch. The acoustic velocity amplitude U_{ac} can be determined from the acoustic pressure amplitude P_{ac}.

$$U_{ac} = P_{ac} / \rho_0 c_0, \tag{28}$$

where ρ_0 is the mean fluid density and c_0 is the speed of sound. The phase shift between these two signals is $\frac{\pi}{2}$ according to the Bernoulli equation $P_0 = P + 1/2\ \rho_0 V^2$, where P_0 is the stagnation pressure. Therefore, the acoustic velocity at the end wall (source strength m) can be expressed as

$$m = (P_{ac} / \rho_0 c_0)\sin(2\pi ft + \frac{\pi}{2}), \tag{29}$$

Substituting this expression into Eqn. (26), the acoustic velocity inside the branch can be derived as follows:

$$u_{ac} = U_{ac}\sin(2\pi ft + \frac{\pi}{2}) * (\frac{1}{y-a} - \frac{1}{y+a}), \tag{30}$$

This method is based on the approximation that assumes that the friction and wall vibrations in the side branches are negligible.

The calculation of the acoustic power is based on the measured phase-averaged values of flow velocity and vorticity shown in Figures 3.18 – 3.23. The acoustic power can be determined by using Eqn. (25)

$$P = \iiint_V -\rho_0(\underline{\omega} \times \underline{V}) \cdot \underline{u_{ac}} dV$$

where

$$\underline{\omega} \times \underline{v} = \begin{vmatrix} i & j & k \\ 0 & 0 & \omega_z \\ u & v - u_{ac} & 0 \end{vmatrix} = u\omega_z \underline{j} - \omega_z (v - u_{ac})\underline{i}\ , \tag{31}$$

which leads to

$$(\underline{\omega} \times \underline{v}) \cdot \underline{u_{ac}} = \{u\omega_z \underline{j} - \omega_z (v - u_{ac})\underline{i}\} \cdot u_{ac}\underline{j} = u\omega_z u_{ac} \tag{32}$$

substituting Eqn. (32) into Eqn. (25) yields

$$P = -\rho_0 \iiint u\omega_z u_{ac} dV\ . \tag{33}$$

3.5.2 Phase-averaged acoustic power

3.5.2.1 Phase-averaged acoustic power at the first hydrodynamic oscillation mode

Figure 3.31 shows patterns of generated acoustic power for the wide (D/L = 0.5) and the narrow main duct (D/L = 0.25) in the left and right columns respectively. The three rows of images correspond to three successive phases of the acoustic oscillation cycle indicated by the location of the circle in the inset schematics in the middle of each row. The calculation of the acoustic power is based on the measured phase-averaged values of flow velocity and vorticity shown in Figures 3.18-3.23.

The first phase ($\varphi = 10^{\circ}$) corresponds to an instant when a new vortex starts to form at the upstream edge of upper side branch. The vortex absorbs energy from the acoustic field, resulting in the negative contribution to the acoustic power production, as indicated in the top row of images in Figure 3.31. At the same time, the well-developed vortical structure in the lower shear layer is convected downstream. The energy is transferred from the vortex to the acoustic field, which is indicated by the positive contours of the generated acoustic power across the mouth of the lower side branch.

The middle row of images corresponds to the phase $\varphi = 170^{\circ}$. Vortical structures in both upper and lower shear layers develop further, and the peak values of the generated acoustic power in the flow field increase. It should be noted that the vortices in the upper shear layer continue to absorb the energy from the acoustic field, since the acoustic velocity u_{ac} is still positive at this instant, i.e. it is directed into the upper side branch.

The bottom row of images corresponds to the phase $\varphi = 240^{\circ}$. At this phase, the acoustic velocity is directed into the lower side branch, and the vorticity in the upper shear layer makes a positive contribution to the generated acoustic power.

For all three phases, the case of the narrow main duct (D/L = 0.25) exhibits higher level of interaction between the upper and the lower shear layers, compared to the case of the wide duct (D/L = 0.5). As a result, the vortices within the shear layers attain higher levels of circulation, which in turn results in the increased peak values of acoustic power generation.

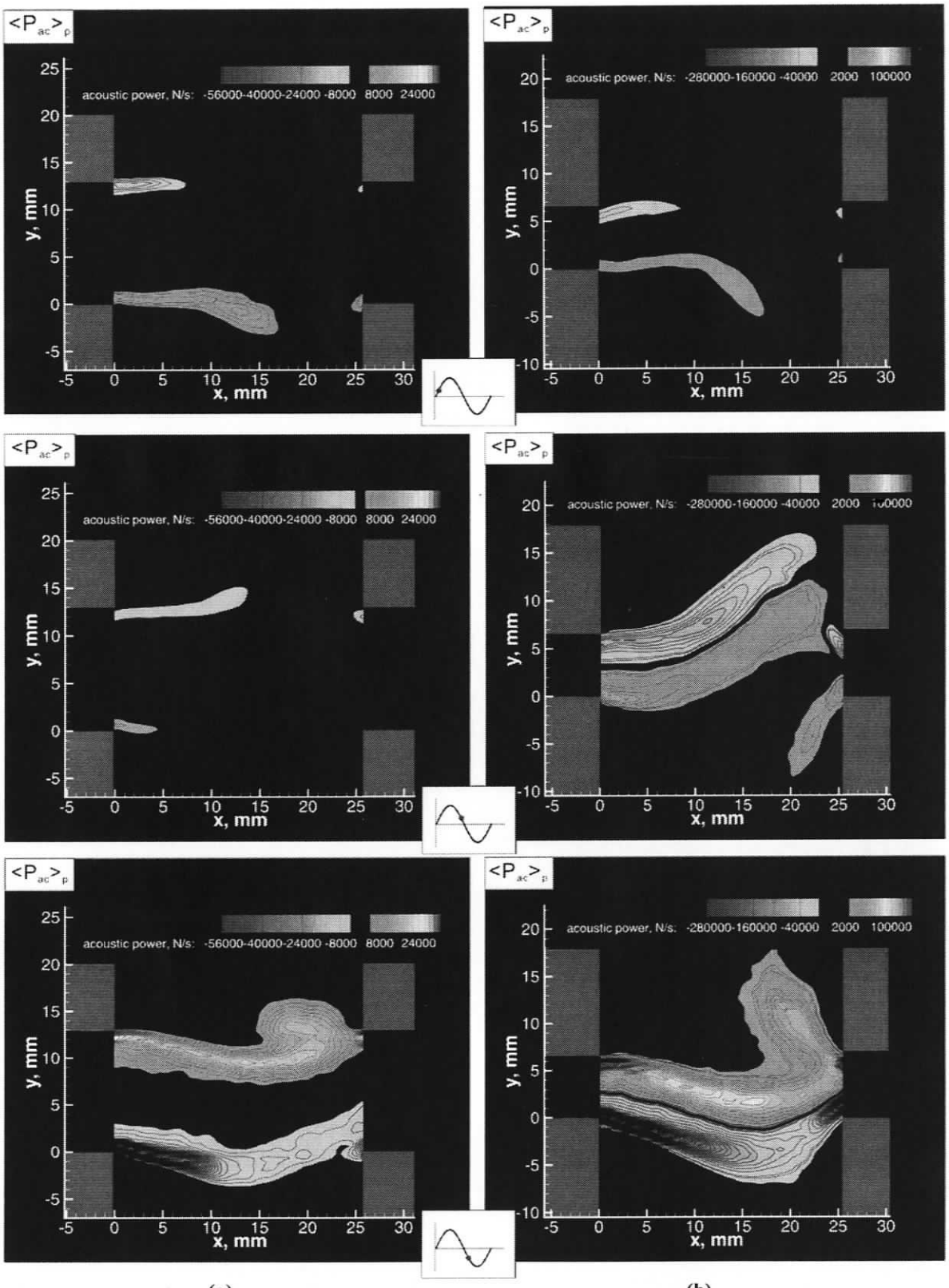

(a) **(b)**

Figure 3.31: Patterns of phase-averaged acoustic power corresponding to the first hydrodynamic oscillation mode at φ=10°, 170° and 240°. (a) Acoustic power for the case of the wide main duct (D/L=0.5, Sr=0.36, U_{ac}/U =0.0005); (b) acoustic power for the case of the narrow main duct (D/L=0.25, Sr=0.28, U_{ac}/U=0.001).

The acoustic power contribution of the upper shear layer as a function of time during a typical acoustic oscillation cycle is shown in Figure 3.32 for the case of the wide main duct (D = 12.7 mm). The first half of the period corresponds to the formation of large-scale vortical structures in the shear layers, while during the second half of the period, the vortices impinge on the downstream edge, and their energy is transferred to the acoustic field.

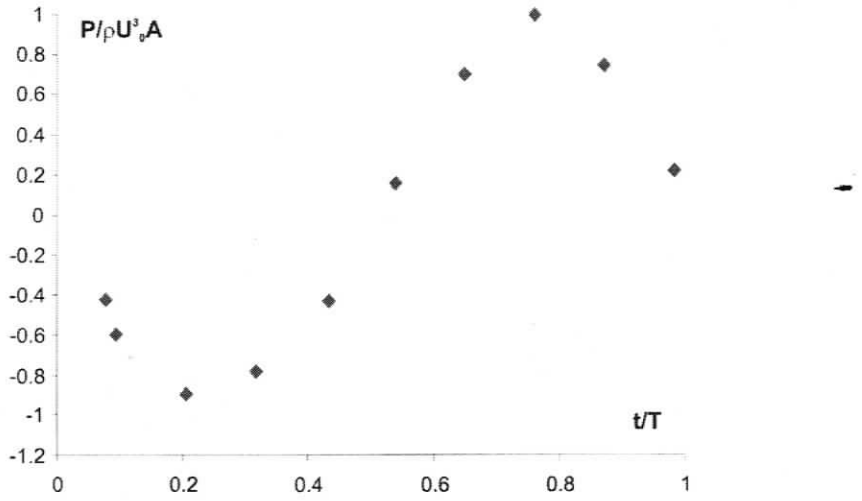

Figure 3.32: Acoustic power generated by the upper shear layer during one period of acoustic oscillation.

3.5.2.2 Phase-averaged acoustic power at the second hydrodynamic oscillation mode

For the second hydrodynamic oscillation mode, the phase-averaged powers at three phases for the wide (D/L = 0.5) and narrow main duct (D/L = 0.25) are shown in Figure 3.33. These three phases correspond to φ = 10°, 160° and 250°. In the case of the wide main duct, at phase φ = 10°, the source region with the peak amplitude of approximately 320 N/s spans over the mouth of the lower side branch. The highest power source region is located near the upstream corner of the junction between the main duct and lower side branch. The weaker sink dominates the larger area of the upper side branch opening. It extended further downstream. The acoustic velocity at this time is directed into the upper

side branch. The sign of the triple product $(\underline{\omega} \times \underline{V}) \cdot \underline{u_{ac}}$ corresponding to the top shear layer is negative, which means that the vorticities act as acoustic sinks. In the lower region of junction, the opposite sign of triple product results in the positive contribution of the lower shear layer.

At the phase of φ = 160°, the power levels become significantly higher as a result of developed large-scale vorticies that exhibit higher circulation levels. Since the acoustic velocity field did not change direction compared to the previous phase (φ = 10°), the upper and lower shear layers still correspond to negative and positive contributions to acoustic power respectively

At the phase φ = 250°, the acoustic velocity is directed into the lower side branch. The triple product changes the sign, which leads to the positive contribution from the upper shear layer and to formation of a sink region at the lower side. As can be seen in Figure 3.23, elevated levels of vorticity occur over a large area in the flow field. As a result, the peak values of the generated acoustic power are increased.

Comparing the plots at different times in the acoustic cycle, the acoustic source is produced as the acoustic velocity points out of the side branch; while an acoustic sink is produced as the acoustic velocity pulls back into the side branch

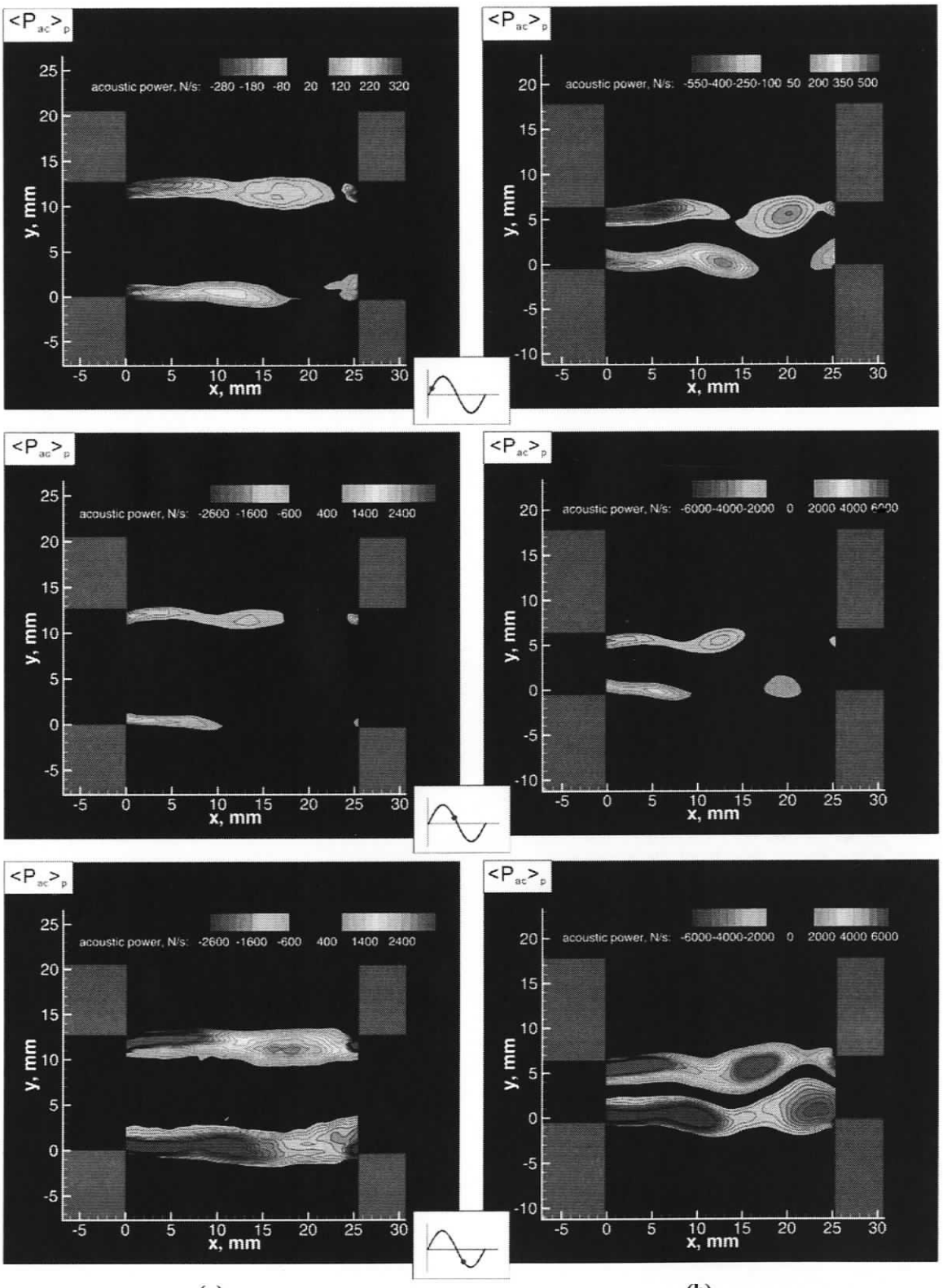

(a) **(b)**

Figure 3.33: Patterns of phase-averaged acoustic power corresponding to the second hydrodynamic oscillation mode at φ=10°, 160° and 250°. (a) Acoustic power for the case of the wide main duct (D/L = 0.5, Sr = 0.82, U_{ac}/U = 0.00017); (b) acoustic power for the case of the narrow main duct (D/L = 0.25, Sr = 0.76, U_{ac}/U = 0.00036).

3.5.3 Time-averaged acoustic power

3.5.3.1 Time-averaged acoustic power at the first hydrodynamic oscillation mode

Patterns of the time-averaged acoustic power are shown in Figure 3.34. The left and right plots correspond to the wide and the narrow main ducts respectively.

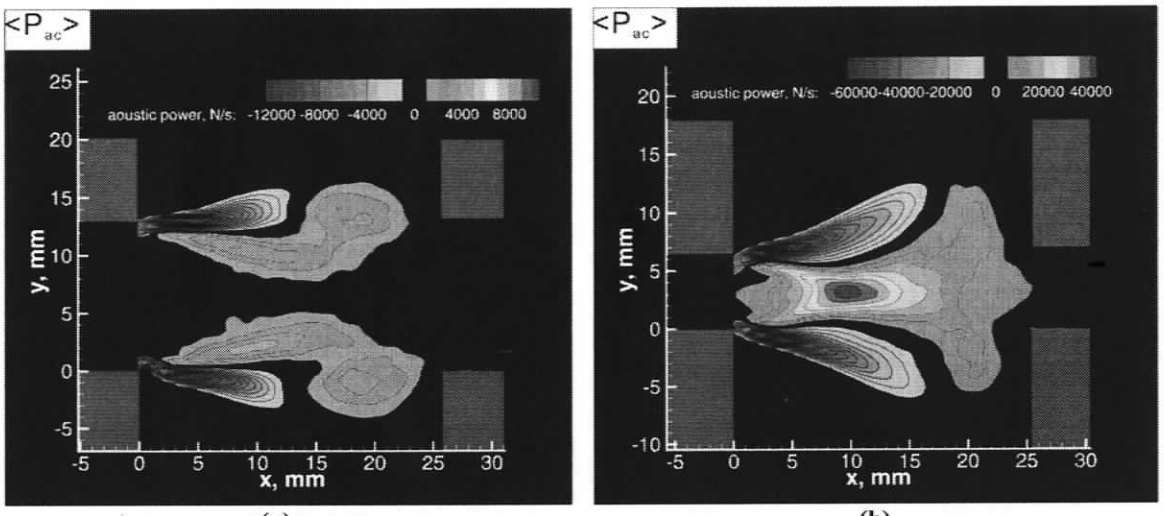

(a) (b)

Figure 3.34: Patterns of time-averaged acoustic power corresponding to the first hydrodynamic oscillation mode. (a) Acoustic power for the case of the wide main duct (D/L = 0.5, Sr = 0.36, U_{ac}/U = 0.0005); (b) acoustic power for the case of the narrow main duct (D/L = 0.25, Sr = 0.28, U_{ac}/U = 0.001).

In the case of the wide duct (D/L = 0.5), the upper and the lower shear layers develop, essentially, independently of each other. As a result, the structure of the acoustic power producing region exhibits two distinct source-sink pairs. The sinks correspond to the regions where the acoustic energy is absorbed by the flow field. These areas are indicated by the negative contours. The sources are located farther downstream in each of the shear layers, where the large-scale vortices start to interact with the impinging corners of the side branches.

When the main duct width is reduced, the increased interaction between the shear layers results in formation of a single acoustic power source region, as shown in the right plot of Figure 3.34. The source is accompanied by two sinks that correspond to the regions

in the shear layers where vortex development takes place. It should be noted that the source region extends across the entire opening of the coaxial side branch resonator.

3.5.3.2 Time-averaged acoustic power at the second hydrodynamic oscillation mode

The approximate acoustic power produced over an acoustic cycle at the second hydrodynamic oscillation mode is shown in Figure 3.35.

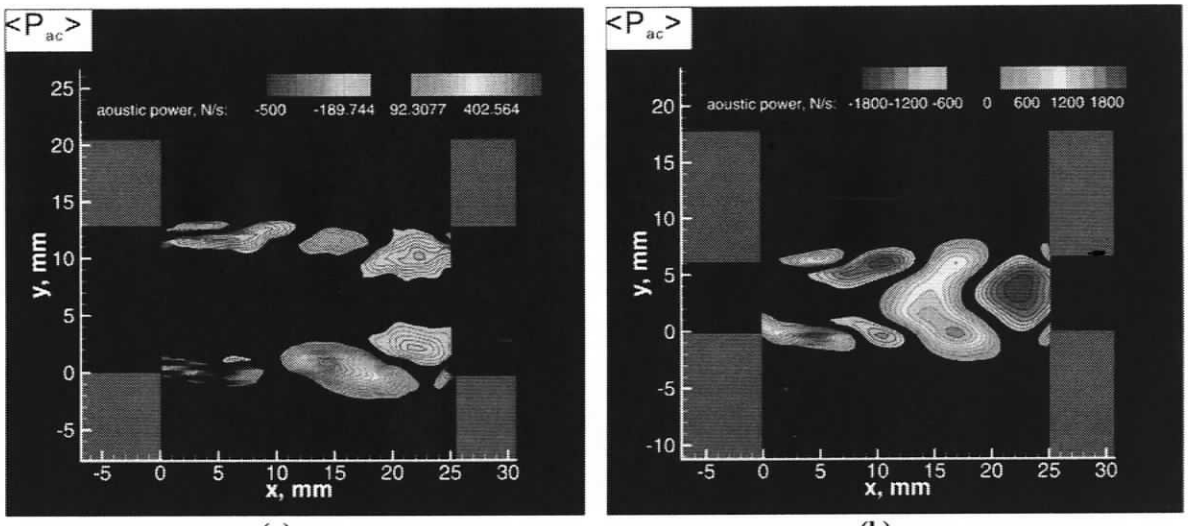

Figure 3.35: Patterns of time-averaged acoustic power corresponding to the second hydrodynamic oscillation mode. (a) Acoustic power for the case of the wide main (D/L = 0.5, Sr = 0.82, U_{ac}/U = 0.00017); (b) acoustic power for the case of the narrow main duct (D/L = 0.25, Sr = 0.76, U_{ac}/U = 0.00036).

The plot (a) shows the time-averaged acoustic power distribution for the case of the wide main duct. A more complex acoustic power structure is observed in comparison to that of the first hydrodynamic mode. The peak amplitude of acoustic power is significantly lower than the values observed in Figure 3.34. A typical vortex traverses the mouth of the side branch in two periods of acoustic velocity oscillation. During this travel, the vortex provides two positive and two negative contributions to acoustic power. Since there is no significant interaction between the upper and lower shear layers, four discrete pairs of sink and source regions exist over the junction area.

The spatial distribution of the generated acoustic power is substantially different in the case of the narrow main duct (shown in the plot on the right). While the interaction between the two shear layers is still limited immediately after the separation, two discrete source-sink pairs exist in the vicinity of the upstream corner of the junction. The two source regions with peak amplitudes of 1800 N/s are located at x = 4 mm. Farther downstream, where the vortices in the upper and lower shear layers interact with each other, a large single source region is present. This source region exhibits high levels of generated acoustic power due to increased circulation of the large-scale vortices. Prior to impingement on the downstream side branch corner, the two interacting shear layers produce a single large-scale sink region that is located at x =22 mm.

CHAPTER 4

CONCLUSIONS AND RECOMMENDATIONS

Global quantitative images of acoustically-coupled flows through coaxial side branch resonators were obtained using digital particle image velocimetry (DPIV). Combination of the DPIV imaging with measurements of unsteady acoustic pressure allowed characterization of the flows in terms of instantaneous, phase- and time-averaged parameters, including velocity vector fields, out-of-plane vorticity contours, streamlines, and turbulence statistics.

Implementation of phase-locking techniques provides visualization of the formation and propagation of vorticies during a single acoustic cycle. The theory of Howe [13] is applied to study acoustic power generation, which is related to the interaction between the vorticity, the hydrodynamic velocity, and the acoustic velocity field. The velocity and vorticity values that were used in the acoustic power calculation are based on the DPIV measurements. The acoustic velocity field is modeled numerically using potential flow theory. The method of acoustic power calculation combined with the phase-locking techniques provides insight into the mechanisms of acoustic power generation during a typical cycle of acoustic oscillations. In general, it was observed that the acoustic source is produced in the junction region of the coaxial resonator as the acoustic velocity pushes out of the side branch, while an acoustic sink is produced as the acoustic velocity pulls back into the side branch.

Strong acoustic resonances of the third and fifth acoustic modes of the resonator were observed over two ranges of mean flow velocity, which is associated with two ranges of

Strouhal number Sr. The Strouhal number of the largest acoustic pulsation (the third acoustic mode) does not exceed 0.42. This range of Strouhal number correspond to the first hydrodynamic shear layer oscillation mode. The fifth acoustic mode excited by the second hydrodynamic mode, which results in a resonance range of Sr = 0.53 to 0.82. The present study addresses the two different diameter ratios (D/L = 0.25 and 0.5.) The main results of these tests can be summarized as follows:

1) The ratio between the cavity width and the main pipe width is crucial in determining the acoustic pressure amplitude. The decreased ratio results in the substantial amplification of the acoustic oscillation amplitude. It is expected that the pressure amplitude depends nonlinearly on the diameter ratio (D/L) because of the non-linear character of the turbulent shear layer interactions.

2) The Strouhal mode of the flow-acoustic resonance has effect on the pressure amplitude. The acoustic resonance achieved during the lower Strouhal mode is stronger than the higher Strouhal number resonance. The acoustic pulsation amplitude is highest for the first hydrodynamic oscillation mode.

3) The decrease of the main duct width has a pronounced effect on the acoustic power source structure due to increased interaction between the unsteady shear layers that form across the side branch openings. At the first shear layer oscillation mode, the spatial structure of the acoustic power producing region changes from two independent sources to a single source as the main duct width decreases. At the second hydrodynamic oscillation mode which is associated with the formation of two vortices in the shear layer, the structure of acoustic power changes from two typical power regions to four. Two distinct source-sink pairs at the downstream region change to a single source and a single sink region when

the main duct width is decreased.

The results obtained through the experiments provide the basis for general engineering applications. The strong acoustic resonances can be attenuated by keeping the diameter ratio *(D/L)* larger than 0.5. For smaller diameter ratio (D/L <0.5), the strong acoustic resonance can be avoided by keeping the Strouhal number sufficiently high (Ziada [5]).The safe range of Strouhal numbers can be achieved by carefully adjusting the flow velocity. Regarding the geometric variations, Kriesels *et al.* [6] reported that the experimental data for square and circular pipes do not differ significantly at moderate acoustic amplitudes. Therefore, at low acoustic amplitudes, the present experimental data is applicable to circular pipe system.

In addition to systematically addressing the mechanisms of acoustic power generation in coaxial side branch resonators, the present study provides a background for the future investigations. The method used herein to calculate the acoustic velocity U_{ac} assumes that there is a perfect standing wave in the side branches. It neglects the friction and wall vibration effects. The acoustic wave front in the computational domain is perfectly one-dimensional. These are the crude assumptions. In the corner of the junction, the acoustic wave front is expected to be distorted due to the acoustic flux into the main duct. The assumption of one-dimensional acoustic waves at the inlet and outlet regions of the main duct is not valid in general. A more accurate method of modeling of the acoustic field that is based on numerical solution of a two-dimensional non-homogeneous wave equation is going to be implemented in the future in conjunction with the experimental results of the present study.

BIBLIOGRAPHY

[1] Adela B. and Ronald, K.H., Cavity flameholders for ignition and flame stabilization in scramjets: review and experimental study. High Temperature Gasdynamics Laboratory, Stanford University, California

[2] Rockwell, D., Naudascher, E. 1979 Self-sustained oscillations of impinging free shear layers. *Annual Reviews of Fluid Mechanics* 11, 67-94

[3] Rockwell, D., Lin, J.C., Oshkai, P., Reiss, M., and Pollack, M. 2003 Shallow cavity flow tone experiments: onset of locked-on states. *Journal of Fluids and Structures* 17(3), 381-414.

[4] Blake, W.K., 1986 Mechanics of Flow-Induced Sound and Vibration, Vols. 1. Academic Press, New York.

[5] Ziada, S., Buehlmann, E. T. 1992 Self-excited resonances of two side-branches in close proximity. *Journal of Fluids and Structures* 6,583-161

[6] Kriesels, P.C., Peters, M.C.A.M., Hirschberg, A.,and Wijnands, A.P.J. 1995 High amplitude vortex-induced pulsations in a gas transport system. *Journal of Sound and Vibration* 184(2), 343-368

[7] Oshkai, P., Geveci, M., Rockwell, D., and Pollack M. 2005 Imaging of Acoustically Coupled Oscillations due to Flow Past a Shallow Cavity: Effect of Cavity Length Scale. *Journal of Fluids and Structures* 20(2), 277-308.

[8] Geveci, M., Oshkai, P., Rockwell, D., Lin, J.-C. and Pollack, M. 2003 Imaging of the self-excited oscillation of flow past a cavity during generation of a flow tone. *Journal of Fluids and Structures* 18, 665-694

[9] Dequand, S., Hulshoff, S.J., Hirschberg, A. 2003 Self-sustained oscillations in a closed side branch system. *Journal of Sound and Vibration* 265, 259-386

[10] Ziada, S., 1994 A flow visualization study of flow-acoustic coupling at the mouth of a resonant side-branch. *Journal of Fluids and Structures* 8, 391-416

[11] Nelson, P.A., Halliwell, N.A.Doak, P.E. 1981 Fluid dynamics of a flow excited resonance. Part I: Experiment. *Journal of Sound and Vibration* 78, 15-38.

[12] Jungowski, W.M., Botros, K.K. and Studzinski, W. 1989 Cylindrical side-branch as tone generator. *Journal of Sound and Vibration* 131, 265-285.

[13] Howe, M.S. 1975 Contributions to the theory of aerodynamic sound, with application to excess jet noise and the theory of the flute. *Journal of Fluid Mechanics* 71, 625-673

[14] Alistair H. 2004 Mech 499 final report. University of Victoria, Victoria, Canada

[15] 2001 *NI 4472 User Manual.* USA: National Instruments,

[16] Adrian, R.J. 1991 Particle-imaging techniques for experimental fluid mechanics. *Annual Review of Fluid Mechanics* 23, 261-304

[17] Maeda T.,Onishi, N., Kadooka, Y. and Tago, Y. 2004 Development of PIV web laboratory and its application, *FUJITSU Sci. Tech. J.* 40(2), 232-241

[18] Huang H., Dabiri D., Gharib M. 1997 On errors of digital particle image velocimetry. *Meas. Sci. Technol.* 8, 1427-1440

[19] Willert, C.E., Gharib M. 1991 Digital particle image velocimetry. *Experiments in Fluids* 10, 181-193

[20] Ziada, S. 2001 Interaction of a jet-slot oscillator with a deep cavity resonator and its control. *Journal of Fluids and Structures* 15, 831-843

[21] Ziada, S., Ng, H., Blake, C.E. 2003 Flow excited resonance of a confined shallow cavity in low Mach number flow and its control. McMaster University, Hamilton, Ontario, Canada

APPENDIX A: PHASE-AVERAGED FLOW PATTERNS AT THE FIRST HYDRODYNAMIC OSCILLATION MODE

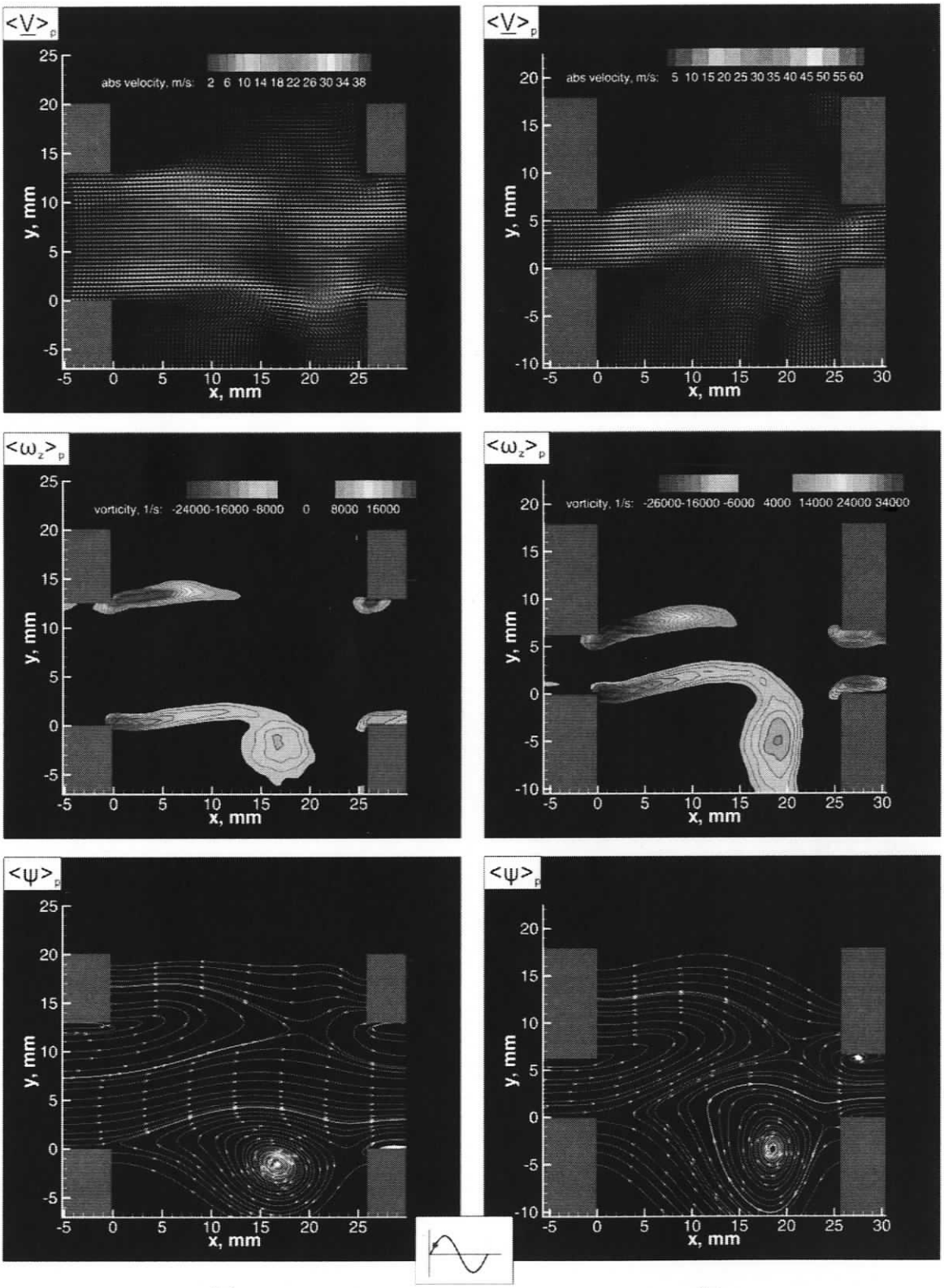

(a) **(b)**

Figure A.1: Phase-averaged streamwise flow patterns corresponding to the first hydrodynamic oscillation mode at φ=50°. (a) Flow patterns for the case of the wide main duct (D/L=0.5, S=0.36, U_{ac}/U=0.0005); (b) flow patterns for the case of the narrow main duct (D/L=0.25, S=0.28, U_{ac}/U=0.001).

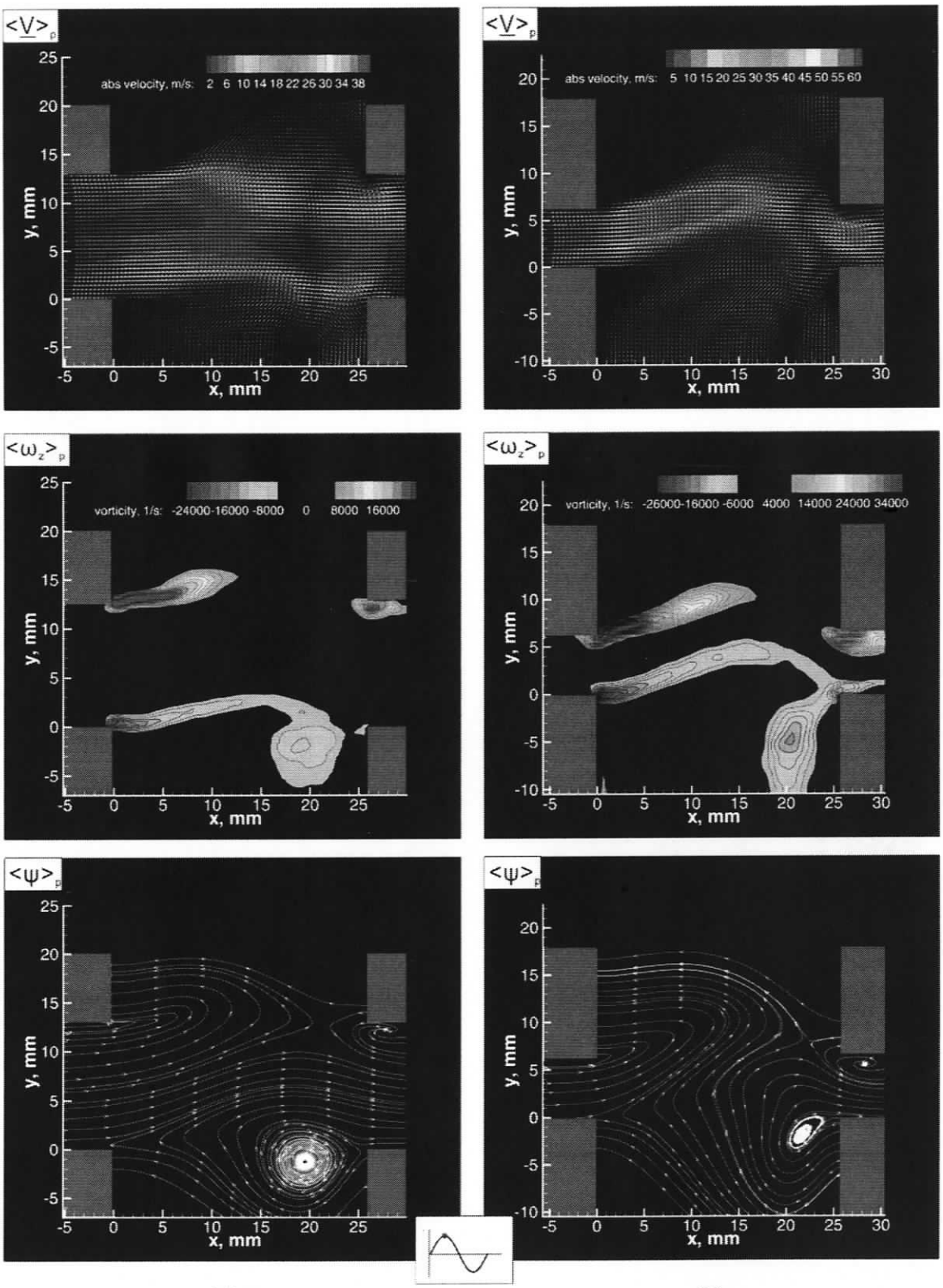

(a) **(b)**

Figure A.2: Phase-averaged streamwise flow patterns corresponding to the first hydrodynamic oscillation mode at φ=90°. (a) Flow patterns for the case of the wide main duct (D/L=0.5, S=0.36, U_{ac}/U=0.0005); (b) flow patterns for the case of the narrow main duct (D/L=0.25, S=0.28, U_{ac}/U=0.001).

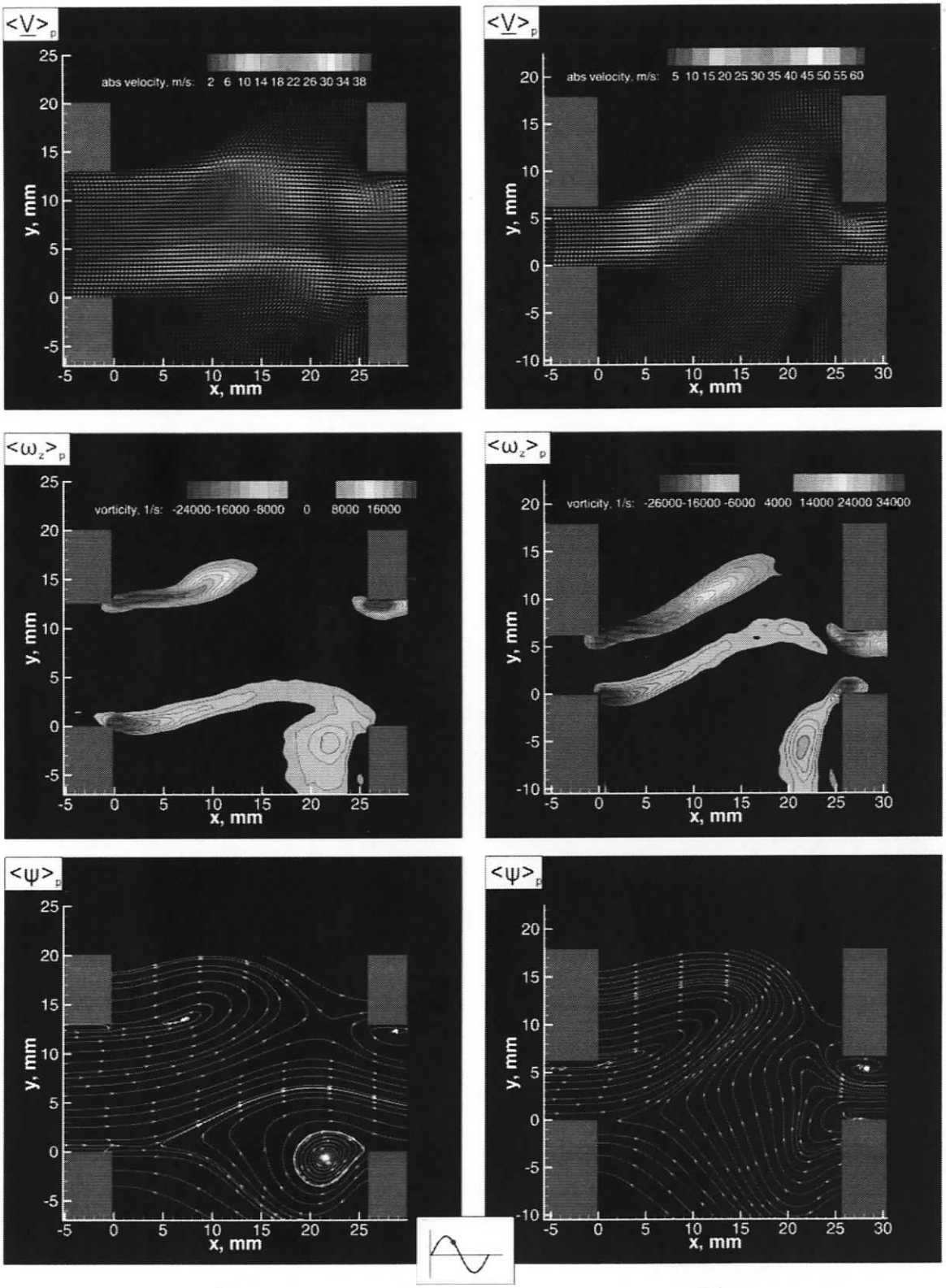

(a) **(b)**

Figure A.3: Phase-averaged streamwise flow patterns corresponding to the first hydrodynamic oscillation mode at φ=130°. (a) Flow patterns for the case of the wide main duct (D/L=0.5, S=0.36, U_{ac}/U=0.0005); (b) flow patterns for the case of the narrow main duct (D/L=0.25, S=0.28, U_{ac}/U=0.001).

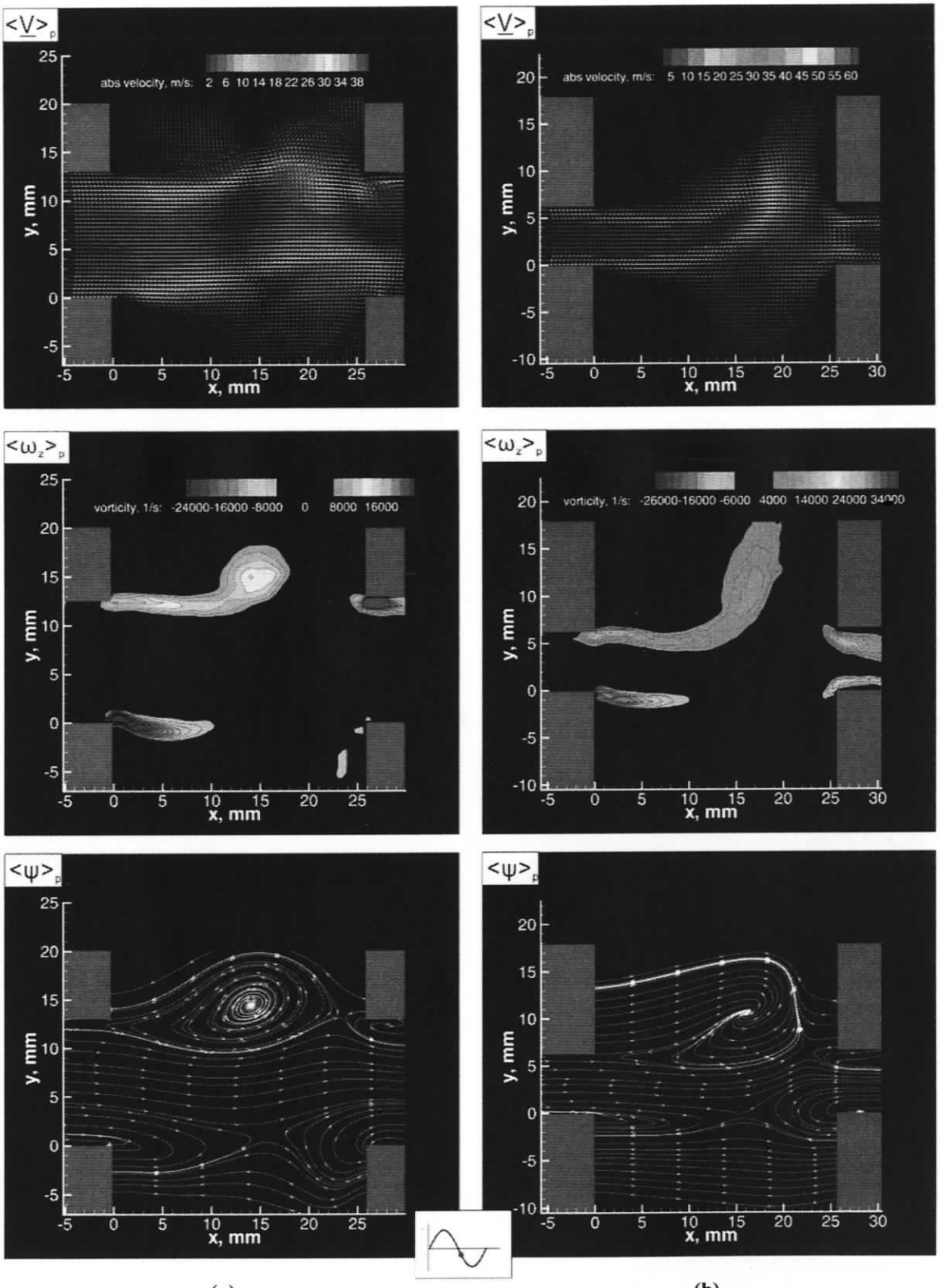

(a) **(b)**

Figure A.4: Phase-averaged streamwise flow patterns corresponding to the first hydrodynamic oscillation mode at φ=210°. (a) Flow patterns for the case of the wide main duct (D/L=0.5, S=0.36, U_{ac}/U=0.0005); (b) flow patterns for the case of the narrow main duct (D/L=0.25, S=0.28, U_{ac}/U=0.001).

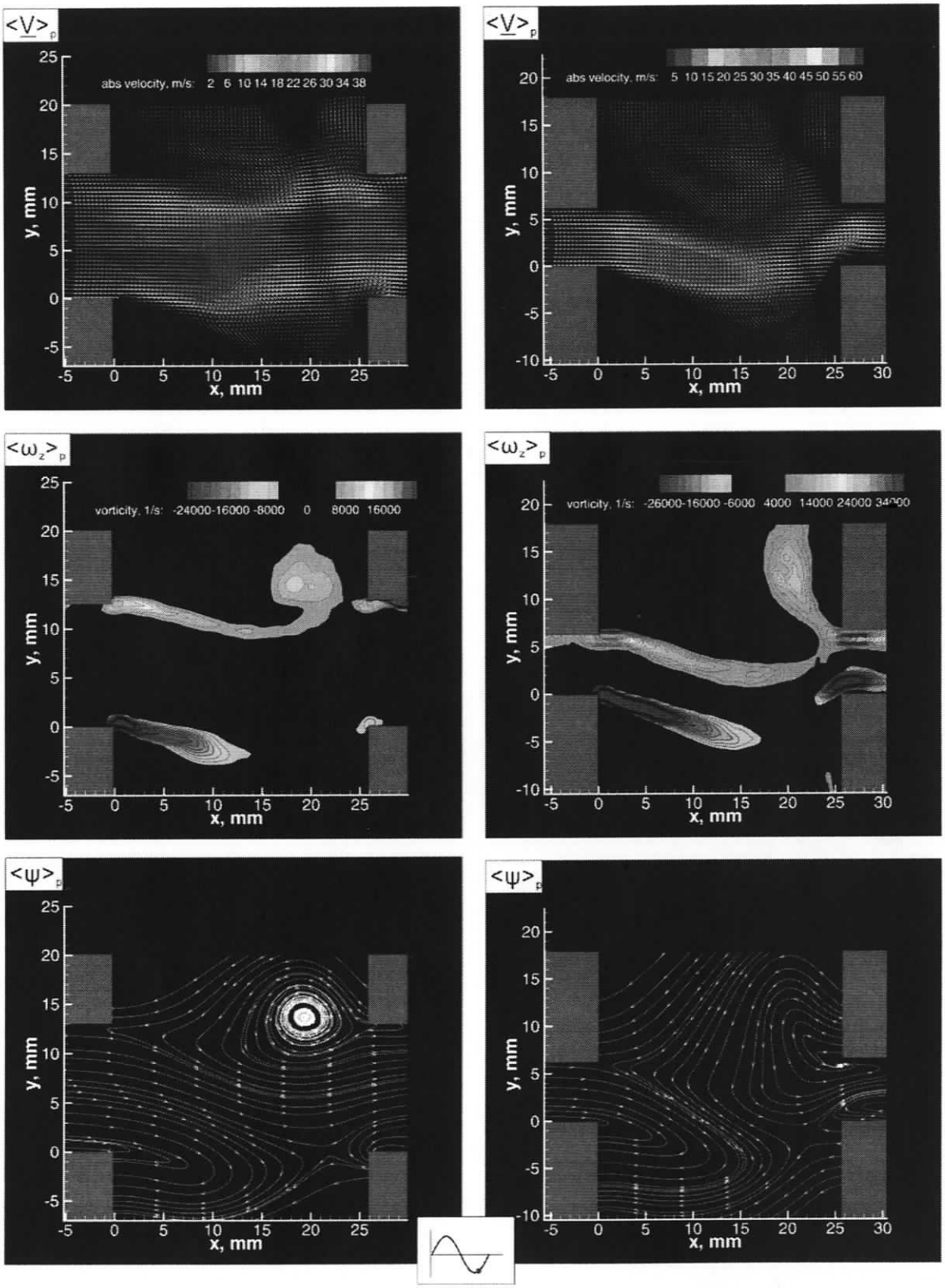

(a) **(b)**

Figure A.5: Phase-averaged streamwise flow patterns corresponding to the first hydrodynamic oscillation mode at φ=290°. (a) Flow patterns for the case of the wide main duct (D/L=0.5, S=0.36, U_{ac}/U=0.0005); (b) flow patterns for the case of the narrow main duct (D/L=0.25, S=0.28, U_{ac}/U=0.001).

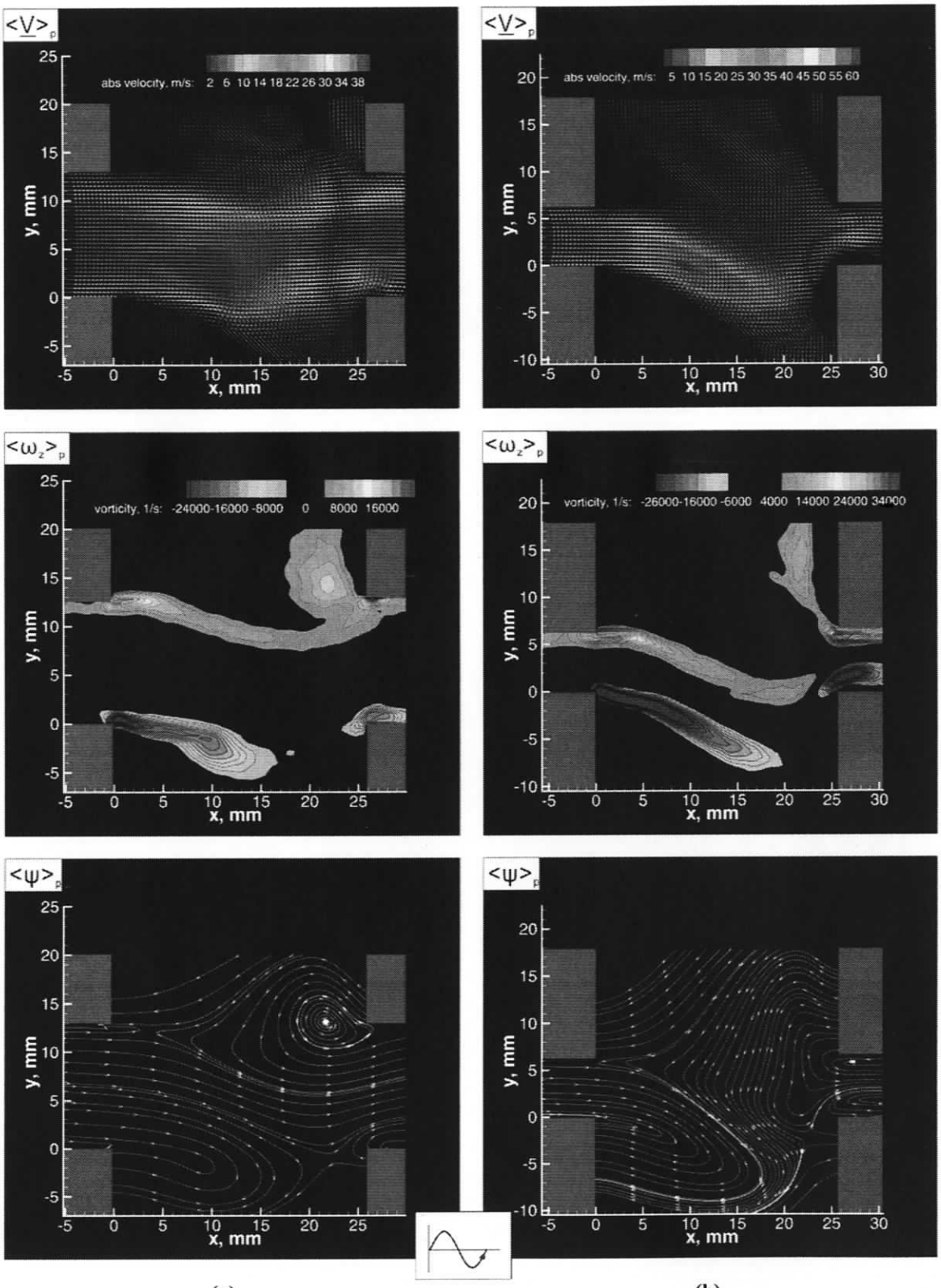

(a) **(b)**

Figure A.6: Phase-averaged streamwise flow patterns corresponding to the first hydrodynamic oscillation mode at φ=330°. (a) Flow patterns for the case of the wide main duct (D/L=0.5, S=0.36, U_{ac}/U=0.0005); (b) flow patterns for the case of the narrow main duct (D/L=0.25, S=0.28, U_{ac}/U=0.001).

APPENDIX B: PHASE-AVERAGED FLOW PATTERNS AT THE SECOND HYDRODYNAMIC OSCILLATION MODE

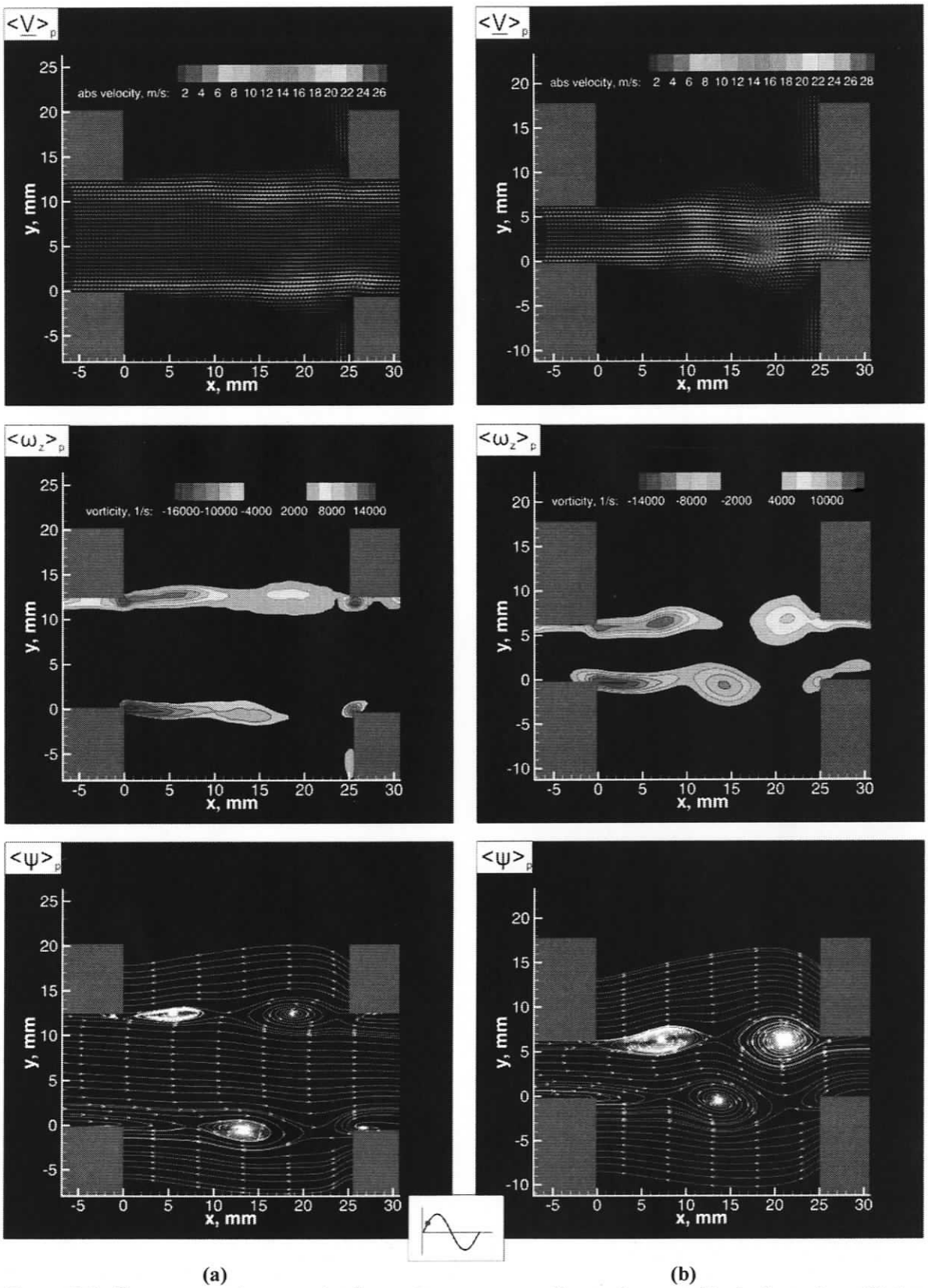

(a) **(b)**

Figure B.1: Phase-averaged streamwise flow patterns corresponding to the second hydrodynamic oscillation mode at φ=40°. (a) Flow patterns for the case of the wide main duct (D/L=0.5, Sr=0.82, U_{ac}/U=0.00017); (b) flow patterns for the case of the narrow main duct (D/L=0.25, Sr=0.76, U_{ac}/U=0.00036).

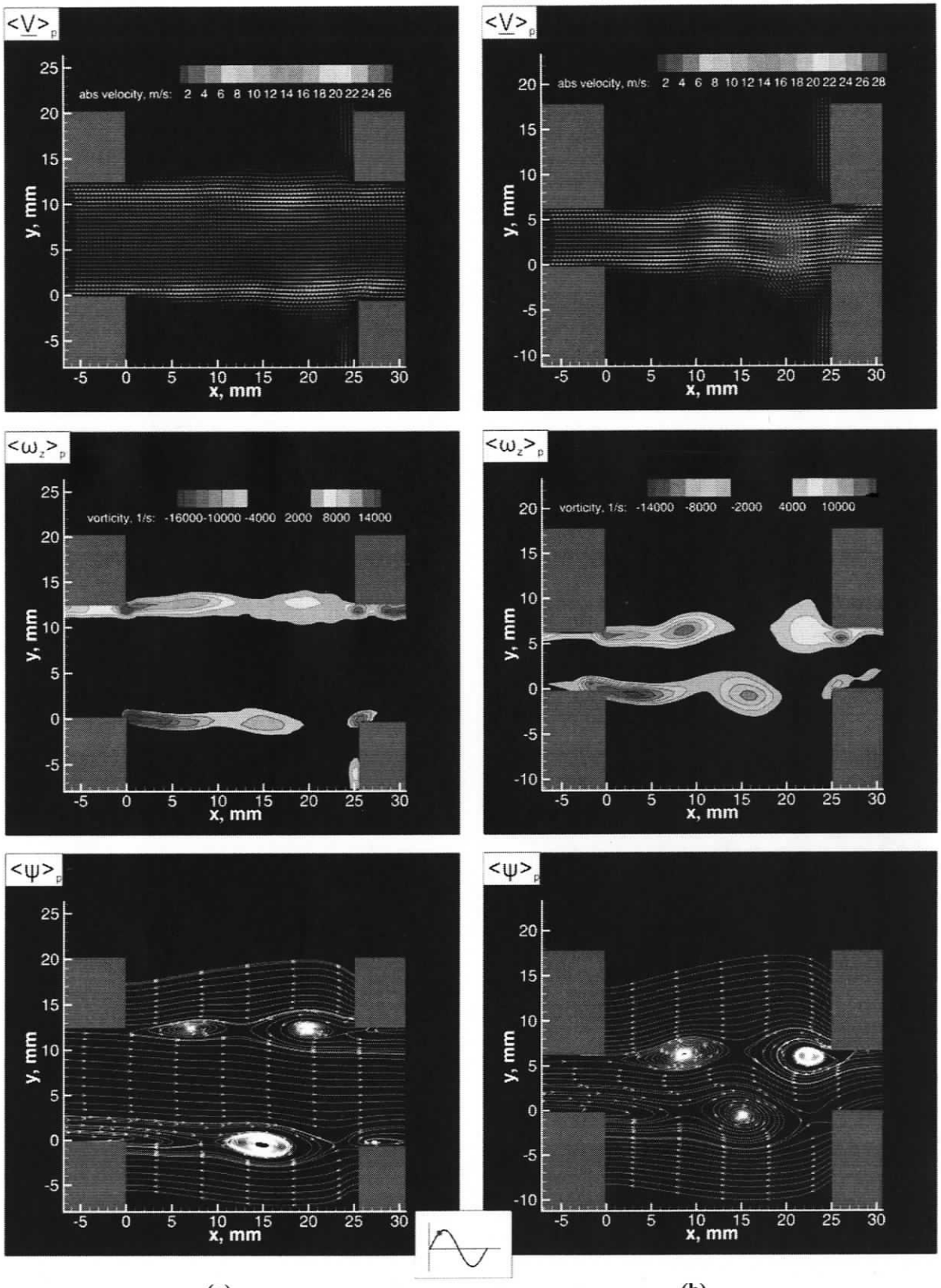

(a) **(b)**

Figure B.2: Phase-averaged streamwise flow patterns corresponding to the second hydrodynamic oscillation mode at φ=70°. (a) Flow patterns for the case of the wide main duct (D/L=0.5, Sr=0.82, U_{ac}/U=0.00017); (b) flow patterns for the case of the narrow main duct (D/L=0.25, Sr=0.76, U_{ac}/U=0.00036).

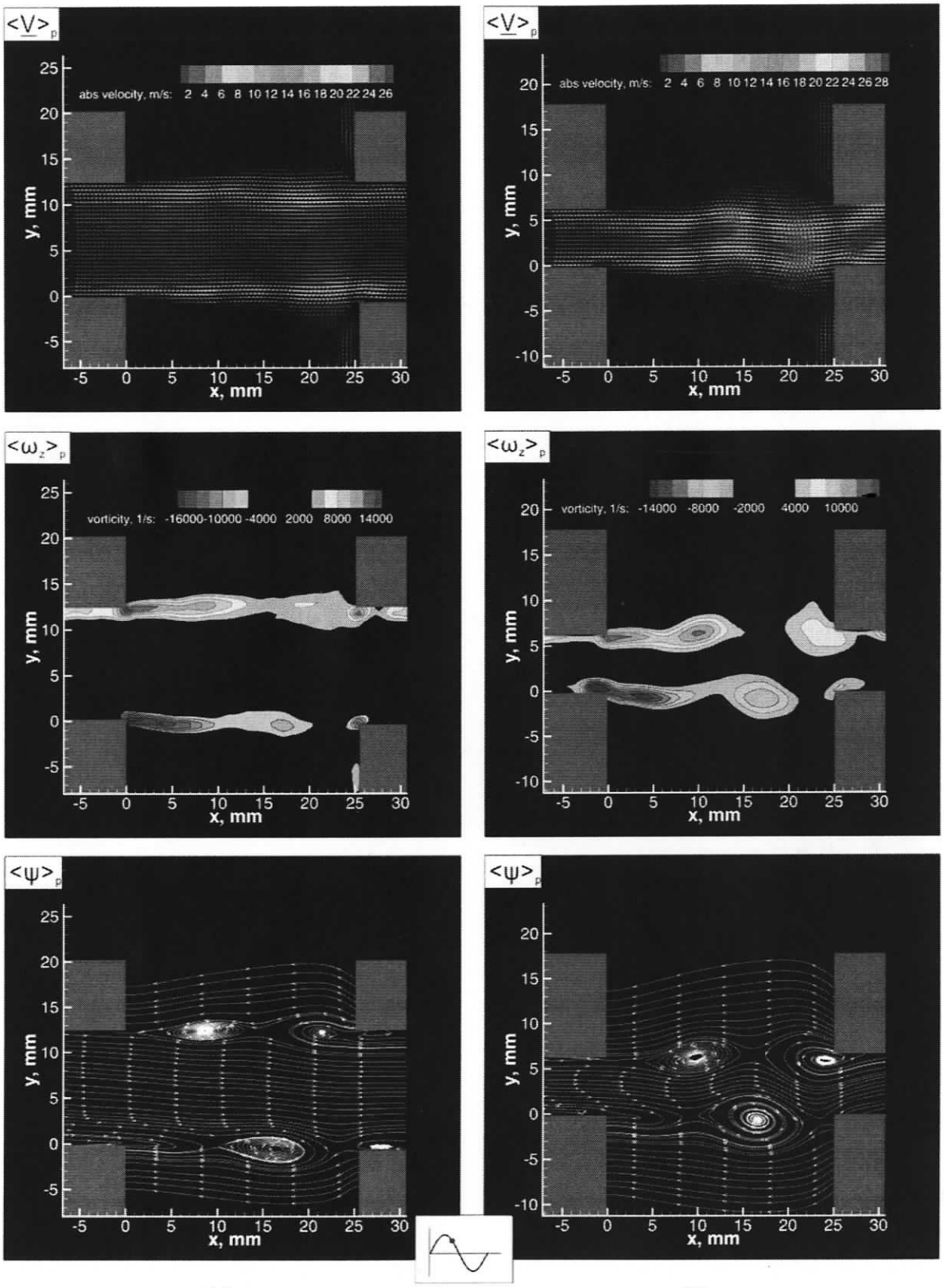

(a) (b)

Figure B.3: Phase-averaged streamwise flow patterns corresponding to the second hydrodynamic oscillation mode at φ=100°. (a) Flow patterns for the case of the wide main duct (D/L=0.5, Sr=0.82, U_{ac}/U=0.00017); (b) flow patterns for the case of the narrow main duct (D/L=0.25, Sr=0.76, U_{ac}/U=0.00036).

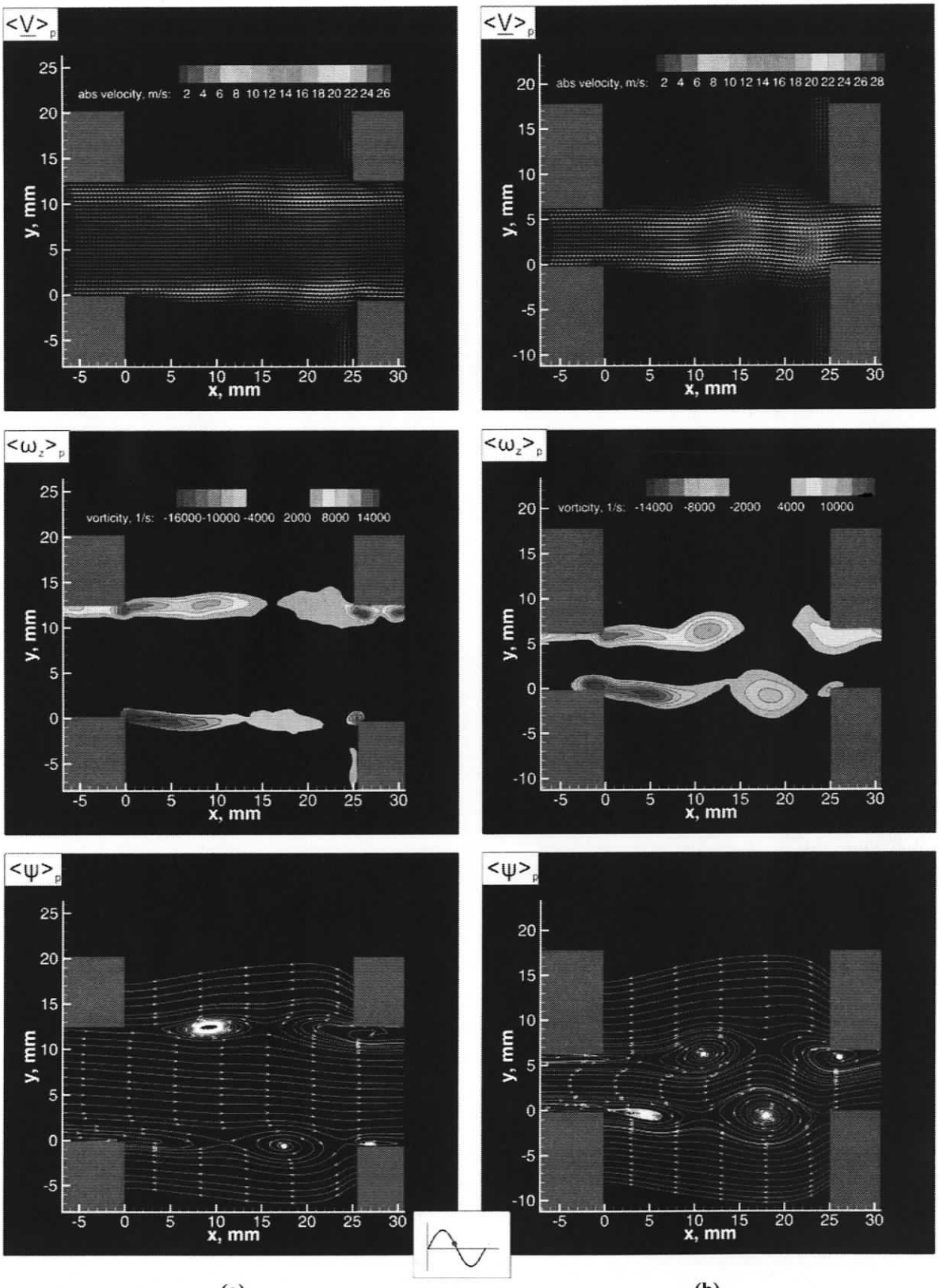

(a) **(b)**

Figure B.4: Phase-averaged streamwise flow patterns corresponding to the second hydrodynamic oscillation mode at φ=130°. (a) Flow patterns for the case of the wide main duct (D/L=0.5, Sr=0.82, U_{ac}/U=0.00017); (b) flow patterns for the case of the narrow main duct (D/L=0.25, Sr=0.76, U_{ac}/U=0.00036).

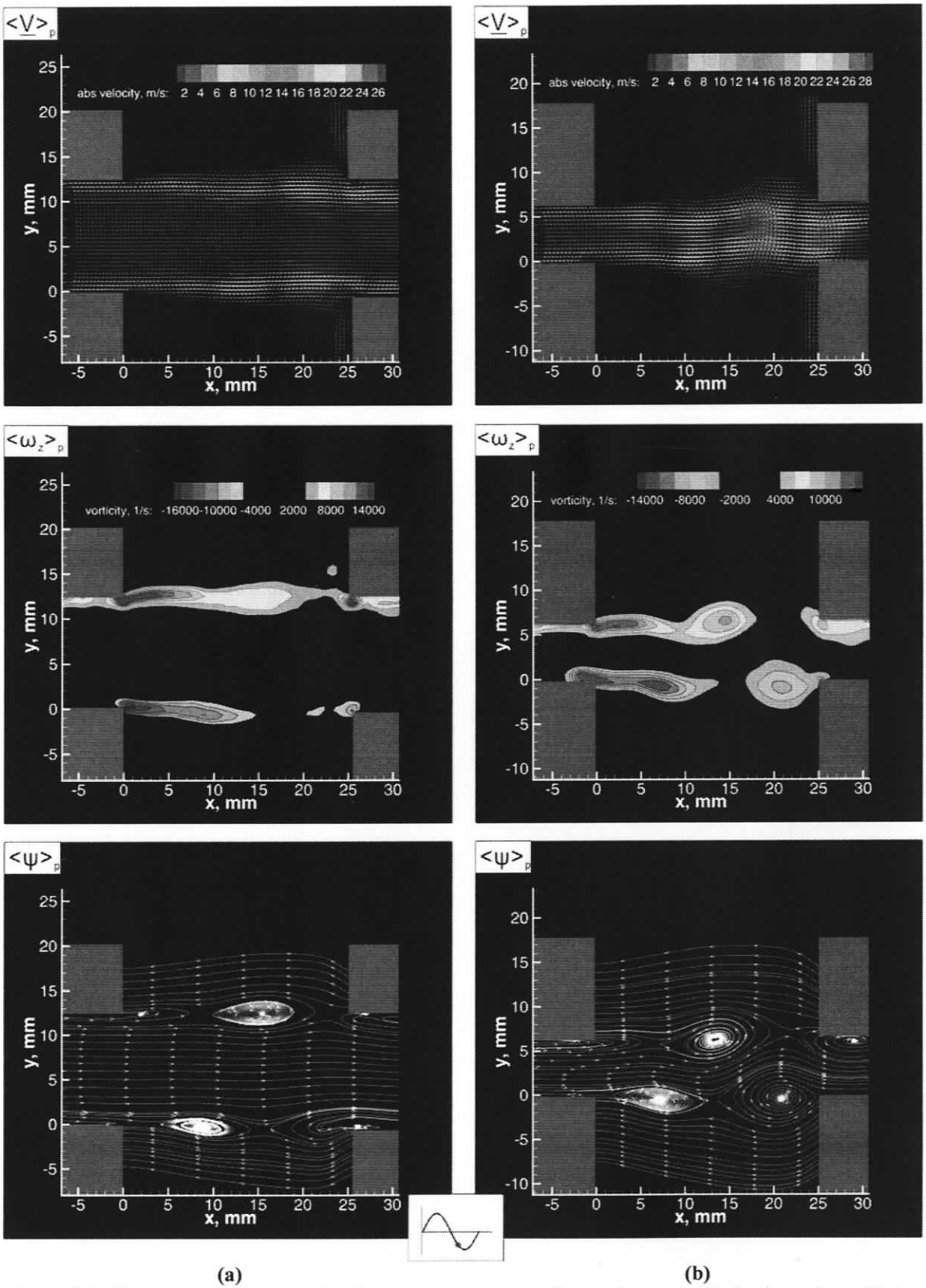

(a) **(b)**

Figure B.5: Phase-averaged streamwise flow patterns corresponding to the second hydrodynamic oscillation mode at φ=190°. (a) Flow patterns for the case of the wide main duct (D/L=0.5, Sr=0.82, U_{ac}/U=0.00017); (b) flow patterns for the case of the narrow main duct (D/L=0.25, Sr=0.76, U_{ac}/U=0.00036).

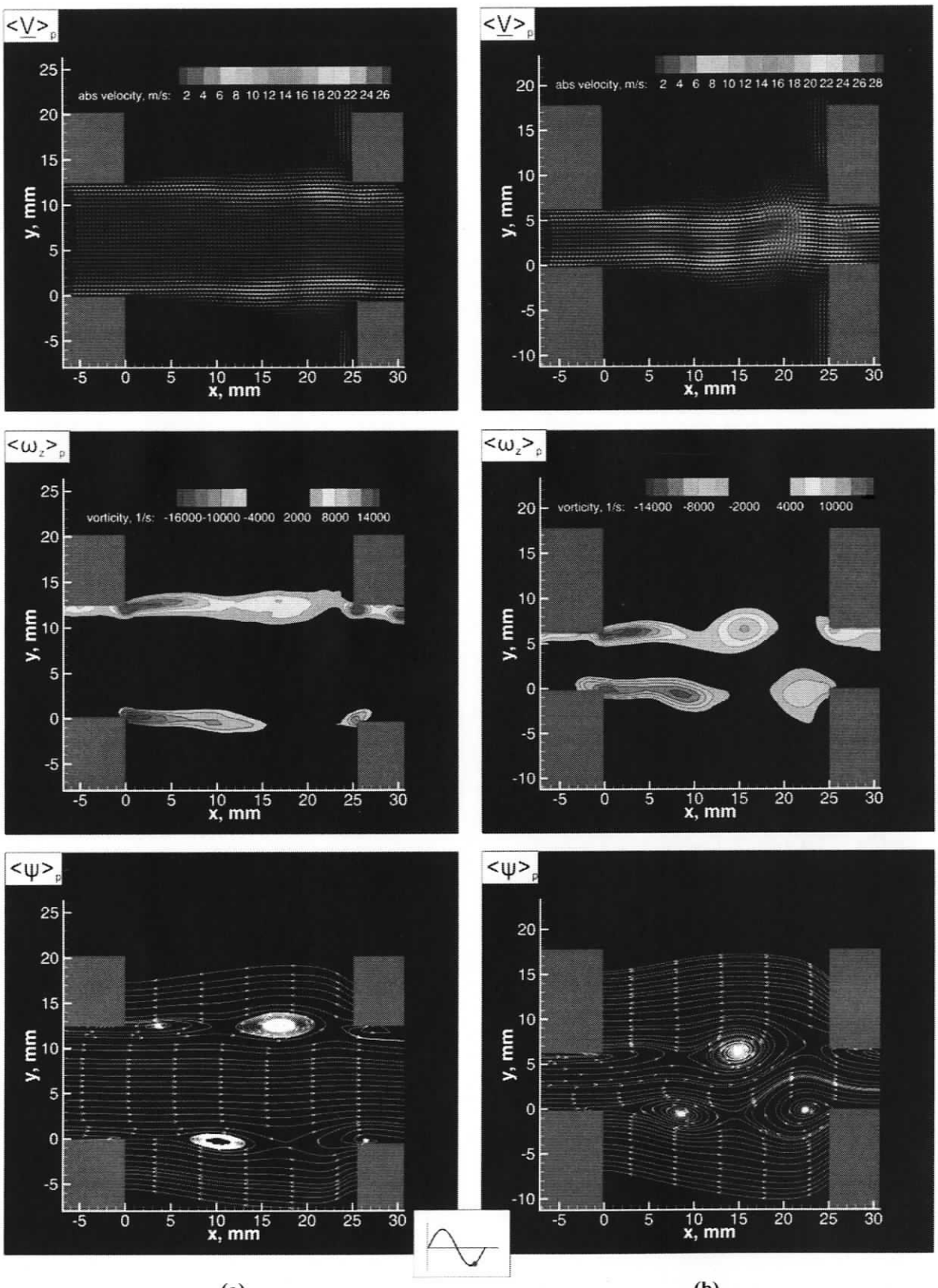

(a) (b)

Figure B.6: Phase-averaged streamwise flow patterns corresponding to the second hydrodynamic oscillation mode at φ=220°. (a) Flow patterns for the case of the wide main duct (D/L=0.5, Sr=0.82, U_{ac}/U=0.00017); (b) flow patterns for the case of the narrow main duct (D/L=0.25, Sr=0.76, U_{ac}/U=0.00036).

APPENDIX C: PHASE-AVERAGED ACOUSTIC POWER AT THE FIRST HYDRODYNAMIC OSCILLATION MODE

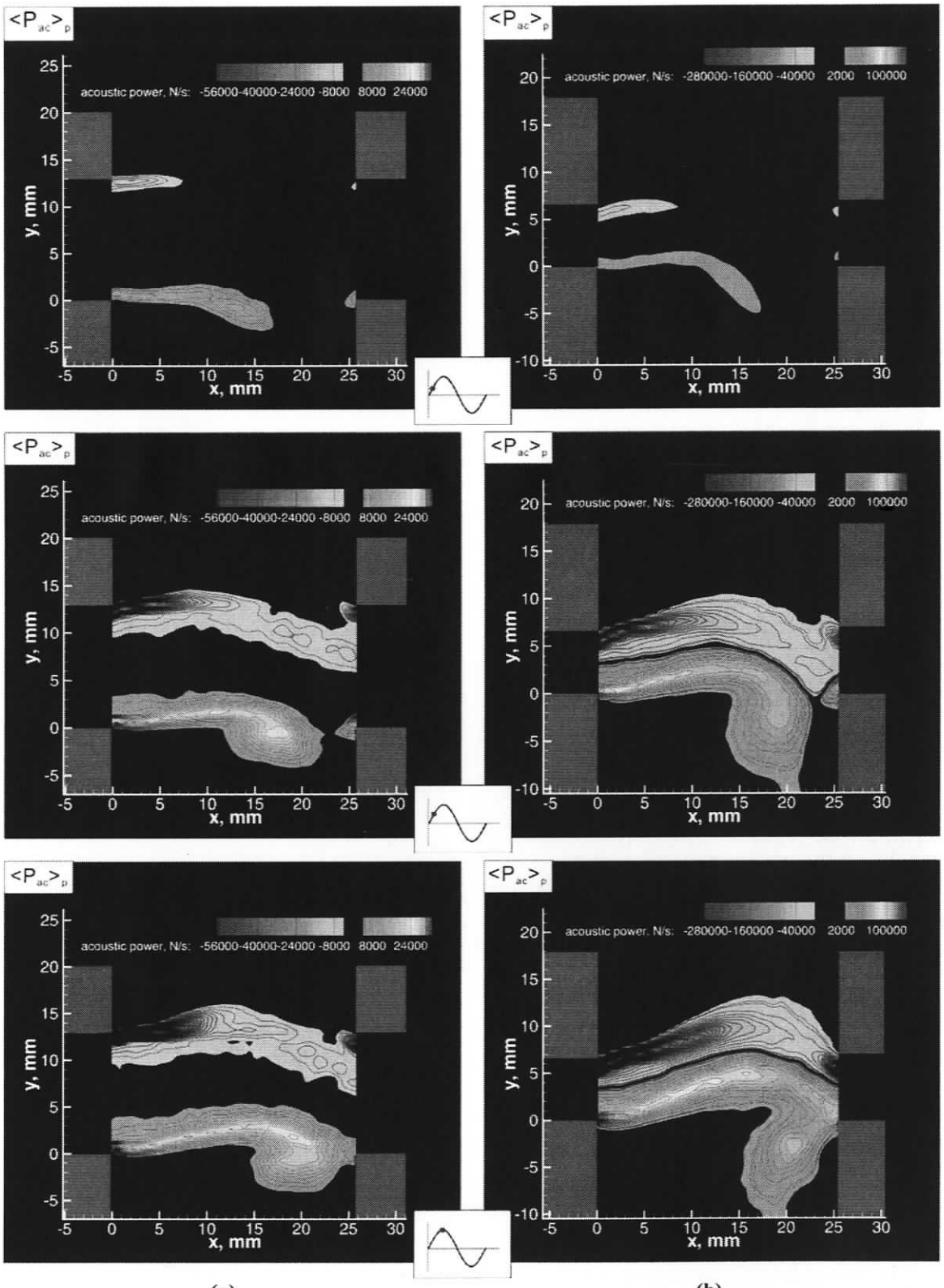

(a) **(b)**

Figure C.1: Patterns of phase-averaged acoustic power corresponding to the first hydrodynamic oscillation mode at three phases of acoustic cycle (φ=10°, 50°, and 90°). (a) Acoustic power for the case of the wide main duct (D/L=0.5, S=0.36, U_{ac}/U=0.0005); (b) acoustic power for the case of the narrow main duct (D/L=0.25, S=0.28, U_{ac}/U=0.001).

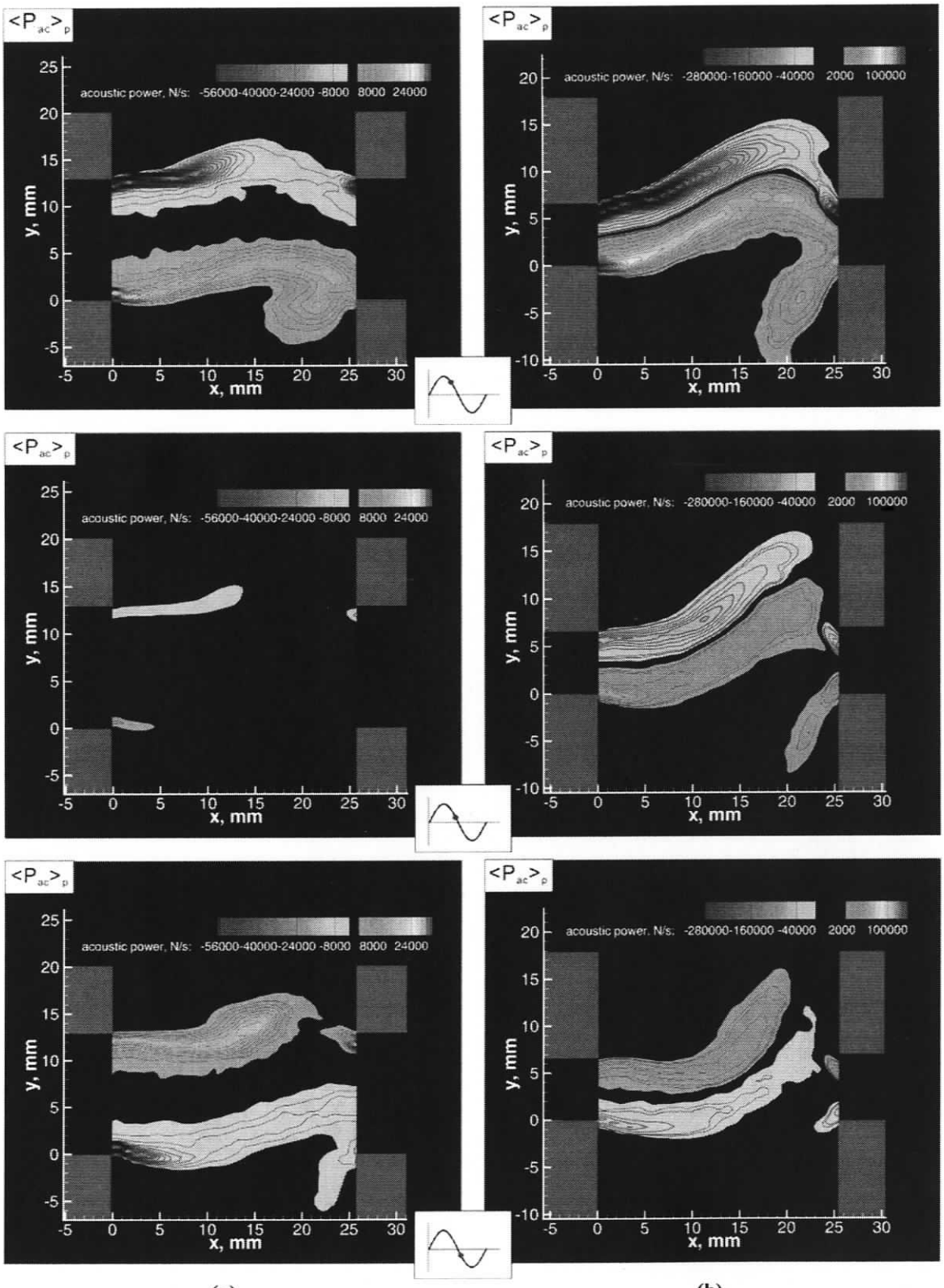

(a) **(b)**

Figure C.2: Patterns of phase-averaged acoustic power corresponding to the first hydrodynamic oscillation mode at three phases of acoustic cycle (φ=130°, 170°, and 210°). (a) Acoustic power for the case of the wide main duct (D/L=0.5, S=0.36, U_{ac}/U=0.0005); (b) acoustic power for the case of the narrow main duct (D/L=0.25, S=0.28, U_{ac}/U=0.001).

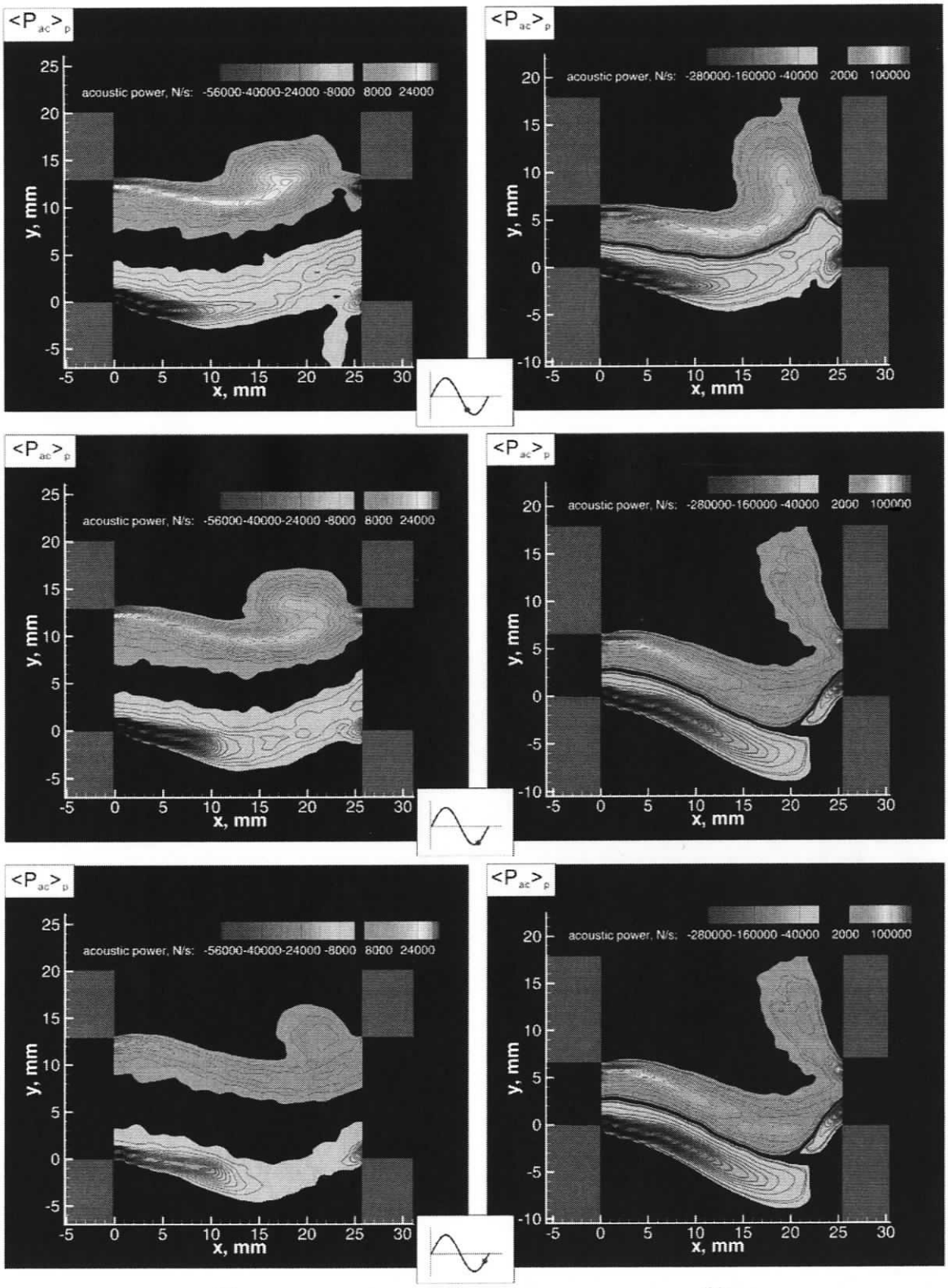

(a) (b)

Figure C.3: Patterns of phase-averaged acoustic power corresponding to the first hydrodynamic oscillation mode at three phases of acoustic cycle (φ=250°, 290°, and 330°). (a) Acoustic power for the case of the wide main duct (D/L=0.5, S=0.36, U_{ac}/U=0.0005); (b) acoustic power for the case of the narrow main duct (D/L=0.25, S=0.28, U_{ac}/U=0.001).

APPENDIX D: PHASE-AVERAGED ACOUSTIC POWER AT THE SECOND HYDRODYNAMIC OSCILLATION MODE

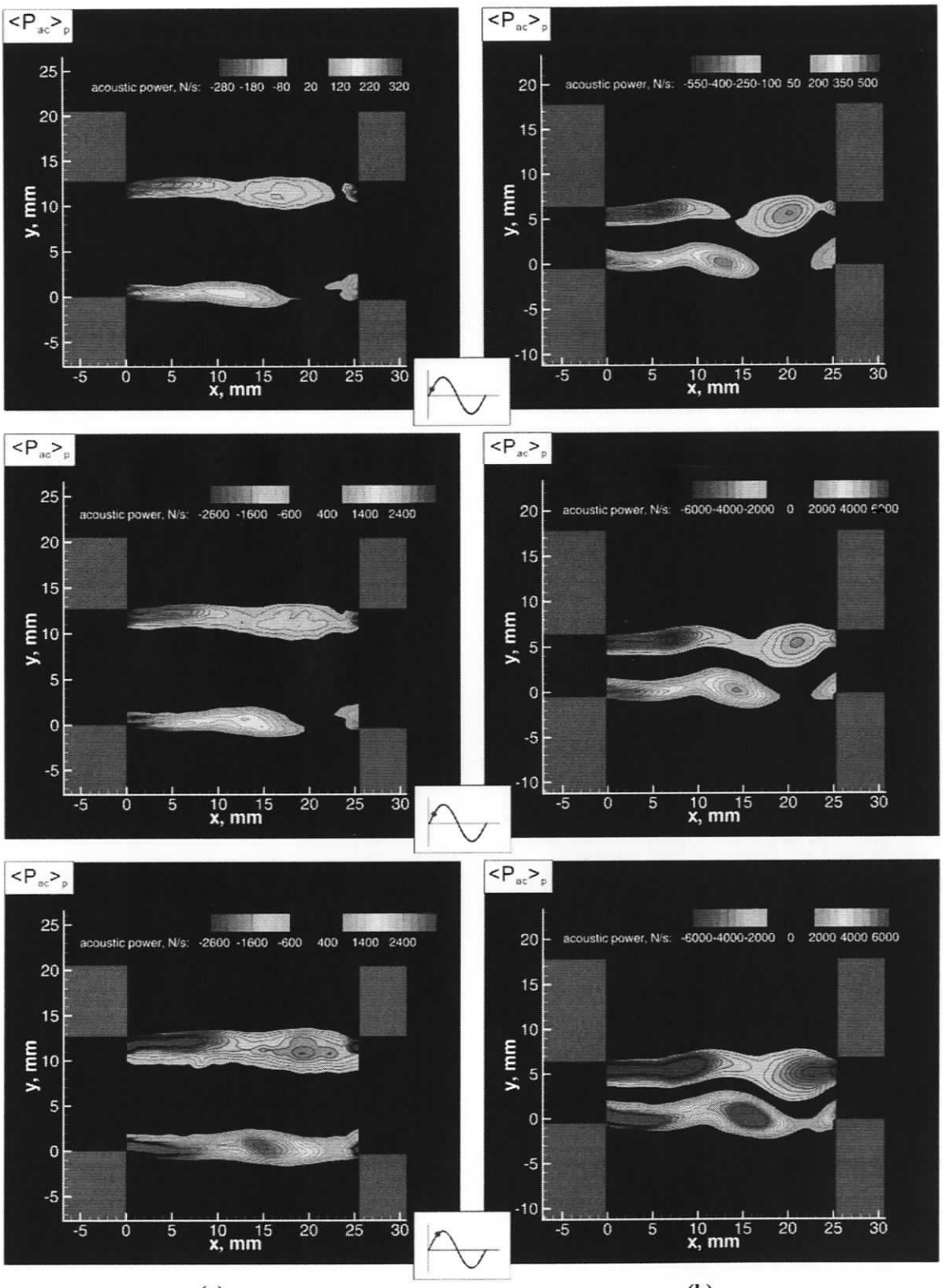

(a) **(b)**

Figure D.1: Patterns of phase-averaged acoustic power corresponding to the second hydrodynamic oscillation mode at three phases of acoustic cycle (φ=10°, 40°, and 70°). (a) Acoustic power for the case of the wide main duct (D/L=0.5, Sr=0.82, U_{ac}/U=0.00017); (b) acoustic power for the case of the narrow main duct (D/L=0.25, Sr=0.76, U_{ac}/U=0.00036).

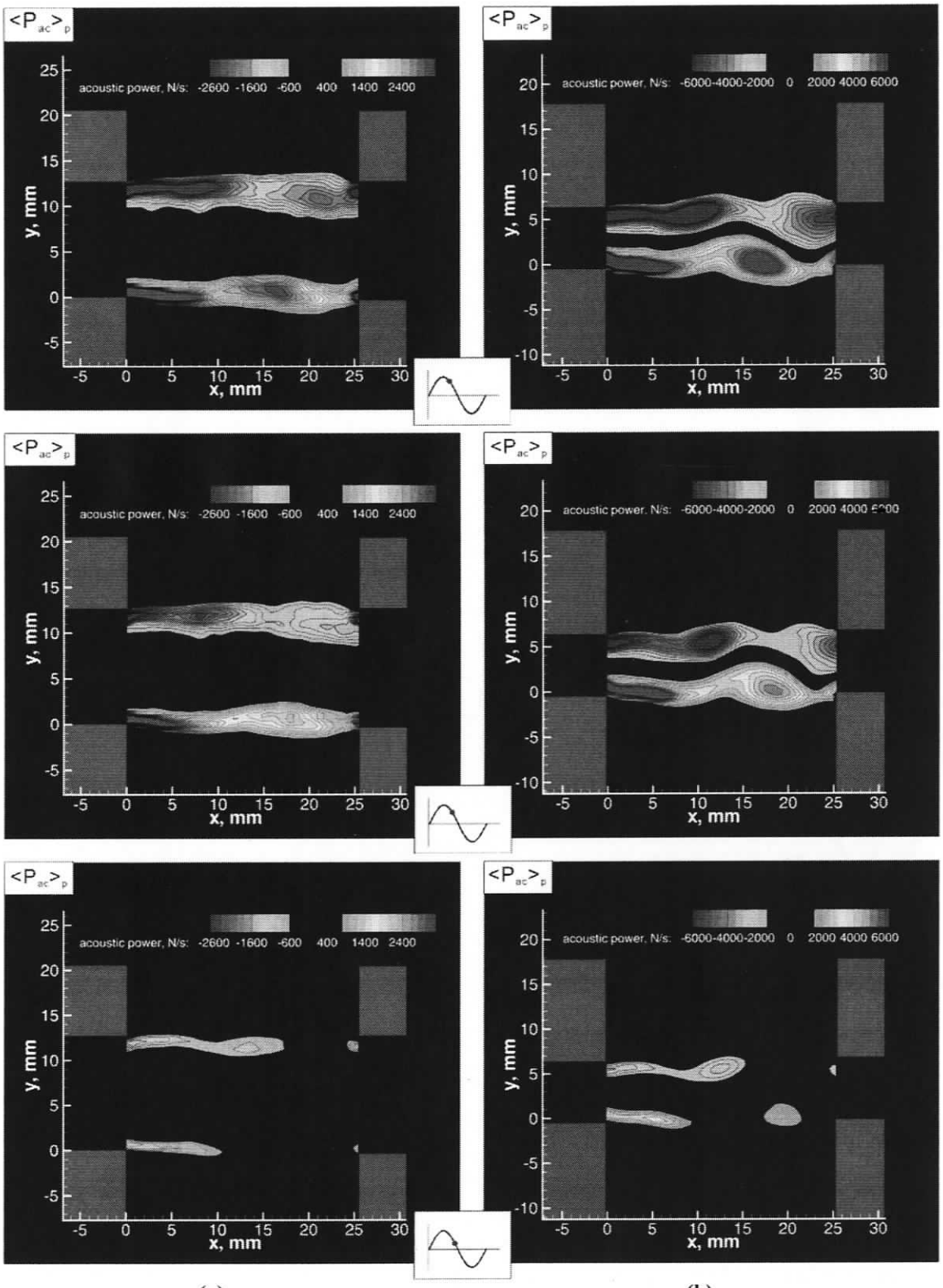

(a) **(b)**

Figure D.2: Patterns of phase-averaged acoustic power corresponding to the second hydrodynamic oscillation mode at three phases of acoustic cycle (φ=100°, 130°, and 160°). (a) Acoustic power for the case of the wide main duct (D/L=0.5, Sr=0.82, U_{ac}/U=0.00017); (b) acoustic power for the case of the narrow main duct (D/L=0.25, Sr=0.76, U_{ac}/U=0.00036).

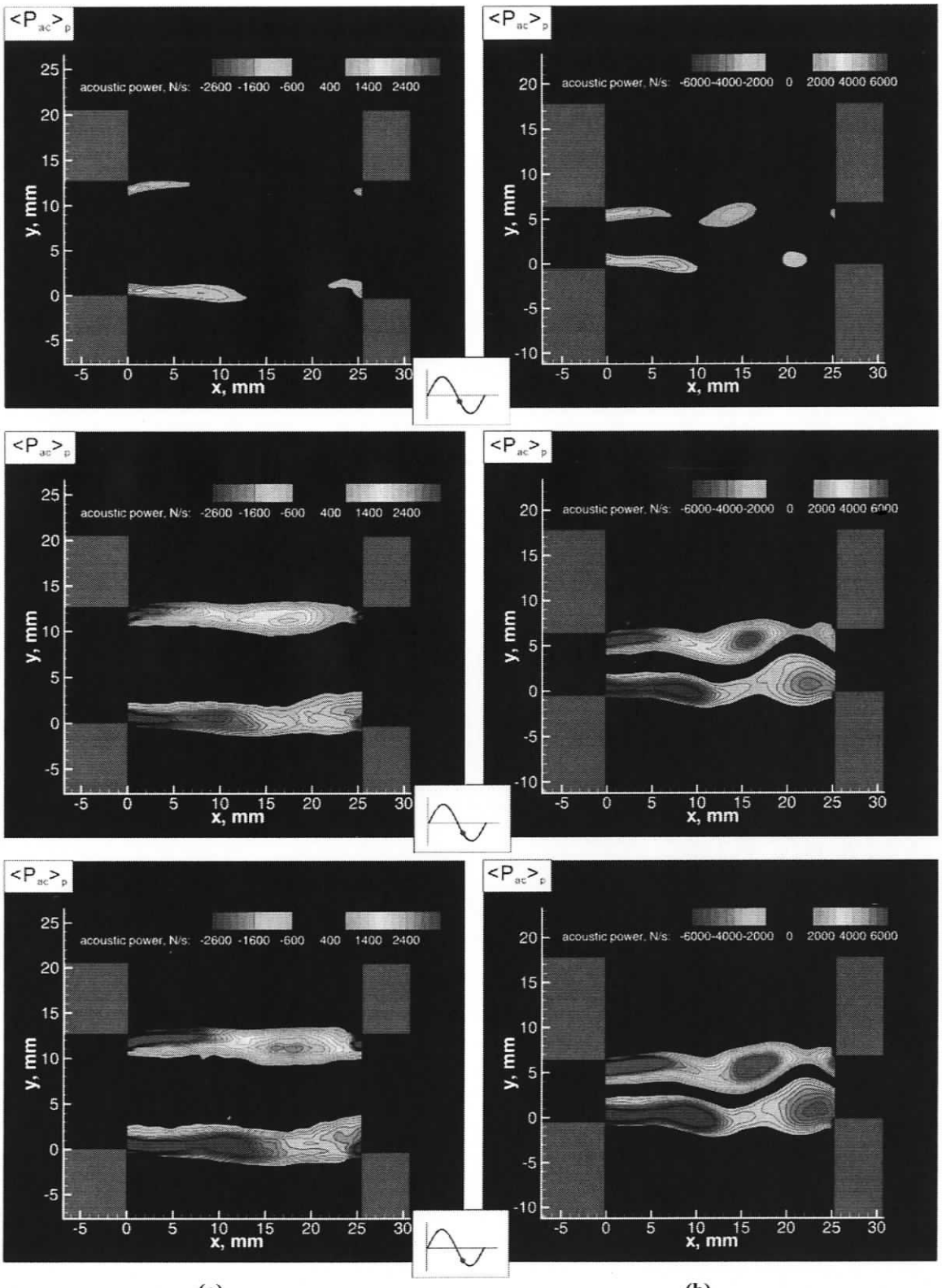

(a) **(b)**

Figure D.3: Patterns of phase-averaged acoustic power corresponding to the second hydrodynamic oscillation mode at three phases of acoustic cycle (φ=190°, 220°, and 250°). (a) Acoustic power for the case of the wide main duct (D/L=0.5, Sr=0.82, U_{ac}/U=0.00017); (b) acoustic power for the case of the narrow main duct (D/L=0.25, Sr=0.76, U_{ac}/U=0.00036).

APPENDIX E: MATLAB CODE

The Matlab code that was used to process the data from pressure transducers and to characterize the acoustic pressure in time and frequency domain is shown below.

```
%takes the spectrum outputted by Labview and creates Tecplot files to
%display the spectrum and the wave
%file format:  two columns, space delimited.  1st column is LHS Tx
%2nd column is RHS Tx

function [tx1, tx2, QS] = sing_spectrum()

%transducer sensitivity;
sens_tx1 = 1/1584;          %PSI/mV  tx1 is LHS
sens_tx2 = 1/1618;          %PSI/mV  tx2 is RHS #4049

%sampling rate that data was taken at.  Used to figure out period.
fs = 8192;

%dialog box for file input.  Make sure the file conforms to the format.
%Two columns.
[FileName,PathName] = uigetfile('*.*','Select the Spectrum File');

data_file = [PathName FileName];

%load the file as variable data
data = load ([data_file]);

%split each transducer data up
tx1 = data(:,1);            %1st column is tx1
tx2 = data(:,2);            %2nd column is tx2
%QS = data(:,3);              %3rth column is Q-switch

%adjust by the sensitivity
tx1 = (tx1.*sens_tx1*1000);       %sensitivity is for millivolts, data collected is volts
%tx2 = (tx2.*sens_tx2*1000);

%get the fft of each transducer
[f1, MX1] = fft_spectrum(tx1,fs);
%[f2, MX2] = fft_spectrum(tx2,fs);
%[f3, MX3] = fft_spectrum(QS,fs);
MX2 = MX1;
MX3 = MX1;

complete=[transpose(f1) MX1 MX2 MX3 ]; %combines the frequency and spectrum data.  Assumes f1==f2

scom = [PathName FileName '_Spectrum.txt']; %determines location to save combined data

%%%%%%%%%%%%%%%%%%%%%%%%%%%%%%%%%%%%%%%%%%%%%%%%%%%%%%%%%%%%%%%%%%%%%%%%
% TECPLOT file for the spectrum
%%%%%%%%%%%%%%%%%%%%%%%%%%%%%%%%%%%%%%%%%%%%%%%%%%%%%%%%%%%%%%%%%%%%%%%%
%Creating the 8 line header that is needed for Tecplot to read the file
```

```
str1='TITLE = "Average"';
str2='VARIABLES = "f, Hz"';
str3='"TX1, psi"';
str4='"TX2, psi"';
str8='ZONE T="ZONE 001"';
str9='I=8193, J=1, F=POINT';
str_f=strvcat(str1,str2,str3,str4,str8,str9);
fid=fopen(scom,'wt');
for i=1:6
  fprintf(fid,'%s',str_f(i,:));fprintf(fid,'\n');
end
sz=size(complete); %adding the combined data to the header
for i=1:sz(1)
  for j=1:3
    fprintf(fid,'%i\t',complete(i,j));
  end
  fprintf(fid,'\n');
end
fclose(fid)

%%%%%%%%%%%%%%%%%%%%%%%%%%%%%%%%%%%%%%%%%%%%%%%%%%%%%%%%%%%%%%%%%%%%%
% TECPLOT file for the wave
%%%%%%%%%%%%%%%%%%%%%%%%%%%%%%%%%%%%%%%%%%%%%%%%%%%%%%%%%%%%%%%%%%%%%

period = 1/fs;        %period = 1/fs
wave = size(tx1);     %assumes size of tx1 = size tx2

%only take one second worth of info
time = linspace(0,(period*wave(1)),wave(1));

complete=[transpose(time) tx1 QS ]; %combines the vorticity and velocity data

  scom = [PathName FileName '_Wave.txt']; %determines location to save combined data

  % Creating the 8 line header that is needed for Tecplot to read the file
  str1='TITLE = "Wave"';
  str2='VARIABLES = "Time, (s)"';
  str3='"TX1, psi"';
  str4='"QS, V"';
  str8='ZONE T="ZONE 001"';
  str9='I=654300, J=1, F=POINT';
  str_f=strvcat(str1,str2,str3,str4,str8,str9);
  fid=fopen(scom,'wt');

  for i=1:6
    fprintf(fid,'%s',str_f(i,:));fprintf(fid,'\n');
  end
  sz=size(complete); %adding the combined data to the header
  for i=1:sz(1)
    for j=1:3
      fprintf(fid,'%i\t',complete(i,j));
    end
    fprintf(fid,'\n');
  end
  fclose(fid)
```

```
return

end

%%%%%%%%%%%%%%%%%%%%%%%%%%%%%%%%%%%%%%%%%%%%%%%%%%%%%%%%%%%%%%%%%%%%%%%%%%%%%%%%
%FFT Calculation
%%%%%%%%%%%%%%%%%%%%%%%%%%%%%%%%%%%%%%%%%%%%%%%%%%%%%%%%%%%%%%%%%%%%%%%%%%%%%%%%
%this function runs the fft through the transducer data.  This code is modified from the mathworks (matlab)
website
function [f,MX] = fft_spectrum(tx,fs)

   %some arbitrary power of 2
   NFFT =16384;

   % Take fft, padding with zeros, length(FFTX)==NFFT
   FFTX=fft(tx,NFFT);

   NumUniquePts = ceil((NFFT+1)/2);

   % fft is symmetric, throw away second half
   FFTX=FFTX(1:NumUniquePts);

   MX=abs(FFTX);          % Take magnitude of X
   % Scale the FFT so that it is not a function of the length of x.
   MX=MX/length(tx);

   % Multiply by 2 to take into account the fact that we threw out second half of FFTX above
   MX=MX*2;
   MX(1)=MX(1)/2;   % Account for endpoint uniqueness
   % Nyquist component should also be unique.
   MX(length(MX))=MX(length(MX))/2;

   MX(1)=0;

   f=(0:NumUniquePts-1)*fs/NFFT;

return
end
```

The Matlab code that was used to create the combination file of velocity and vorticity, which is readable in Tecplot, is shown below.

```
function vortvelv(n)
    n=3;
  for k=3:n %loop to determine the file names of the images
     clear svel
     clear svor
     if k<=9 %the different cases are to account for DaVis saving notation
        identve = sprintf('velocity0000%g_0', k); %identve stores the velocity filename
        identvo = sprintf('vorticity0000%g_0', k); %identvo stores the vorticity filename
        nk = sprintf('00%g',k); %nk is a new k to format the file names properly
     elseif k<=99
        identve = sprintf('velocity000%g_0', k);
        identvo = sprintf('vorticity000%g_0', k);
        nk = sprintf('0%g',k);
     else
        identve = sprintf('velocity00%g_0', k);
        identvo = sprintf('vorticity00%g_0', k);
        nk = sprintf('%g',k);
     end
     svel=sprintf('F:\\TingDATA\\FSCPhaselocked\\Scan_Cam1=PIV_Delay=0.400_0\\text\\%s.txt',identve);
%adds the location information to filename
     svor=sprintf('F:\\TingDATA\\FSCPhaselocked\\Scan_Cam1=PIV_Delay=0.400_0\\text\\%s.txt',identvo);
%adds the location information to filename
     velocity=textread(svel,'',-1,'headerlines',1); %loads the data file under velocity
     vorticity=textread(svor,'',-1,'headerlines',1); %loads the data file under vorticity
     eval(['clear ', identve,' ',identvo]);
     i=1; %counter for y coordinate
     j=1; %counter for x coordinate
     u=0; %variable for the u component of the velocity for calculating the absolute velocity
     v=0; %variable for the w component of the velocity for calculating the absolute velocity
     ylim=130; %number of measurements along the y axis
     xlim=172; %number of measurements along the x axis
     plim= xlim * ylim %number of measurements points
     vorticity2=zeros(plim,1); %vector for the newly arranged vorticity data
     velmag=zeros(plim,1); %vector for the newly created velocity magnitude data
     for i = 1:ylim %rearranges the vorticity data
        for j = 1:xlim
           m = (i-1)*xlim + j;
           vorticity2(m) = vorticity(i,j);
        end
        j = 1;
     end
     for i = 1:plim
        velocity(i,1)=velocity(i,1);
        velocity(i,2)=velocity(i,2);
        u=velocity(i,3);
        v=velocity(i,4);
        velmag(i)=sqrt(u^2+v^2);
     end
     complete=[velocity velmag vorticity2]; %combines the vorticity and velocity data
```

```
scom=sprintf('F:\\TingDATA\\FSCPhaselocked\\Scan_Cam1=PIV_Delay=0.400_0\\text\\velvort%s.txt',nk);
%determines location to save combined data
    % Creating the 8 line header that is needed for Tecplot to read the file
    str1=sprintf('TITLE = "velvort%s"',nk);
    str2='VARIABLES = "x, mm"';
    str3='"y, mm"';
    str4='"u, m/s"';
    str5='"v, m/s"';
    str6='"abs velocity, m/s"';
    str7='"vorticity, 1/s"';
    str8='ZONE T="ZONE 001"';
    str9='I=172, J=130, F=POINT';
    str_f=strvcat(str1,str2,str3,str4,str5,str6,str7,str8,str9);
    fid=fopen(scom,'wt');
    for i=1:9
      fprintf(fid,'%s',str_f(i,:));fprintf(fid,'\n');
    end
    sz=size(complete); %adding the combined data to the header
    for i=1:sz(1)
      for j=1:6
        fprintf(fid,'%i\t',complete(i,j));
      end
      fprintf(fid,'\n');
    end
    fclose(fid)
  end
clear
return
```

APPENDIX F: LABVIEW CODE

The Labview code that was used for acquisition of acoustic pressure, which was measured by the pressure transducers at the end of the side braches, is shown below.

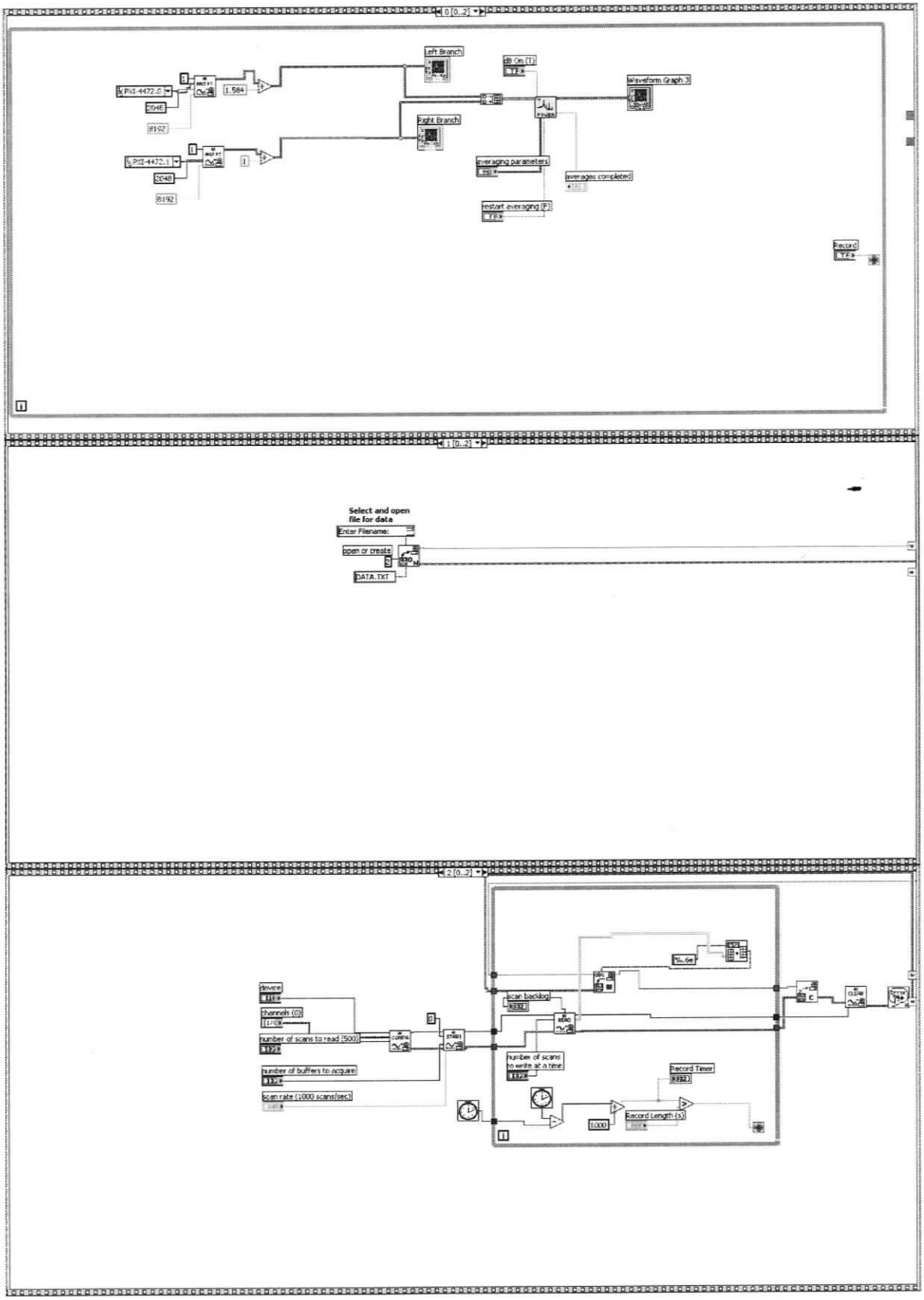
0 [0..2]
Left Branch
dB On (T)
Waveform Graph 3
PXI-4472.0
1.584
2048
8192
Right Branch
PXI-4472.1
2048
8192
averaging parameters
averages completed
restart averaging (F)
Record
1 [0..2]
Select and open file for data
Enter Filename:
open or create
DATA.TXT
2 [0..2]
%.6e
device
channels (0)
number of scans to read (500)
number of buffers to acquire
scan rate (1000 scans/sec)
config
start
scan backlog
read
number of scans to write at a time
Record Timer
1000
Record Length (s)
write
close

The Labview code that was used to realize the phase-locking is shown below.